FAA-RD-76-55

Project Report
ATC-68

Multipath Parameter Computations for the MLS Simulation Computer Program

J. Capon

8 April 1976

Lincoln Laboratory
MASSACHUSETTS INSTITUTE OF TECHNOLOGY
LEXINGTON, MASSACHUSETTS

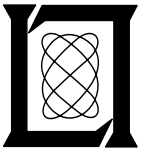

Prepared for the Federal Aviation Administration,
Washington, D.C. 20591

This document is available to the public through
the National Technical Information Service,
Springfield, VA 22161

1. Report No.	2. Government Accession No.	3. Recipient's Catalog No.
FAA-RD-76-55		

4. Title and Subtitle	5. Report Date
Multipath Parameter Computations for the MLS Simulation Computer Program	8 April 1976
	6. Performing Organization Code

7. Author(s)	8. Performing Organization Report No.
Jack Capon	ATC-68

9. Performing Organization Name and Address	10. Work Unit No. (TRAIS)
Massachusetts Institute of Technology Lincoln Laboratory P.O. Box 73 Lexington, MA 02173	11. Contract or Grant No. DOT-FA74WAI-461
	13. Type of Report and Period Covered Project Report
12. Sponsoring Agency Name and Address Department of Transportation Federal Aviation Administration Systems Research and Development Service Washington, DC 20591	14. Sponsoring Agency Code

15. Supplementary Notes

The work reported in this document was performed at the Massachusetts Institute of Technology Lincoln Laboratory under Air Force Contract F19628-76-C-0002.

16. Abstract

A set of mathematical models and computer programs have been developed to characterize multipath propagation in an airport environment. When combined with system mathematical models, these models are intended to provide a firm technical basis for assessing the performance of candidate Microwave Landing Systems (MLS) in realistic airport environments. The two paramount issues in developing these models have been 1) validation based on actual field test data and 2) computer running time.

The obstacles modeled include buildings and aircraft, as well as the ground which can cause both specular reflections and diffuse scattering. In addition, the shadowing effects due to runway humps, and aircraft, buildings approaching the line of sight between transmitter and receiver are included. Computational procedures are presented for obtaining the salient multipath parameters, i.e., relative magnitude, phase, directional angles, Doppler frequency, and time delay.

Computer programs have been written for these algorithms using the Fortran programming language, with structured programming methods, such as Iftran, employed whenever possible. A presentation is given of computer validation data for the computational procedures. A comparison of these computer validation results with experimental field data demonstrates good agreement in all cases of interest. The computer running time for these computer programs is quite reasonable, e.g., it takes about five times longer than actual flight time to run a model of a typical airport environment on an IBM 370 model 168.

17. Key Words	18. Distribution Statement
Microwave Landing System L-band multipath C-band multipath	Document is available to the public through the National Technical Information Service, Springfield, Virginia 22151.

19. Security Classif. (of this report)	20. Security Classif. (of this page)	21. No. of Pages	
Unclassified	Unclassified	196	

TABLE OF CONTENTS

LIST OF ILLUSTRATIONS

List of Illustrations (Cont'd)

List of Illustrations (Cont'd)

List of Illustrations (Cont'd)

List of Illustrations (Cont'd)

I. INTRODUCTION

The Microwave Landing System (MLS) is being developed to provide all-weather landing guidance information for a wide range of aircraft approach angles. The increased accuracy and greatly expanded coverage requirements of MLS, relative to existing Instrument Landing Systems (ILS), tend to make the influence of multipath propagation a major factor in the determination of MLS system performance. It is for this reason that a computer program has been written to perform multipath modeling and simulation for MLS. The purpose of this report is to present a discussion of the computer programs which have been used in this MLS simulation for determining the multipath components which occur due to obstacles which are found in typical airport environments. In most cases of interest these computer models are compared with experimental field data in order to show that they are good replicas of real world situations.

The multipath propagation due to reflections and scattering from large buildings in proximity to runways, and from large aircraft in landing patterns or on adjacent taxiways, pose some of the more critical discriminants for MLS. In addition, there are severe requirements posed for MLS by shadowing effects due to runway humps, and aircraft and buildings approaching the line of sight between the ground transmitter and the aircraft receiver. Since airport topographies can vary widely, it is not feasible to attempt to standardize the description of such obstacle multipath propagation for any given airport.

In this paper a description is given of the methods which have been used to model the obstacles in an airport environment. Descriptions are also presented for the computer programs which have been implemented for the purpose of determining the obstacle multipath components. The models to be presented have been employed to compute the effects due to specular reflection, as well as diffuse scattering, from the ground located near the transmitter antenna. In addition, a description is given of the algorithms used to determine the effect due to scattering from buildings, or hangars, and aircraft. The methods for treating the shadowing effect due to runway humps, and aircraft or buildings which are near the line of sight between transmitter and receiver, are also discussed.

The following important points concerning these models should be stressed. One point is that the complex real world objects are represented by certain simpler objects which more readily lend themselves to practical computation routines. As an example, aircraft fuselages are modeled as metallic cylinders. Another point is that a feasible computational algorithm must be used to give a quantitative expression for the scattered signal. In this case there must be a compromise between accuracy and computational speed. In order to achieve these goals, we typically have used a mixture of physical optics and geometric optics algorithms as opposed to rigorous solutions of the particular electromagnetic wave propagation boundary value problem.

A presentation is also given of the computer validation data in order to provide some perspective on the magnitude of the various scattered signals. These data are also compared with experimental field data in order to

establish that the computer algorithms are realistic models of real world configurations. The principal sources of test results were the U.S. MLS Phase I and II experimental data, the Lincoln Laboratory Logan MLS multipath experiment, the R.A.E. (U.K.) MLS system study, the Thomson-CSF MLS TACD program, and the Lincoln Laboratory discrete address beacon system experimental facility (DABSEF). The frequency ranges at which these data were obtained included L-band, 1 GHz, C-band, 5 GHz, and K_u-band, 15 GHz. In addition, the computer running time, as well as flow chart descriptions, are given for the various subprograms employed in the multipath computations. These subprograms have been designed to be system-independent. This implies that the multipath computations pertain to the particular geometry, or configuration, used to model the airport environment. Another implication is that these results can be used to evaluate the performance of many different types of MLS systems, for the particular airport environment.

II. SPECULAR GROUND REFLECTION

A. Description of Theory

In this section we present the computations required to obtain the multipath component due to the specular reflection from the ground directly in front of the transmitting antenna. Towards this end it is assumed that the ground, considered as a scattering surface, has a small-scale roughness superimposed on a large-scale roughness which can be described by topographical features. This model for the ground is termed a composite rough surface, and has been discussed by Beckmann.[1] The large-scale roughness can be modeled by dividing the ground into a number of plane surface elements. These surface elements are taken to be triangles or rectangles. The position and orientation of a surface element is specified by the three, or possibly four, rectangular coordinates of the corners of the element. The electrical properties of the ground are assumed to be homogeneous over each surface element, and specified by its relative complex dielectric constant

$$\varepsilon_r = \varepsilon_R - j\varepsilon_I \quad , \tag{II-1}$$

where ε_R, ε_I are the real and imaginary relative dielectric constants, respectively, given by

$$\varepsilon_R = \varepsilon/\varepsilon_o \quad , \tag{II-2}$$

$$\varepsilon_I = \sigma_c/\omega\varepsilon_o \quad , \tag{II-3}$$

ε_0 is the dielectric constant of free space, ε is the dielectric constant of the surface element, σ_c is the conductivity of the surface element, and ω is the radian frequency of the incident wave, cf. Kerr,[2], p. 397. It should be noted that snow banks at the edge of the runways can be modeled by means of the large-scale roughness model for the ground.

The small-scale roughness is assumed to have features with a Gaussian height distribution, with root-mean-square roughness height σ_h, as indicated by Beckmann and Spizzichino.[3] In addition, the following assumptions are required for the small-scale roughness.

(1) Radius of curvature of scattering surface is much greater than wavelength of incident radiation,

(2) Shadowing effects caused by small-scale roughness may be neglected,

(3) Multiple scattering between adjacent parts of same surface may be neglected.

The electromagnetic field scattered from a rough surface may be considered as a sum of a specular and diffuse component. Specular reflection is highly directional, i.e., propagation occurs over a small angle in space, and its phase is coherent, i.e., directly related to the phase of the incident wave. In addition, specular reflection results from radiation from an area within the first few Fresnel ellipses, or zones, cf. Kerr,[2] pp. 411-418. Diffuse scattering has less directivity, and takes place due to radiation from a much larger surface area than the first few Fresnel zones, which is known as the glistening surface, cf. Beckmann and Spizzichino,[3] p. 256. The phase

angles of the diffusely scattered waves are incoherent, i.e., these phase angles cannot be directly related to the phase of the incident wave at all points in space. In addition, its amplitude is a non-deterministic, or random, quantity in the sense that it is different for each rough surface which is a sample function from the ensemble of such sample functions. The probability distribution of the diffusely scattered field amplitude is a Rayleigh distribution, while that of the phase is a uniform distribution, cf. Beckmann and Spizzichino,[3] Chapter 7.

In general, both specular and diffuse components are present simultaneously. If the root-mean-square roughness height, σ_h, is small compared to the wavelength, λ, then the specular component predominates. Otherwise, the specular component is negligible and the diffuse component predominates.

We now present the computations required to determine the amplitude, phase, planar directional angles, fractional Doppler frequency, and time delay for the specular ground reflection. The corresponding computations for the diffuse component are presented subsequently in Section V. The geometry of specular reflection is given in Fig. II-1, assuming, for simplicity, that the orientations of the surface elements are all parallel to some ground plane.

The field amplitude $E(r)$ at distance r from the transmitting antenna is assumed to be a uniform plane wave

$$E(r) = \frac{A}{r} \varepsilon^{-jkr} \quad , \qquad \text{(II-4)}$$

where k is the wavenumber, so that $k=2\pi/\lambda = \omega/c$, λ is the wavelength, A is a constant and c is the velocity of propagation. The field at the receiver due to direct transmission is

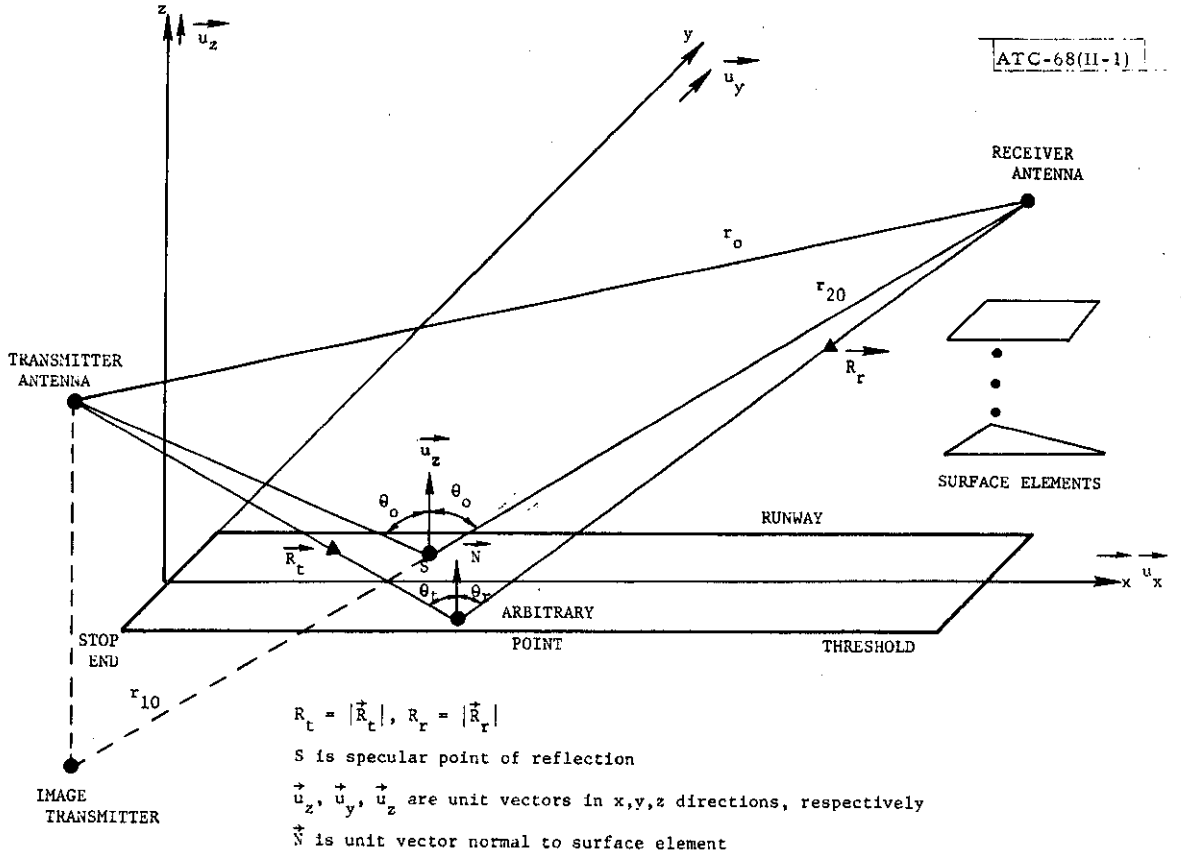

Fig. II-1. Geometry for specular reflection from the ground.

$$E_o = \frac{A}{r_o} \varepsilon^{-jkr_o} \quad . \qquad \text{(II-5)}$$

The field amplitude at the receiver can be found by using the Fresnel-Kirchoff diffraction formula, cf. Goodman,[4] p. 41, or Sommerfeld,[5] p. 201,

$$E_s = \frac{Aj}{\lambda} \iint_{\substack{\text{all} \\ \text{surface} \\ \text{elements}}} \frac{1}{R_r R_t} \frac{[\cos \theta_r + \cos \theta_t]}{2} \varepsilon^{-jk(R_r + R_t)} \, dS \, . \qquad \text{(II-6)}$$

It should be mentioned that the results in Ref. 5 must be used with a slight modification. That is, it is assumed in Ref. 5 that the transmitter signal has a frequency variation of $\varepsilon^{-i\omega t}$, instead of $\varepsilon^{i\omega t}$. As a consequence, in order to obtain the correct phase relationship, it is necessary to use the complex conjugate of all expressions derived in Ref. 5. We now wish to indicate the modifications required in Eq. (II-6) to take account of transmitter and receiver antenna patterns, and finite ground conductivity, as well as several practical computational simplifications. The major contribution to the integral in Eq. (II-6) occurs near the point of specular reflection. In order to take the small-scale roughness of the surface into account, an attenuation factor ρ_r, can be introduced in the diffraction formula, cf. Beckmann and Spizzichino,[3] p. 81,

$$\rho_r = \varepsilon^{-\frac{1}{2}\left(\frac{4\pi}{\lambda} \sigma_h \cos\theta_t\right)^2} \quad . \qquad \text{(II-7)}$$

The factor of 1/2 in the exponent in Eq. (II-7) is required since an amplitude, and not power, attenuation factor is needed.

The phase shift and attenuation caused by the reflection are given by the Fresnel reflection coefficients, cf. Kerr,[2] p. 396. These coefficients depend on the polarization of the wave relative to the surface, the angle of incidence, and the relative complex dielectric constant of the reflecting medium. For vertical polarization, i.e., the electric (E) field is in the plane of incidence defined by the incident vector $\vec{R}_t$ and surface normal vector $\vec{N}$, the Fresnel reflection coefficient is given by

$$R_v(\theta_t) = \frac{\varepsilon_r \cos\theta_t - \sqrt{\varepsilon_r - \sin^2\theta_t}}{\varepsilon_r \cos\theta_t + \sqrt{\varepsilon_r - \sin^2\theta_t}} \quad , \qquad \text{(II-8)}$$

where ε_r is the relative complex dielectric constant given in Eq. (II-1). If the E field is perpendicular to the plane of incidence, then we have horizontal polarization and the Fresnel reflection coefficient is

$$R_h(\theta_t) = \frac{\cos\theta_t - \sqrt{\varepsilon_r - \sin^2\theta_t}}{\cos\theta_t + \sqrt{\varepsilon_r - \sin^2\theta_t}} \quad . \qquad \text{(II-9)}$$

If the surface element is inclined, so that it is not horizontal, or vertical, then it is necessary to use an equivalent reflection coefficient, as indicated by Mitzner.[6] If the wave is initially vertically polarized, relative to the horizontal ground plane, then the equivalent reflection coefficient for the corresponding vertically polarized component of the wave reflected by the inclined surface element is given by[6]

$$R_{eq} = R_v(\theta_t) \cos \alpha_1 \cos \alpha_2 + R_h(\theta_t) \sin \alpha_1 \sin \alpha_2 \ , \qquad \text{(II-10)}$$

(vertical polarization)

where α_1 is the angle between the vertical plane defined by R_t and the z-axis, and the local plane of incidence defined by $\vec{R}_t$ and the normal to the surface element, and α_2 is the angle between the vertical plane defined by $\vec{R}_r$ and the z-axis, and the local plane of incidence. For horizontal polarization we have[6]

$$R_{eq} = R_v(\theta_t) \sin \alpha_1 \sin \alpha_2 + R_h(\theta_t) \cos \alpha_1 \cos \alpha_2 \ . \qquad \text{(II-11)}$$

(horizontal polarization)

The details of the computation for R_{eq}, for arbitrarily tilted surfaces, are presented in Appendix A. It should be noted that for a perfect conductor, i.e., ϵ_R is finite, $\epsilon_I = \infty$, we have

$$R_v(\theta_t) = 1, \quad \theta_t \neq \pi/2, \quad \text{(perfect conductor)} \qquad \text{(II-12)}$$

$$R_h(\theta_t) = -1, \quad \text{(perfect conductor)}. \qquad \text{(II-13)}$$

The surface of integration in the Fresnel-Kirchoff diffraction formula given in Eq. (II-6) must, as a practical matter, be limited. The manner in which this is to be done is to integrate in a certain manner only over a certain number of Fresnel zones. The Fresnel zone is an elliptical region within which the total path length, $R_t + R_r$, is less than one half-wavelength longer than the minimum path length $r_{10} + r_{20}$. The Fresnel zones are shown in Fig. II-2, where, for simplicity, the transmitter and receiver are shown on the x-axis, and where the dimensions of the Fresnel zones are, cf. Kerr,[2] pp. 411-418,

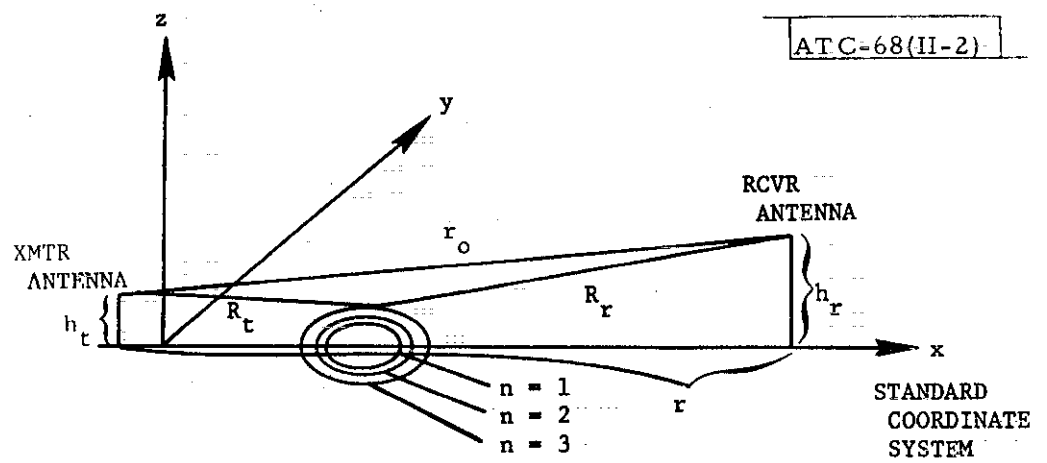

(a)

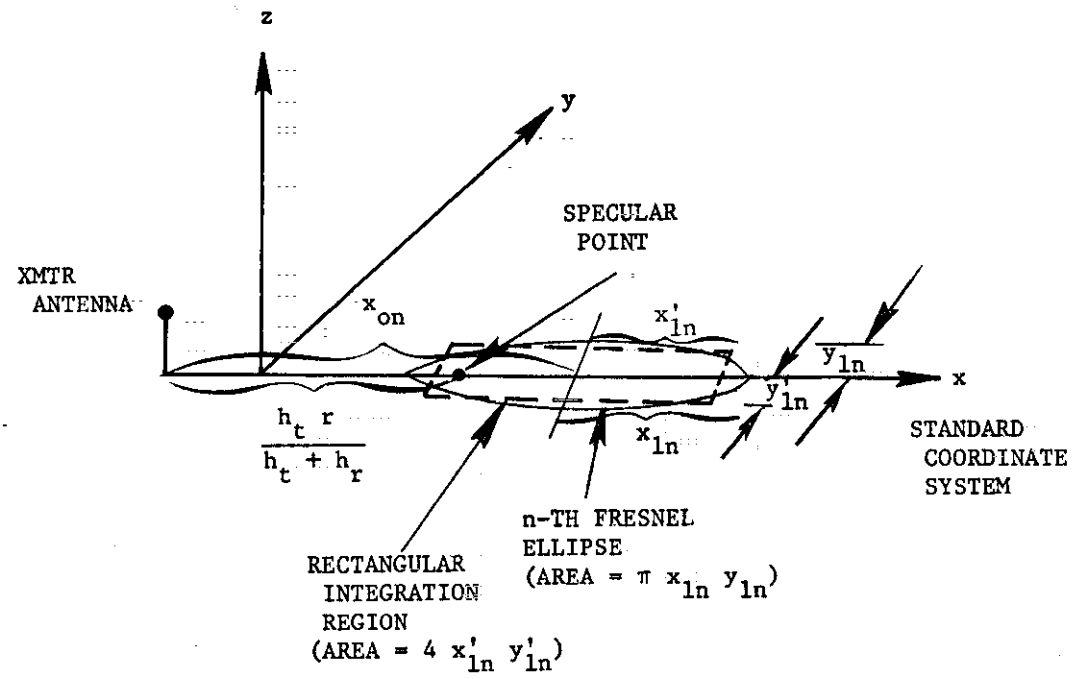

(b)

Fig. II-2. Description of the Fresnel zones.

and rectangular integration region. In Section IIC it is shown that it is better to use the rectangular integration region, since this leads to improved accuracy in the computational results. Thus, the final version of the program uses a rectangular integration region. When an elliptical integration region is used, with the integration occurring over n Fresnel zones, then the center, major, and minor axes of the Fresnel ellipse are chosen as in Eqs. (II-14) through (II-16). If a rectangular integration region is to be employed, then the half-lengths of the sides of the rectangular integration region, depicted in Fig. II-2, are given by $x'_{1n} = \frac{\sqrt{\pi}}{2} x_{1n}$, $y'_{1n} = \frac{\sqrt{\pi}}{2} y_{1n}$, where x_{1n}, y_{1n} are the lengths of the major and minor axes, respectively, of the n-th Fresnel ellipse given in Eqs. (II-15), (II-16). The center of the rectangular region is located at the same point as the center of the elliptical region, given by x_{on} in Eq. (II-14). It is easily seen that the area of the rectangular region is $4x'_{1n}\, y'_{1n} = \pi x_{1n}\, y_{1n}$, which is the same as the area of the elliptical integration region.

It is advantageous at this point to discuss the details of the computation for the position of the specular point. This point is used to define the direction of propagation of the multipath component, and will be important for the computation of the various required multipath parameters to be discussed subsequently. Figure II-1 shows the manner in which the specular point is computed for the specular ground reflection from flat terrain which is coplanar with the xy-plane. However, as mentioned previously, it has been assumed that the ground can be modeled as a series of rectangular, or triangular, surface elements of arbitrary orientation, in which case the specular

point location will not, in general, be identical to that shown in Fig. II-1. It is easy to see that the specular point, as computed in Fig. II-1, is located at a distance $h_t r/(h_t + h_r)$ in front of the transmitting antenna, as shown in Fig. II-2b. The algorithm used to locate the actual specular point is as follows:

(1) The specular point location in the xy-plane is determined as indicated in the geometry of Fig. II-1.

(2) The plane surface element which contains the point given in (1) is determined.

(3) The specular point is located in an infinite plane which is coplanar with the surface element found in (2).

If the specular point found in (3) does not lie in the surface element found in (2), then the specular point is repositioned to the closest point in the surface element when computing the various required multipath parameters to be discussed subsequently. In addition, if either the transmitter or receiver lie below an extension of the tilted planar facet determined in (2), then the specular point is computed relative to flat terrain which is coplanar with the xy-plane, as indicated in (1). It is also important to note that the determination of the Fresnel ellipse, as indicated in Eqs. (II-14) through (II-16), is accomplished in the planar facet determined in (2), and then this region is projected back into the xy-plane.

The details of the method used to compute the position of the specular point for an arbitrarily tilted ground facet are given in Appendix A. In addition, the details of the method for determining whether a surface element

contains a point in the xy-plane are given in Appendix C. This latter computation is also required in the numerical integration procedure in order to associate an integration point with its appropriate surface element.

The total reflection coefficient is defined as

$$\rho_s = E_s/E_o \quad . \tag{II-19}$$

Using the previously mentioned modifications of the Fresnel-Kirchoff diffraction formula given in Eqs. (II-7) and (II-10), and taking the transmitter antenna pattern into account, we may use Eq. (II-6) to write

$$\rho_s = \frac{jr_o}{\lambda} \iint_{\substack{\text{appropriate} \\ \text{integration} \\ \text{region}}} \frac{1}{R_r R_t} \varepsilon^{-jk(R_r + R_t - r_o)} G(\alpha,\beta)\, G_A(\alpha',\beta')$$

$$\cdot \rho_r R_{eq} \frac{\cos\theta_t + \cos\theta_r}{2} dS \quad , \tag{II-20}$$

where $G(\alpha,\beta)$ is the transmitter antenna pattern for the radiated field, α and β are the planar azimuth and elevation angles, respectively, for the vector $\vec{R}_t$ measured relative to a coordinate system centered on the transmitter antenna, $G_A(\alpha',\beta')$ is the aircraft receiver antenna pattern, α' and β' are the planar azimuth and elevation angles, respectively, for the vector $\vec{R}_r$ measured relative to a coordinate system centered on the receiver antenna, cf. Fig. II-1. For convenience of exposition, a detailed discussion of the effect of the transmitter and receiver antenna patterns, on the various computational

procedures, is given in Appendix K. Thus, in the ensuing discussions it may be assumed throughout, unless otherwise noted, that the transmitter and receiver antenna patterns are omnidirectional, i.e., $G(\alpha,\beta) = 1$, for all α,β, and $G_A(\alpha',\beta') = 1$, for all α',β'.

It should be noted that in Eq. (II-20) the relative complex dielectric constant, ε_r, in determining R_{eq}, and the root-mean-square roughness height, σ_h, are different on the various surface elements, but are considered to be constant on any particular surface element. The integral in Eq. (II-20) was evaluated numerically by means of a two-dimensional approximating summation. A uniform rectangular mesh of 25 x 11 points, with 25 points in the x-direction and 11 points in the y-direction, was found to be adequate for the evaluation of the double sum. This density of points for this grid was determined experimentally from computer runs.

It is also necessary to point out that the entire procedure based on Eq. (II-20) depends very heavily on the assumption that the major contribution to the integral in Eq. (II-6) occurs near the specular point. In addition, we must have near-specular reflection from all of the surface elements in order to use the Fresnel reflection coefficients given in Eqs. (II-8) through (II-11).

B. Computation of Multipath Parameters

We now indicate the manner in which the various multipath parameters of interest are computed. The formula for ρ_s given in Eq. (II-20) is approximate and, in addition, no account has been taken of the movement of the aircraft antenna along the flight path. Hence, the phase of the specular ground reflection cannot be obtained precisely. However, as an approximation, the magnitude,

V_s, and phase shift, ψ_s, both relative to the direct wave of the specular ground reflection may be computed as

$$V_s = |\rho_s| \quad , \tag{II-21}$$

$$\psi_s = \text{ARG}\{\rho_s\} + \frac{2\pi}{\lambda}[\, r_{10} + r_{20} - r_o] \quad . \tag{II-22}$$

The planar azimuth and elevation angles for the specular ground reflection, denoted by α_t, β_t, respectively, are computed according to the vector direction between the transmitter and the specular point on the ground, as shown in Fig. II-3. These angles are also known as the planar directional angles of the multipath component. The particular axes shown in Fig. II-3, in which the origin is at the stop end of the runway and the x-axis is along the centerline of the runway, are termed the standard coordinate system and are used whenever specifying the locations of the obstacles for the computer simulation program. We see from Fig. II-3 that the planar directional angles are given by

$$\alpha_t = \tan^{-1}(R_{ty}/R_{tx}) \quad , \tag{II-23}$$

$$\beta_t = \tan^{-1}(R_{tz}/R_{tx}) \quad . \tag{II-24}$$

It is also of interest to compute the planar azimuth and elevation incidence angles of the specular ground reflection, denoted by α_r,β_r, respectively, relative to a coordinate system aligned along the velocity vector of the receiver aircraft, as shown in Fig. II-3. We see from Fig. II-3 that these planar directional angles are given by

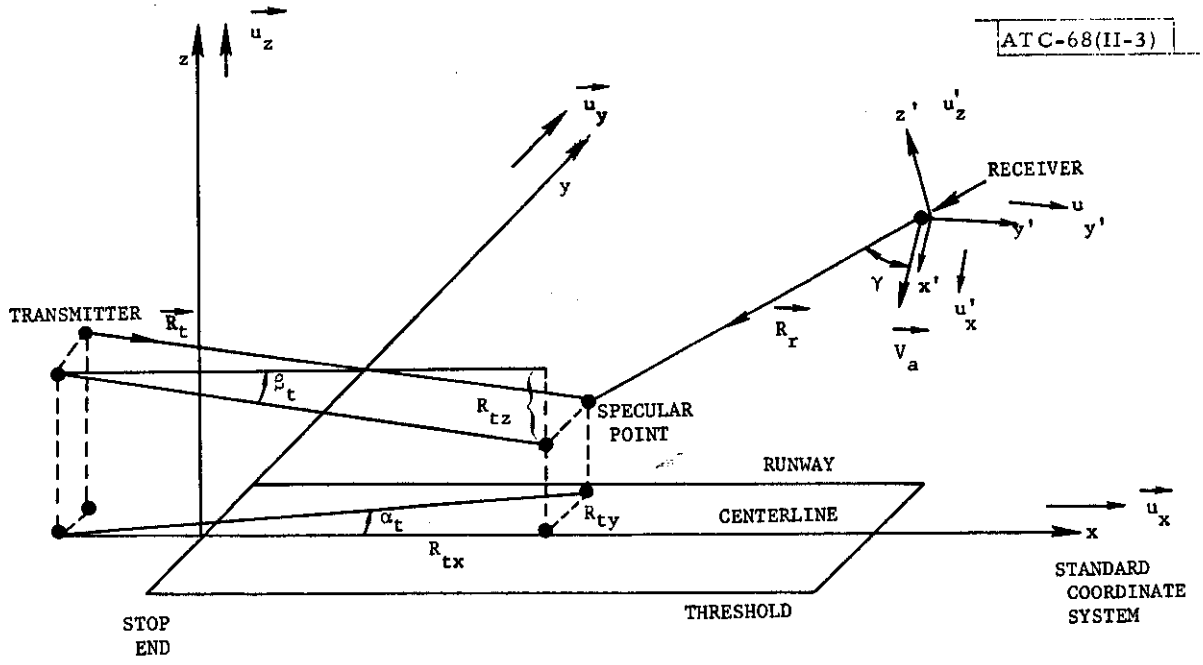

$\vec{V}_A$ is aircraft velocity vector

$\vec{u}_x$, $\vec{u}_y$, $\vec{u}_z$ are unit vectors in x,y,z directions respectively

$\vec{R}_t = R_{tx}\,\vec{u}_x + R_{ty}\,\vec{u}_y + R_{tz}\,\vec{u}_z$

$\vec{u}_{x'}$, $\vec{u}_{y'}$, $\vec{u}_{z'}$ are unit vectors in x', y', z' directions, respectively

$\vec{R}_r = R_{rx'}\,\vec{u}_{x'} + R_{ry'}\,\vec{u}_{y'} + R_{rz'}\,\vec{u}_{z'}$

Fig. II-3. Method for computing planar directional angles and Doppler frequency.

$$\alpha_r = \tan^{-1}(R_{ry'}/R_{rx'}) , \qquad \text{(II-25)}$$

$$\beta_r = \tan^{-1}(R_{rz'}/R_{rx'}) . \qquad \text{(II-26)}$$

The planar azimuth and elevation incidence angles, α_r, β_r, are required if it is desired to apply the multiplicative effect due to a receiver antenna pattern, $G_A(\alpha', \beta')$.

The fractional receiver Doppler frequency is computed according to the velocity of the aircraft receiver, relative to the velocity of light, projected along the direction of arrival of the multipath signal at the receiver, and is given by

$$\omega'_{SD} = \frac{\omega_{SD}}{\omega} = \frac{1}{c} \vec{V}_A \cdot \vec{R}_R / |\vec{R}_R| = \frac{V_A}{c} \cos(\gamma) \quad , \qquad \text{(II-27)}$$

where $\vec{V}_A$ is the vector aircraft velocity, and $V_A = |\vec{V}_A|$. In order to obtain the time delay, t_{SD}, of the specular ground reflection relative to the direct wave, it is assumed, as an approximation, that it arrives at the receiver along the direction defined by the specular point of reflection, so that, cf. Fig. II-1,

$$t_{SD} = \frac{1}{c}(r_{10} + r_{20} - r_o) \quad . \qquad \text{(II-28)}$$

The multipath subroutines have been designed to be system-independent, i.e., their output applies only to the particular airport scenario, or environment, which is of interest. It is for this reason that the fractional receiver Doppler frequency ω'_{SD} and not ω_{SD} is computed in the multipath subroutines. That is, in order to have the multipath subroutines be system-

independent, the effect of the transmitter frequency, ω, must be applied in the system subroutines, in which the errors due to multipath are computed for particular systems, as indicated in Eq. (II-27), $\omega_{SD} = \omega\, \omega'_{SD}$.

C. Focusing Ground Effect Option

It has been mentioned previously in Section IIA that the ground has been modeled as a series of rectangular and triangular surface elements, each of which can be oriented in an arbitrary direction. In addition, each surface element is characterized by its own relative complex dielectric constant and root-mean-square roughness height. A numerical integration is performed over these surface elements, as indicated in Eq. (II-20), to obtain the complex amplitude of the specular ground reflection.

However, in some situations it is appropriate to obtain more than just a single specular ground reflection component for ground which has been modeled as a series of rectangular and triangular surface elements. It is possible to employ the computer program to get multiple specular ground reflections by using the focusing ground effect option, which will now be described in detail.

As an input parameter to the program, each surface element is assigned a tag, which may be, say, either a zero, or one. The region of the ground which does not lie within any of the surface elements is termed the default region of the ground and is assigned a tag of zero. Let us suppose that N surface elements have been given a tag of unity. A primary specular ground reflection is formed, as well as N secondary specular ground reflections, as follows. The integrand in Eq. (II-20) is evaluated, at some mesh point, corresponding to one of the mesh points contained within the integration region

discussed previously, on some surface element, and is assigned to the primary specular ground reflection provided that the surface element has a tag of zero. A summation of all such contributions from the various mesh points is formed to obtain the primary specular ground reflection. This multipath component has a specular point associated with it as described previously, so that all multipath parameters can be obtained as indicated in Eqs. (II-21) to (II-28).

The N secondary specular ground reflections are obtained by evaluating the integrand in Eq. (II-20), at some mesh point on some surface element that has a tag of unity, and summing these individual contributions in the appropriate way. Each secondary specular ground reflection has a repositioned specular point assigned to it in the following manner. A specular point is computed, for the k-th secondary specular ground reflection, relative to an infinite plane coplanar with the surface element associated with this k-th component. If this specular point does not lie on the associated surface element, then it is repositioned to the nearest point on this surface element. Once this specular point has been assigned, it is possible to compute the multipath parameters as indicated in Eqs. (II-21) to (II-28). This procedure thus leads to a total of (N+1) primary plus secondary specular ground reflection components, each component containing eight multipath parameters computed according to Eqs. (II-21) to (II-28). This option is important for those situations in which the ground can be modeled as a series of surface elements and there are multiple ground reflections which can be obtained therefrom.

D. Simple Fresnel Reflection - Roughness Coefficient Computation

The computational procedures which have been presented previously in Sections IIA - IIC require a complex numerical integration over various surface elements in order to obtain the multipath parameters for the specular ground reflection. These calculations require a considerable amount of computer time, on the order of about 0.1 seconds of IBM 370/168 computer time for a given flight evaluation point, as indicated in Section VIII. In some situations it is appropriate to eliminate this complex algorithm and to use one which is considerably simpler, and thus requires much less computer running time. Towards this end, an option has been incorporated into the program which enables the complex specular ground reflection coefficient, ρ_s, to be calculated in the following manner.

$$\rho_s = \rho_r \cdot R_V(\theta_t) \quad , \quad \text{(vertical polarization)},$$

$$= \rho_r \cdot R_H(\theta_t) \quad , \quad \text{(horizontal polarization)}, \qquad \text{(II-29)}$$

where ρ_r is the attenuation factor due to the small-scale roughness, and is given in Eq. (II-7), and $R_V(\theta_t)$, $R_H(\theta_t)$ are the Fresnel reflection coefficients for vertical, horizontal polarization, respectively, given in Eqs. (II-8) and (II-9). The root-mean-square roughness height and relative complex dielectric constant used in this computation correspond to those for the default region of the ground which does not lie within the area defined by the rectangular and triangular surface elements. The specular point is computed for an

infinite flat ground plane as indicated previously in Section IIA. The various multipath parameters are computed as shown in Eqs. (II-21) through (II-28), with the sole exception that the phase shift is now obtained as $\psi_s = \text{ARG}\{\rho_s\}$.

E. Computer Validation Results

We now present some of the results obtained using the computer program which computes the multipath parameters for the specular ground reflection. The details of the operation of this subroutine can be obtained from the flow chart shown in Fig. II-4. For simplicity, we do not consider the focusing ground effect option in these computer validation results.

A presentation is first given of some of the important details concerning the operation of the program. We first mention that the integral in Eq. (II-20) is evaluated by means of an approximating summation with the summand evaluated on either an elliptic, or rectangular, grid, cf. Fig. II-2. When an elliptic grid is used, there is a constant stepping distance in the major-axis direction, and a constant number of grid points in the minor-axis direction. As mentioned previously, a total of 25 x 11 grid points were employed. When a rectangular grid is employed, the incremental distance along the longer side of the rectangle is 1/25 of this length, and the incremental distance is 1/11 of the shorter side of the rectangle in that direction. A two-dimensional Simpson algorithm was used to evaluate the two-dimensional integral of Eq. (II-20). A simple check for shadowing of the receiver from the transmitter by a tilted surface is also performed in the program, so that all such points which are shadowed do not contribute to the integral.

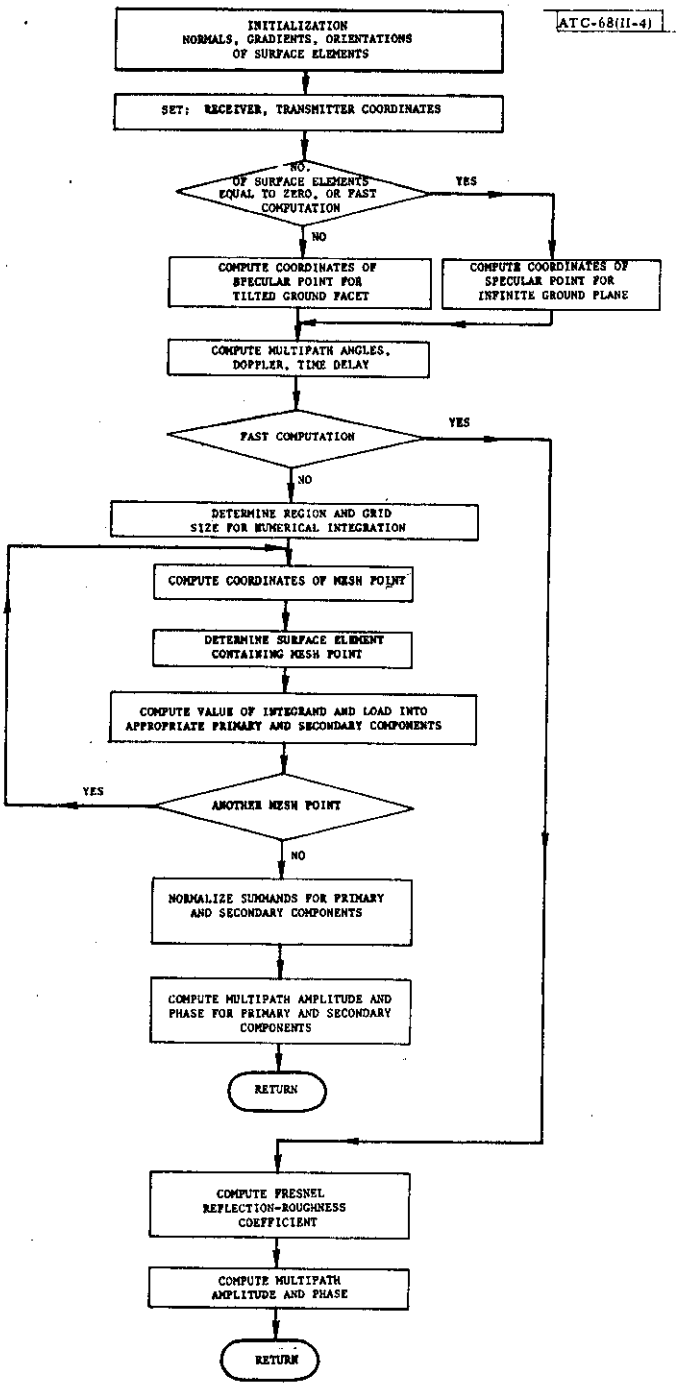

Fig. II-4. Flow chart for program which computes multipath parameters for specular ground reflection.

It should also be mentioned that there is an option in the program which enables the user to eliminate the time-consuming computation of the multipath amplitude and phase and compute only the other parameters for the specular ground reflection, such as planar directional angles, fractional Doppler frequency and time delay, cf. Fig. II-4. The computation of only these latter parameters involves only a small amount of computer time per flight evaluation point. If this option is used, then the amplitude and phase of the specular ground reflection must be obtained by some other means, such as recalling their values from machine storage for some previous calculation at a flight evaluation point reasonably close to the desired one.

In Fig. II-5 there are shown plots of the magnitude and phase of the integral given in Eq. (II-20), i.e., V_s, ψ_s, the magnitude and phase of the specular ground reflection, cf. Eqs. (II-21), (II-22), versus the number of Fresnel zones used in the numerical integration, for an elliptic grid. The results of these figures apply for vertical polarization, and for a smooth perfectly-conducting surface, i.e., $\sigma_h = 0$, $\varepsilon_R = 1$, $\varepsilon_I = 10^8$. The corresponding results for a rectangular integration region, as was discussed previously in Section IIA, are shown in Fig. II-6. In Figs. II-5 and II-6 there are also shown the corresponding theoretical curves which can be obtained by using the method of images and Babinet's principle, cf. Sommerfeld,[5] p. 204 and Silver,[7] p. 167, so that the problem of scattering from an elliptic, or rectangular, region of ground can be treated as that of diffraction through a circular, or square, aperture, respectively. These results are derived in Appendix D,

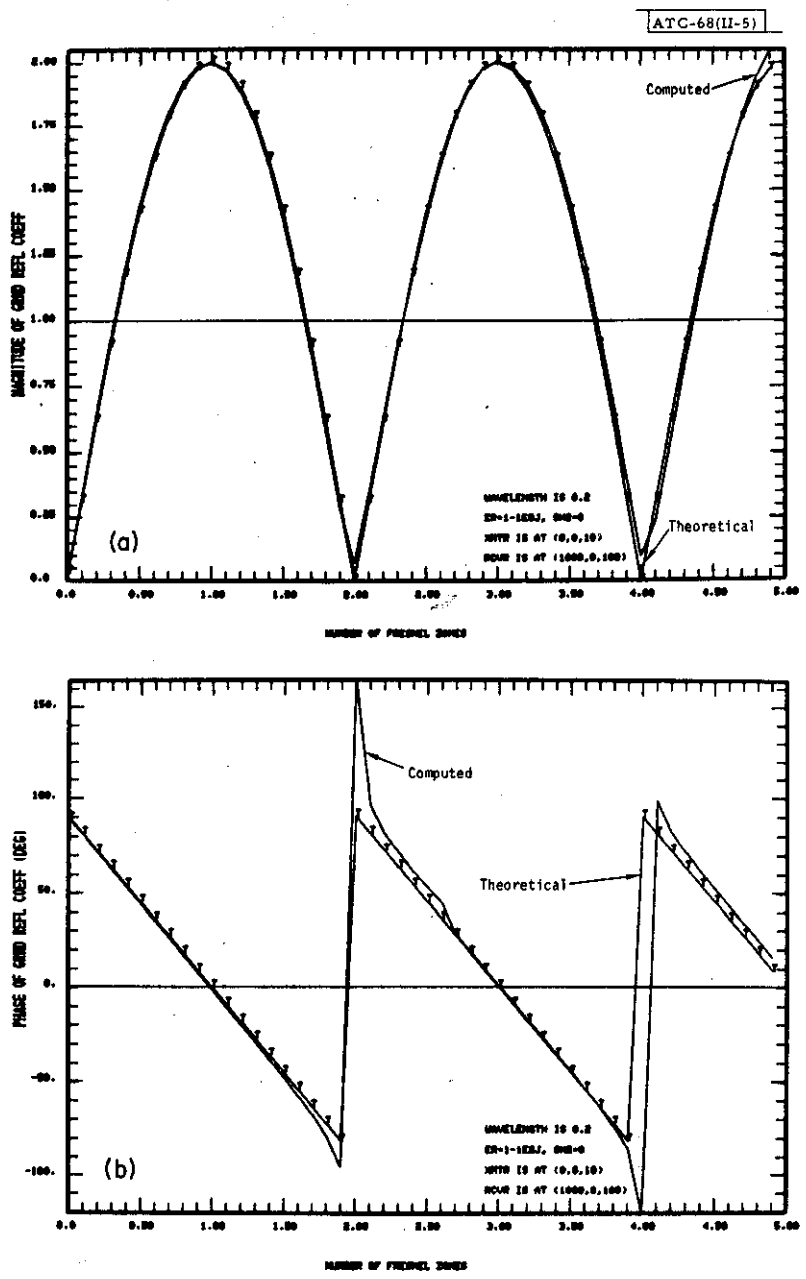

Fig. II-5. Comparison of computed and theoretical values of magnitude and phase of Fresnel-Kirchoff diffraction integral vs number of Fresnel zones used in elliptical integration region, for a flat, smooth, perfectly-conducting surface.

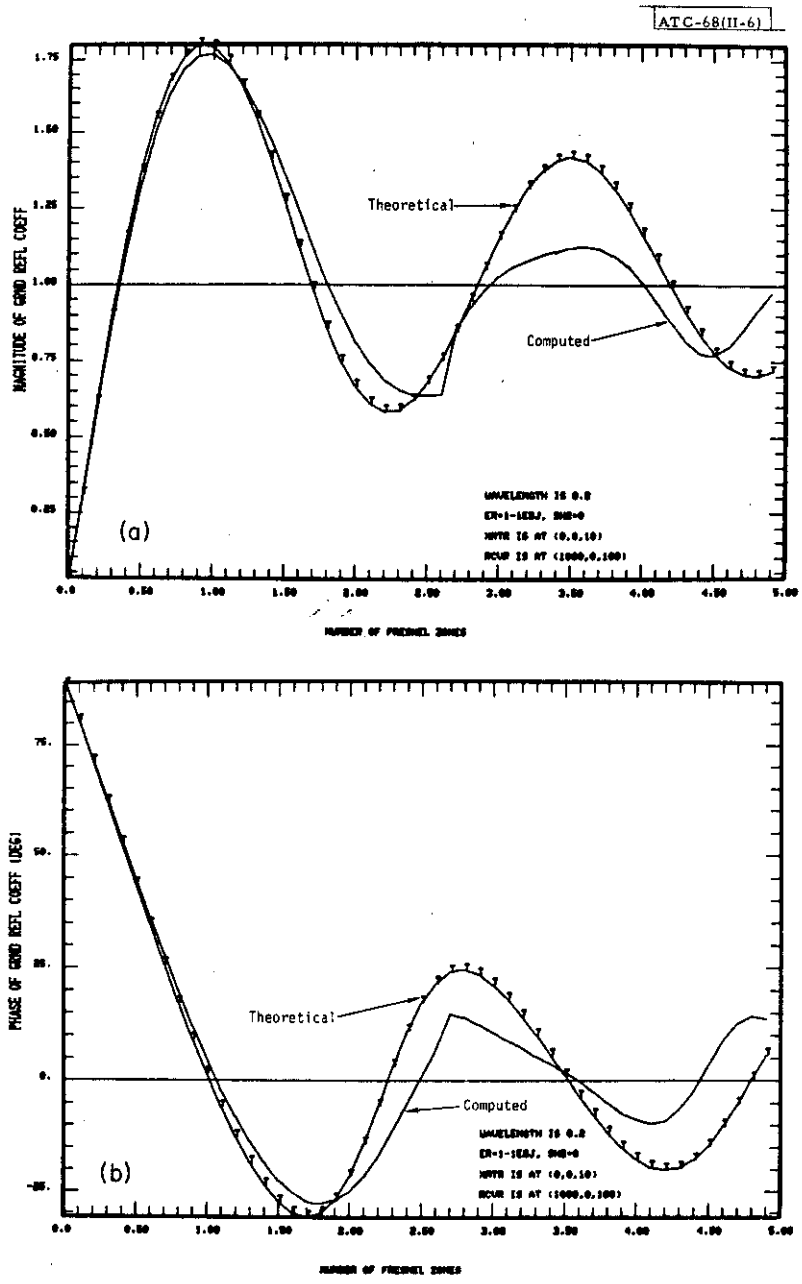

Fig. II-6. Comparison of computed and theoretical values of magnitude and phase of Fresnel-Kirchoff diffraction integral vs number of Fresnel zones used in rectangular integration region, for a flat, smooth, perfectly-conducting surface.

from which we obtain

$$V_s = 2\left|\sin\left(\frac{\pi}{2} N\right)\right| \quad , \text{ (circular aperture)} \qquad \text{(II-30)}$$

$$\psi_s = 90(1 - N + 2N') \quad , \text{ (circular aperture)} \qquad \text{(II-31)}$$

$$V_s = 2\left|F^2\left(\sqrt{\frac{\pi}{2} N}\right)\right| \quad , \text{ (square aperture)} \qquad \text{(II-32)}$$

$$\psi_s = 90 + \text{ARG}\left\{F^2\left(\sqrt{\frac{\pi}{2} N}\right)\right\} \quad , \text{ (square aperture)} \qquad \text{(II-33)}$$

where N represents the number of Fresnel zones, N' is the largest integer less than or equal to N/2, and F(x) is the Fresnel integral defined as follows, cf. Sommerfeld,[5] p. 239,

$$F(x) = \int_0^x \varepsilon^{-j\frac{\pi}{2} u^2} \, du \quad . \qquad \text{(II-34)}$$

It is seen from Figs. II-5 through II-6 that there is excellent agreement between the results of the computer program and the theoretical predictions for both the elliptic and rectangular integration regions. Similar results were obtained for other positions of the transmitter and receiver, such as (0, 0, 10) and (10000, 0, 100) for the transmitter and receiver positions, respectively.

The results in Fig. II-5 show that the magnitude and phase of the specular ground reflection oscillate indefinitely about the true values of unity

and zero, respectively, as the number of Fresnel zones, or integration region size, is increased. This is a very unfortunate behavior which is undesirable for the purpose of computing the magnitude and phase of the specular ground reflection. Fortunately, this problem does not exist for the rectangular integration region, as seen by the results in Fig. II-6. This figure shows that the magnitude and phase converge to the true values of unity and zero, respectively, as the number of Fresnel zones is increased. In addition, it is seen from Fig. II-6 that when the number of Fresnel zones is 2.8, the magnitude and phase are very close to the true values of unity and zero, respectively, i.e., the magnitude is about 0.92 and the phase is about 15°. It is for this reason that a rectangular integration region, extending over 2.8 Fresnel zones, is employed in the computer program.

Similar plots are shown in Figs. II-7 and II-8, for vertical polarization, and for a flat, smooth, concrete surface and for a flat, smooth, water surface, respectively. In these figures we have $\sigma_h = 0$, and $\varepsilon_r = 7 - 0j$, $75 - 36j$, respectively. The values obtained from Figs. II-7 and II-8, for the magnitude and phase, for N = 2.8 are in reasonable agreement with the asymptotic values, for a large number of Fresnel zones used in the integration, which can be obtained from the value computed for $R_v(\theta_t)$ as given in Eq. (II-8). These values are -0.524, -0.110j for the data given in Figs. II-7 and II-8, respectively. Thus the results of Figs. II-6 through II-8 provide some justification for using a rectangular integration region with 2.8 Fresnel zones as the region of integration in Eq. (II-20).

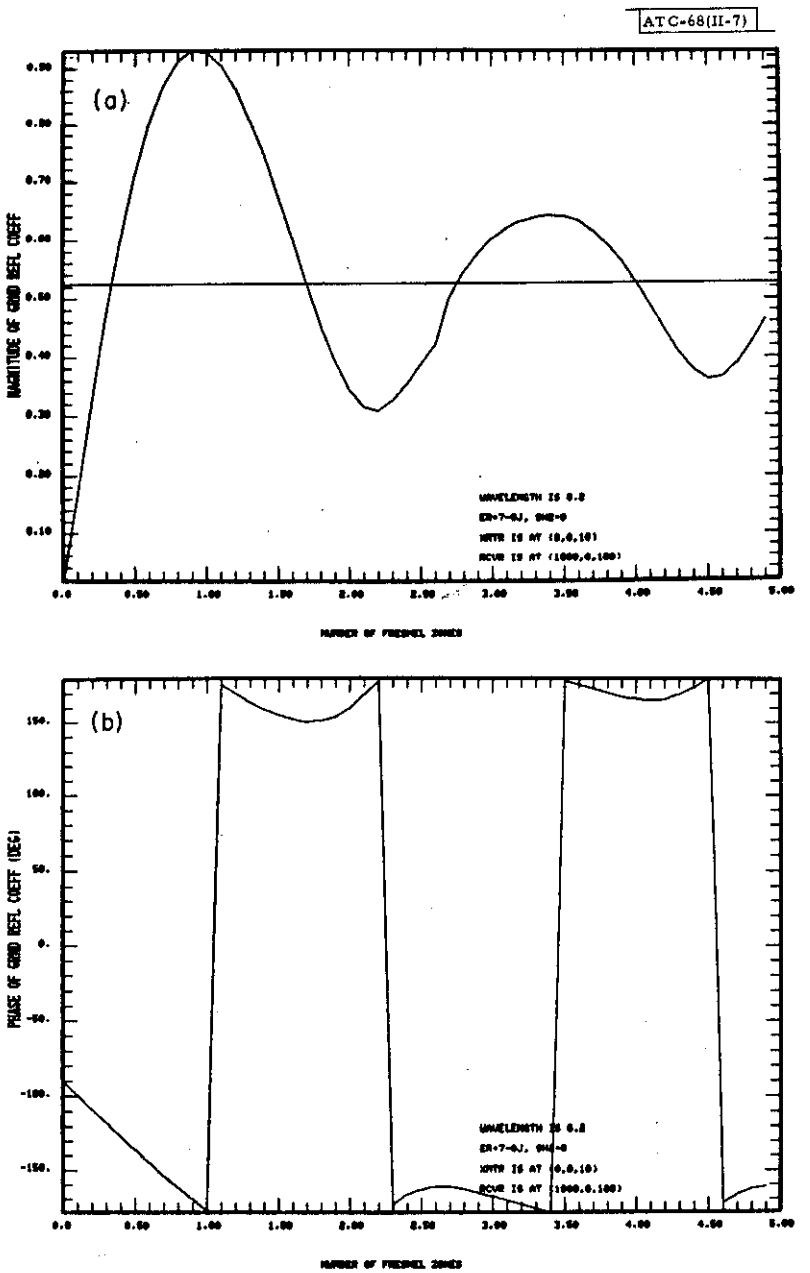

Fig. II-7. Magnitude and phase of Fresnel-Kirchoff diffraction integral vs number of Fresnel zones used in rectangular integration region, for a flat, smooth, concrete surface.

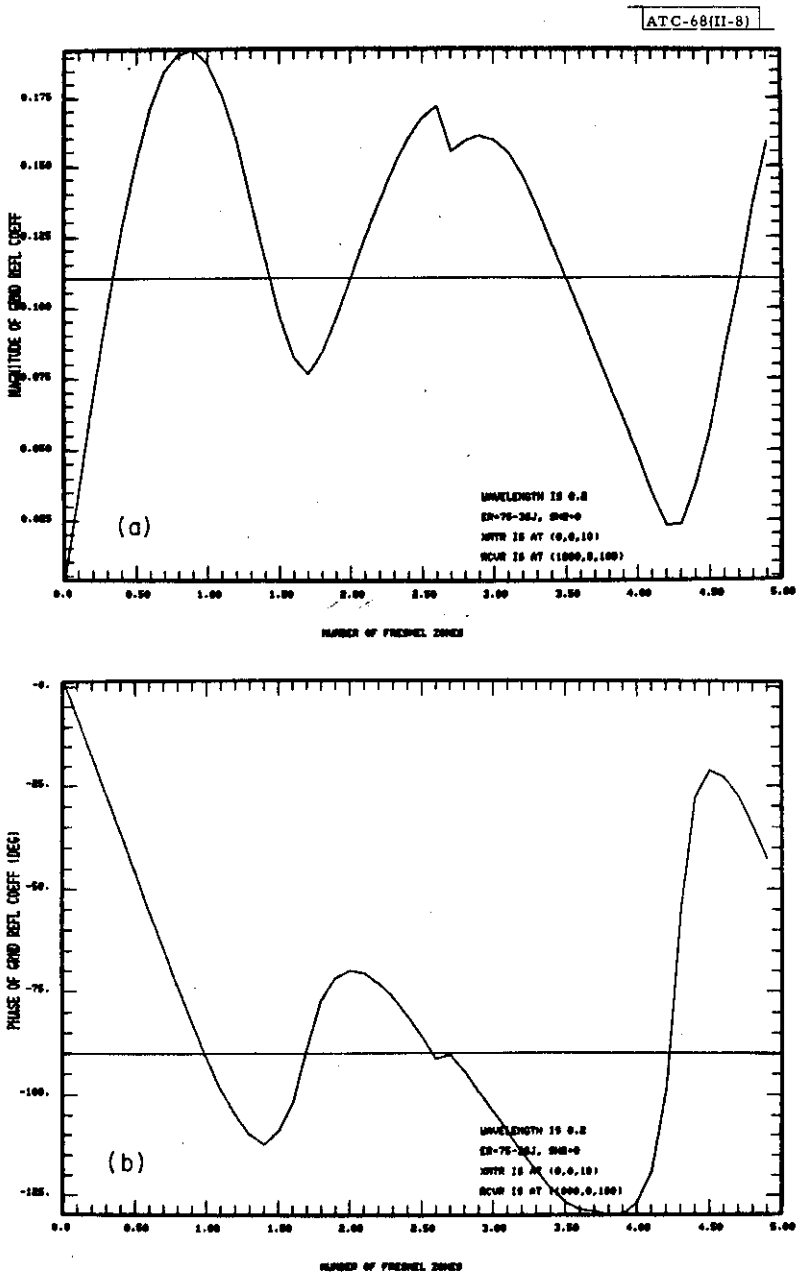

Fig. II-8. Magnitude and phase of Fresnel-Kirchoff diffraction integral vs number of Fresnel zones used in rectangular integration region, for a flat, smooth, water surface.

III. SCATTERING FROM BUILDINGS

A. Flat Plate Model for Buildings

We now consider the computations required to obtain the multipath propagation components due to scattering from buildings, or hangars. For the purpose of this computation, it is assumed that the building can be modeled as a rectangular flat plate as shown in Fig. III-1. Complex buildings may be modeled by several rectangular flat plates, each with appropriate tilt angle, dielectric constant and roughness specification. In such a case, independent computations are made for each plate by the method described here. This flat plate can be oriented at an arbitrary tilt angle with respect to the ground normal, as depicted in Fig. III-1. In addition, it is assumed that the building can be characterized by means of a root-mean-square roughness height and relative complex dielectric constant. The transmitting and receiving antennas are assumed to be on the same side of the building so that it is possible for scattering to take place, i.e., it is possible to determine the specular point shown in Fig. III-1. If the transmitter and receiver lie on opposite sides of the building, then there can be no scattered wave and its amplitude is set to zero.

B. Method Based On Diffraction By Rectangular Aperture

The following simplified method is to be used to get the magnitude and phase of the multipath signal, relative to the direct signal, due to scattering from buildings or hangars. The method is based on the method of images and Babinet's principle, cf. Sommerfeld,[5] p. 204 and Silver,[7] p. 167, which state that the problem of scattering from a rectangular building, or hangar,

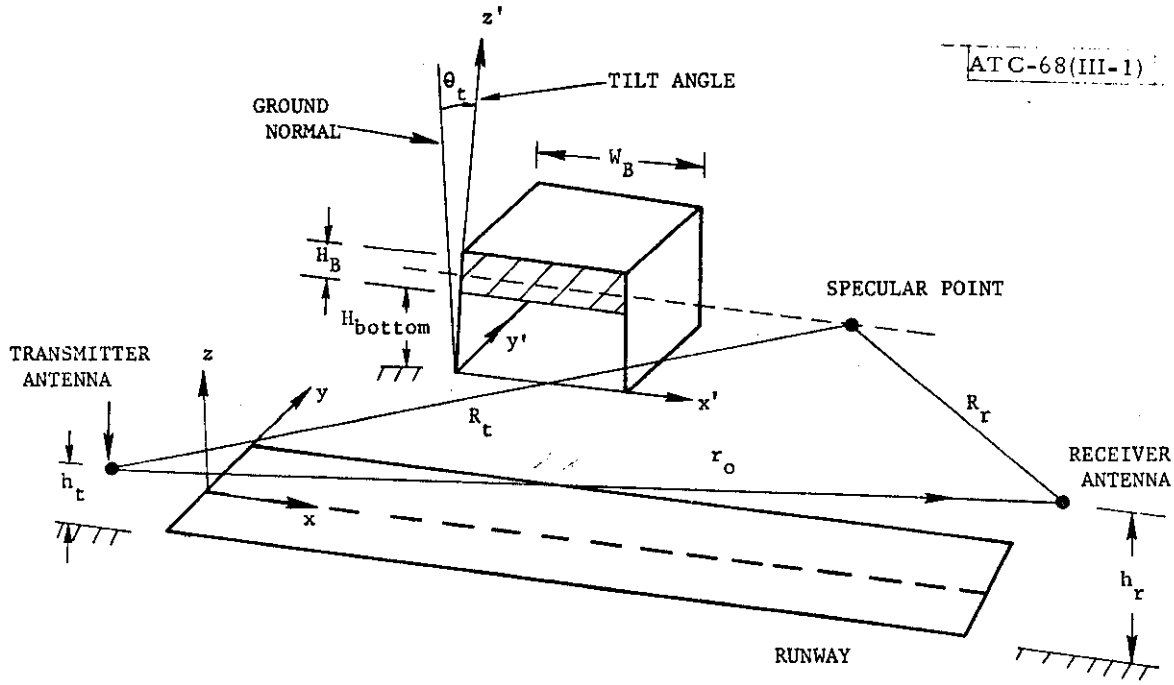

Fig. III-1. Configuration used to determine multipath parameters due to scattering from building.

as shown in Fig. III-1, can be equated to the problem of diffraction through a rectangular opening in an opaque screen. Strictly speaking, this principle applies only for a flat perfectly conducting surface. However, the variation in angle of incidence over the typical airport building surface is generally small enough to warrant inclusion of finite conductivity, and possibly roughness, by a multiplicative factor.

The diffraction problem, corresponding to the geometry shown in Fig. III-1, is depicted in Fig. III-2. The case of greatest practical interest is that of Fresnel diffraction, for which the received signal relative to the direct wave can be expressed as the following complex coefficient, cf. Sommerfeld,[5] pp. 237-247,

$$\rho_B = \rho_{Ba}\, \rho_{Be}\, \rho_R\, \rho_r\, \rho_t\, R_{eq} \quad , \qquad \text{(III-1)}$$

where R_{eq} is the equivalent Fresnel reflection coefficient which takes into account the finite dielectric and conductivity properties of the building surface as well as its arbitrary orientation and was given in Eqs. (II-10) and (II-11), ρ_t is the time delay factor given by

$$\rho_t = \varepsilon^{-jk(R_t + R_r - r_o)} \quad , \qquad \text{(III-2)}$$

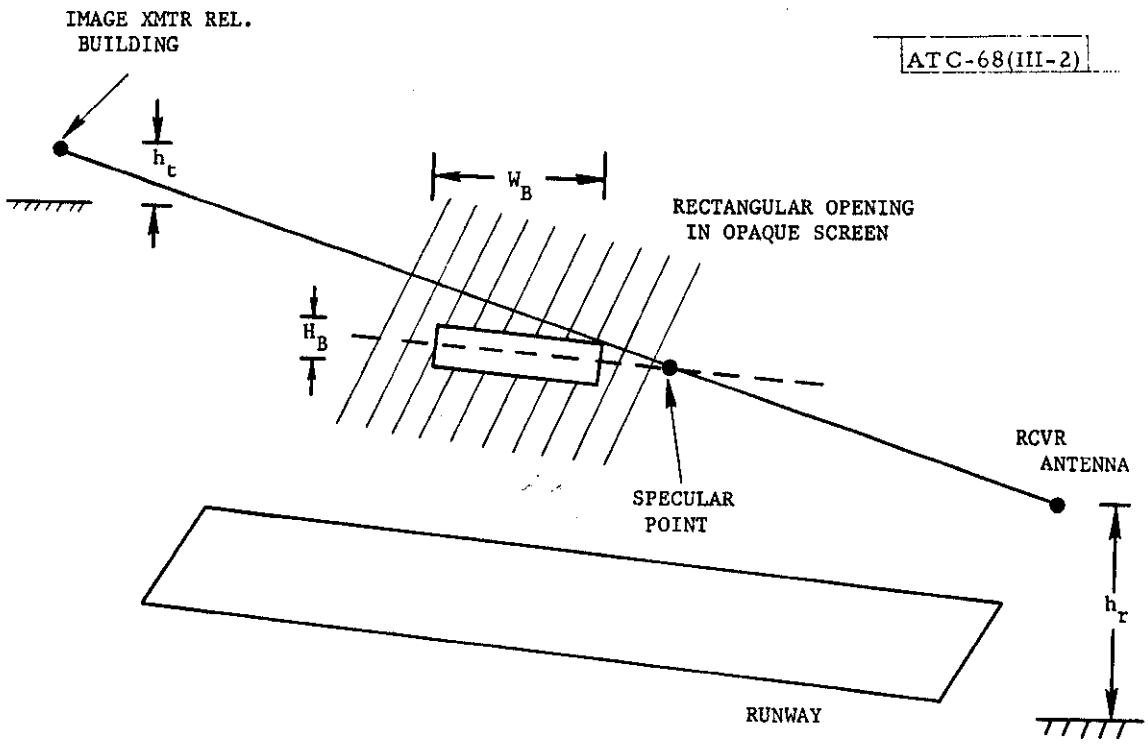

Fig. III-2. Diffraction problem assumed to be equivalent to that of scattering from building.

ρ_r is the attenuation factor due to the building surface roughness and was given in Eq. (II-7), ρ_R is a distance factor which takes into account the fact that a power loss occurs due to the greater path distance of the multipath signal relative to the direct wave, and is given by

$$\rho_R = \frac{r_o}{R_t + R_r} \quad , \tag{III-3}$$

β_{Be} is the elevation factor computed as

$$\rho_{Be} = \epsilon^{j\pi/4}(F(u_{top}) - F(u_{bot}))/\sqrt{2} \tag{III-4}$$

where F(u) is the Fresnel integral defined previously in Eq. (II-34) and

$$u_{top} = \sqrt{2}(H_{bottom} + H_B - h_s)(1 - \beta_1^2)^{1/2}/R_f \quad , \tag{III-5}$$

$$u_{bot} = \sqrt{2}(H_B - h_s)(1 - \beta_1^2)^{1/2}/R_f \quad , \tag{III-6}$$

$$R_f = \sqrt{\lambda \frac{R_t R_r}{R_t + R_r}} \quad , \tag{III-7}$$

h_s is the height of the specular point above the ground, shown in Fig. III-3, and ρ_{Ba} is the azimuthal factor computed as

$$\rho_{Ba} = \varepsilon^{j\pi/4} (F(u_{right}) - F(u_{left}))/\sqrt{2} \quad , \qquad \text{(III-8)}$$

where

$$u_{right} = \sqrt{2}(W_B - W_s)\ (1 - \alpha_1^2)^{1/2}/R_f \quad , \qquad \text{(III-9)}$$

$$u_{left} = -\sqrt{2}W_s\ (1 - \alpha_1^2)^{1/2}/R_f \quad , \qquad \text{(III-10)}$$

α_1, β_1 are the direction cosines of the line of sight, between image transmitter and receiver, relative to the x', z'-axis, respectively, and W_s is the directed distance between the specular point and the left-hand edge of the building, shown in Fig. III-4. The details of the method used to determine the position of the specular point for scattering from buildings are given in Appendix E. In writing Eq. (III-1) it has been assumed that the transmitter antenna pattern can be removed from inside the Fresnel-Kirchoff diffraction integral, as was done in Section II. The justification for this assumption is provided in Appendix K.

It should be mentioned that the diffraction formulas given for ρ_{Be}, ρ_{Ba} in Eqs. (III-4) and (III-8) are approximations which are valid when either α_1, or β_1, or both are zero. These formulas are derived from diffraction formulas in physical optics, cf. Sommerfeld,[5] pp. 237-247, for which the line of

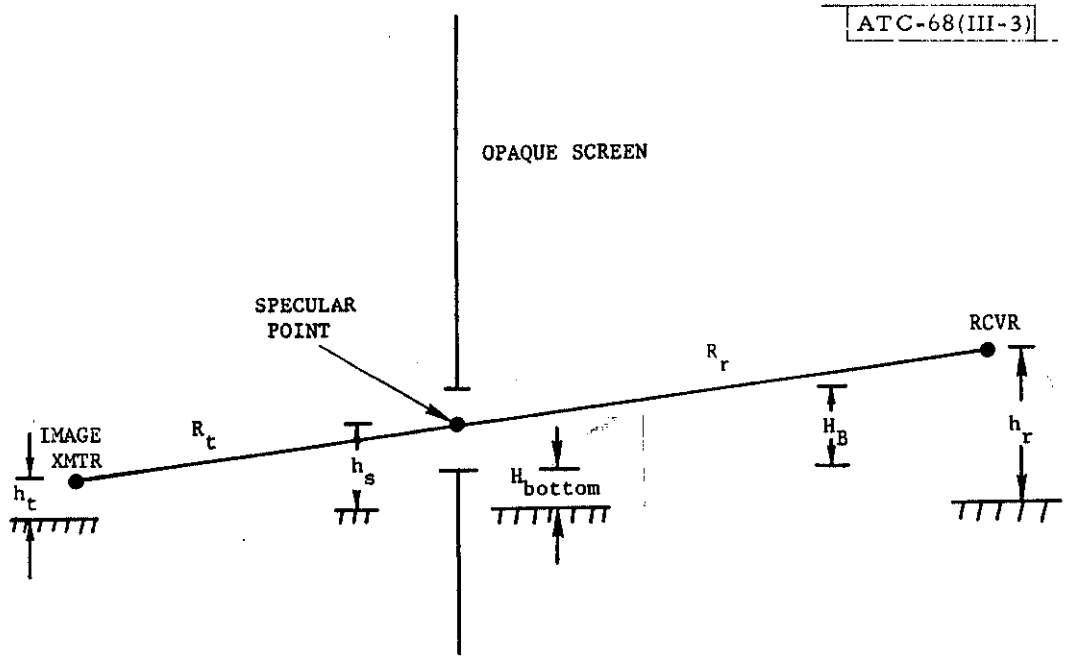

Fig. III-3. Side view of the geometry for computing elevation factor ρ_{Ba} for scattering from building.

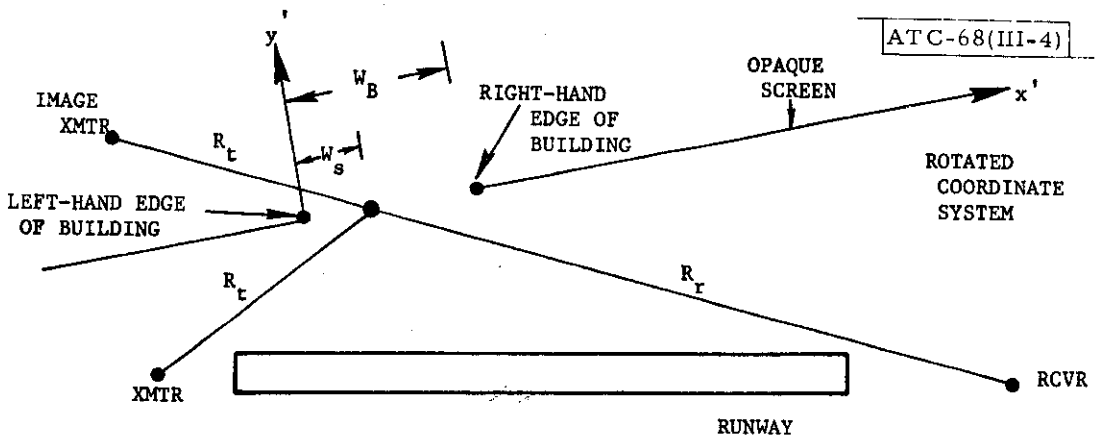

Fig. III-4. Top view of geometry for computing azimuthal factor ρ_{Ba} for scattering from building.

sight between the source and the observer lies in a plane which is perpendicular to the plane containing the diffraction aperture and parallel to one of the edges of the aperture. It is only when this condition is true that the two-dimensional diffraction integral can be factored into a product of one-dimensional Fresnel integrals as given previously. When this condition is not true, then it is necessary to express the diffraction integral as a Fresnel surface integral, which leads to greatly complicated computational procedures. These points are discussed in detail in Appendix F, where it is shown that the preceding approximations for the diffraction formulas are reasonably valid for a wide variety of conditions.

If the position of the specular point lies within the region defined by the front face of the building, then its position is not changed. However, if this is not the case, then it is repositioned as follows. If $h_s < H_{bottom}$, then h_s is set equal to H_{bottom}; if $h_s > H_B + H_{bottom}$, then h_s is set equal to $H_B + H_{bottom}$; if $W_s < 0$, then W_s is set equal to 0, and if $W_s > W_B$, then W_s is set equal to W_B. The justification for repositioning the specular point in this manner is based on the geometric theory of diffraction.[8]

C. Computation of Multipath Parameters

The amplitude and phase of the multipath component due to scattering from each building are given by

$$V_B = |\rho_B| \quad , \tag{III-11}$$

$$\psi_B = \text{ARG}\{\rho_{Ba}\rho_{Be}R_{eq}\} + k(R_t' + R_r' - R_t - R_r), \tag{III-12}$$

where R_t', R_r' are the distances from the repositioned specular point to the transmitter, receiver, respectively. If the specular point is not repositioned, then we have, of course, $R_t' = R_t$, $R_r' = R_r$. The computations required for the planar directional angles, fractional Doppler frequency and relative time delay are similar to those for the specular ground reflection given previously in Eqs. (II-23) - (II-28). However, it should be noted that these parameters are computed using the repositioned specular point. If there is no repositioning, then, of course, the original specular point is used to derive these parameters.

D. Inclusion Of Ground Reflections

The computations presented previously in this section refer to a ray path which extends from the transmitter to the building, or obstacle, and then to the receiver. This ray path may be denoted as X-O-R. In addition to this ray path, computations must be performed for three other ray paths which involve ground reflections, as indicated in Fig. III-5. One of these ray paths includes a ground reflection between transmitter and obstacle, denoted as X-G-O-R, the second ray path involves a ground reflection between obstacle and receiver, denoted as X-O-G-R, and the third ray path includes ground reflections between transmitter and obstacle and between obstacle and receiver, denoted as X-G-O-G-R, cf. Fig. III-5. The multipath parameters for these other three ray paths are computed in much the same manner as the X-O-R path by using appropriate combinations of transmitter, image transmitter, receiver, or image receiver positions, as will now be described in detail. It should be pointed out that it is well known from the mathematical models of Instrument Landing System (ILS) multipath and experimental radar cross section determinations, cf. Ref. 9 , that significant errors can occur if these additional ground reflection terms are ignored.

One possible means of handling the ground reflections, as shown in Fig. III-5, would be the Fresnel-Kirchoff diffraction integral approach outlined in Section II. However, this is rather unattractive from a computational viewpoint since it would have to be applied simultaneously to the hangar and both ground locations in all cases, including those in which the multipath amplitude is rather low due to the particular geometry. Consequently,

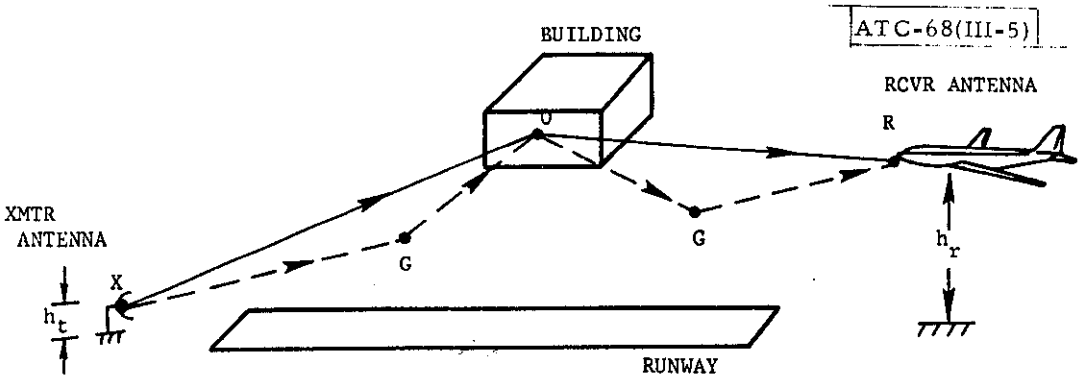

Fig. III-5. Possible ray paths for ground reflections from a vertical structure.

we have instead chosen a simpler approach based on the method of images and Babinet's principle, cf. Refs. 5 and 7. In essence, the idea is as follows:

1. To handle path X-G-O-R, we consider the signal to be transmitted from an image transmitter located beneath the given transmitter and received by the actual aircraft. The image antenna phase center is located a distance of $2h_t$ beneath the actual transmitter. The signal radiated by the image transmitter is attenuated by ρ_{1g} and shifted in phase by ϕ_{1g} where

   ρ_{1g} = effective reflection coefficient magnitude for ground at geometric angle of reflection for path X-G-O-R. (This takes into account the ground roughness and dielectric properties.)

   $= \rho_r \cdot R_{eq}$

   ϕ_{1g} = phase change on reflection from ground for path X-G-O-R.

   $= \text{ARG}\{R_{eq}\}$

2. To handle path X-O-G-R, we consider the signal to be transmitted by the actual transmitter and received by an image aircraft located at a distance of $2h_r$ below the actual aircraft. The signal received by the image aircraft is attenuated by ρ_{2g} and shifted in phase by ϕ_{2g}, where ρ_{2g} and ϕ_{2g} are the analogs to ρ_{1g} and ϕ_{1g} for path X-G-O-R.

3. To handle path X-G-O-G-R, we consider the signal to be transmitted by an image transmitter located a distance of $2h_t$ beneath the actual transmitter, and received by an image aircraft located at a distance of $2h_r$ below the actual aircraft. The signal radiated by the image transmitter is attenuated by ρ_{1g} and shifted in phase by ϕ_{1g}, while the signal received by the image aircraft is attenuated by ρ_{2g} and shifted in phase by ϕ_{2g}.

The net received multipath signal then consists of four distinct components corresponding to the ray paths X-O-R, X-G-O-R, X-O-G-R, X-G-O-G-R, as shown in Fig. III-5.

In Fig. III-6 we illustrate graphically the four ray paths to be considered. The computations required to determine the multipath components for the three paths X-G-O-R, X-O-G-R, X-G-O-G-R are similar to those for the ray path X-O-R which were presented previously in this section, except for the following minor modifications. The positions of the transmitter, or receiver, or possibly both, are changed to their locations as indicated previously and illustrated in Fig. III-6. The computational procedure is used as before, but with these new positions employed in the computations. In addition, the multipath amplitudes for the paths X-G-O-R, X-O-G-R, X-G-O-G-R are multiplied by ρ_{1g}, ρ_{2g} and $\rho_{1g}\,\rho_{2g}$, respectively, where these quantities are computed in a manner similar to that for ρ_r given in Eq. (II-7) and R_{eq} given in Eqs. (II-10) and (II-11). The procedure used to determine the relative phase shift, planar directional angles, fractional Doppler frequency, and

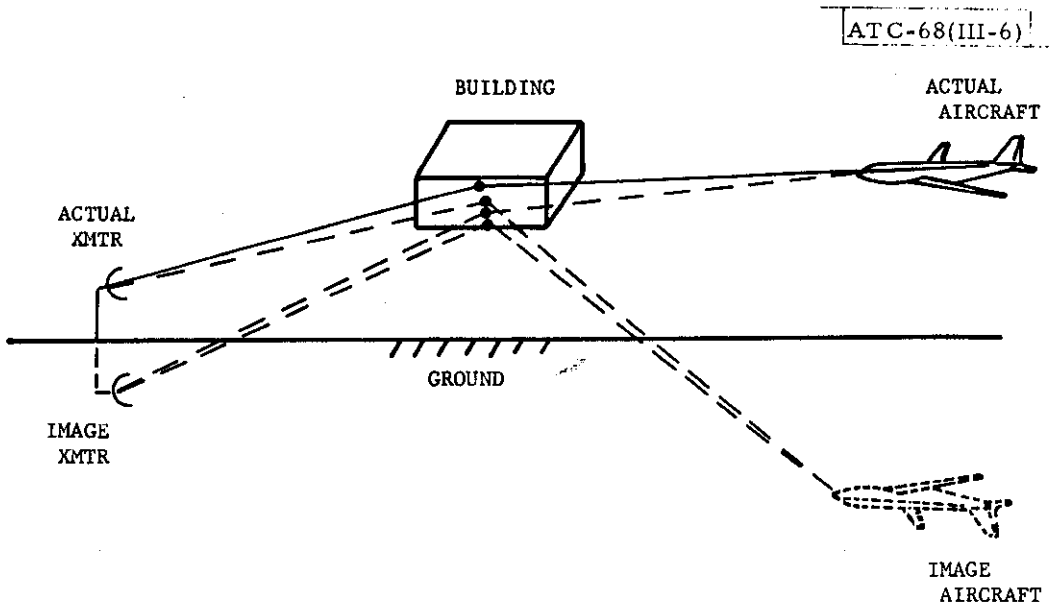

Fig. III-6. Method of images applied to ground reflections.

time delay for the multipath components for these three ray paths is similar to that given previously in Eq. (III-16) and Eqs. (II-23) - (II-28). However, we point out once again that the relative phase shift for these three multipath components is increased by ϕ_{1g}, ϕ_{2g}, and $\phi_{1g} + \phi_{2g}$, respectively, where these phase angles are due to the reflection from the ground and are computed, respectively as ARG$\{R_{eq1}\}$, ARG$\{R_{eq2}\}$, ARG$\{R_{eq1}\}$ + ARG$\{R_{eq2}\}$, where R_{eq1}, R_{eq2} correspond to the ground reflection between transmitter and obstacle, and between obstacle and receiver, respectively.

The results of certain field measurements have shown that building or aircraft multipath levels, as a function of height, can be substantially altered by non-flat terrain off the runway. However, the ground reflection model described above assumes that the ground off the runway is at the same height as the runway. This is generally not the case. For example, the FAA suggests a dropoff at the runway edge to drain the rain which can accumulate. It has been pointed out by Horonjeff[10] that certain airports show cases where the terrain 200 feet off the runway is 5 feet, or 25λ at C-band, below that of runway centerline.

A simple way in which this effect can be taken into account in the model is to add a differential height parameter ΔZ_g to the description of each building and aircraft. When computing the multipath parameters involving ground reflections, the image transmitter would be at a height of

$$h_t \text{ (image)} = -h_t + 2\Delta Z_g \quad , \qquad \text{(III-13)}$$

and the image receiver would be at a height of

$$h_r(\text{image}) = -h_r + 2\Delta Z_g \quad . \qquad \text{(III-14)}$$

The actual computational procedure for obtaining the multipath parameters for the ray paths X-G-O-R, X-O-G-R, X-G-O-G-R, is similar to that described previously.

This summarizes the numerical algorithms used to include ground reflections for multipath from vertical structures. A few observations are in order regarding the approximations made. The use of image theory is strictly valid only for perfect conductors. For non-perfect conductors there is an error that depends on the Fresnel reflection coefficient for the given surface. It is believed that this error is small if appropriate use is made of the reflection coefficient associated with the specular point for the ground reflection.

E. Comparison Of Results With Experiments And Geometric Diffraction Theory

We now wish to present some computer validation results for the computational procedures presented in Sections II A-D. An idea can be obtained of the operation of this computer program from the flow chart shown in Fig. III-7. In order to present the computer validation results, we employ some data obtained by ITT/Gilfillan[11] for obtaining reflections from an airport building using the geometric theory of diffraction.[8] These data are shown in Fig. III-8

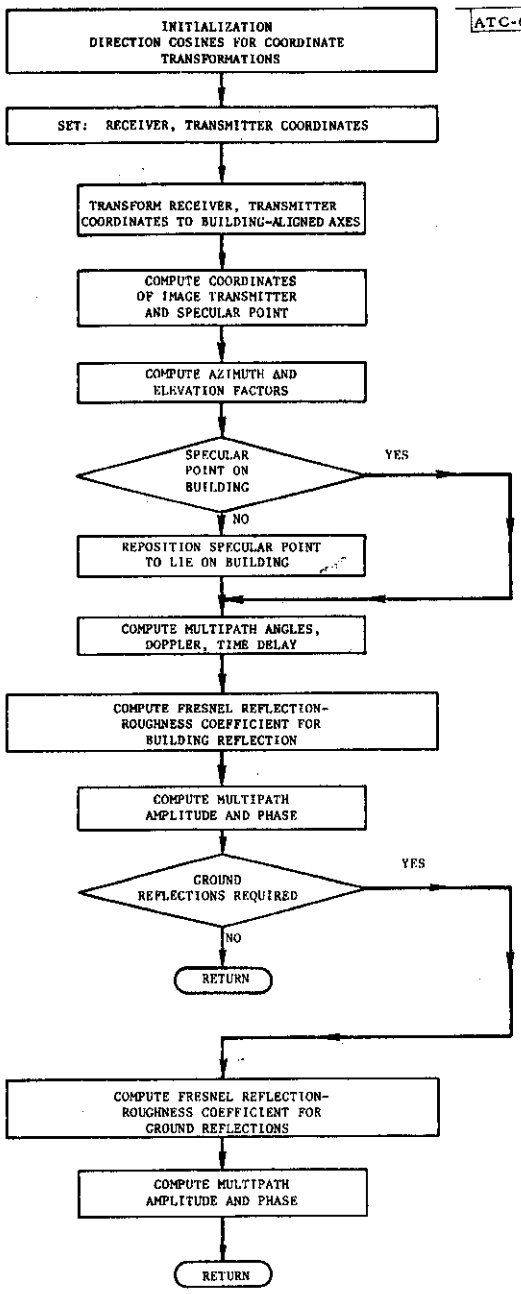

Fig. III-7. Flow chart for program which computes multipath parameters for scattering from building.

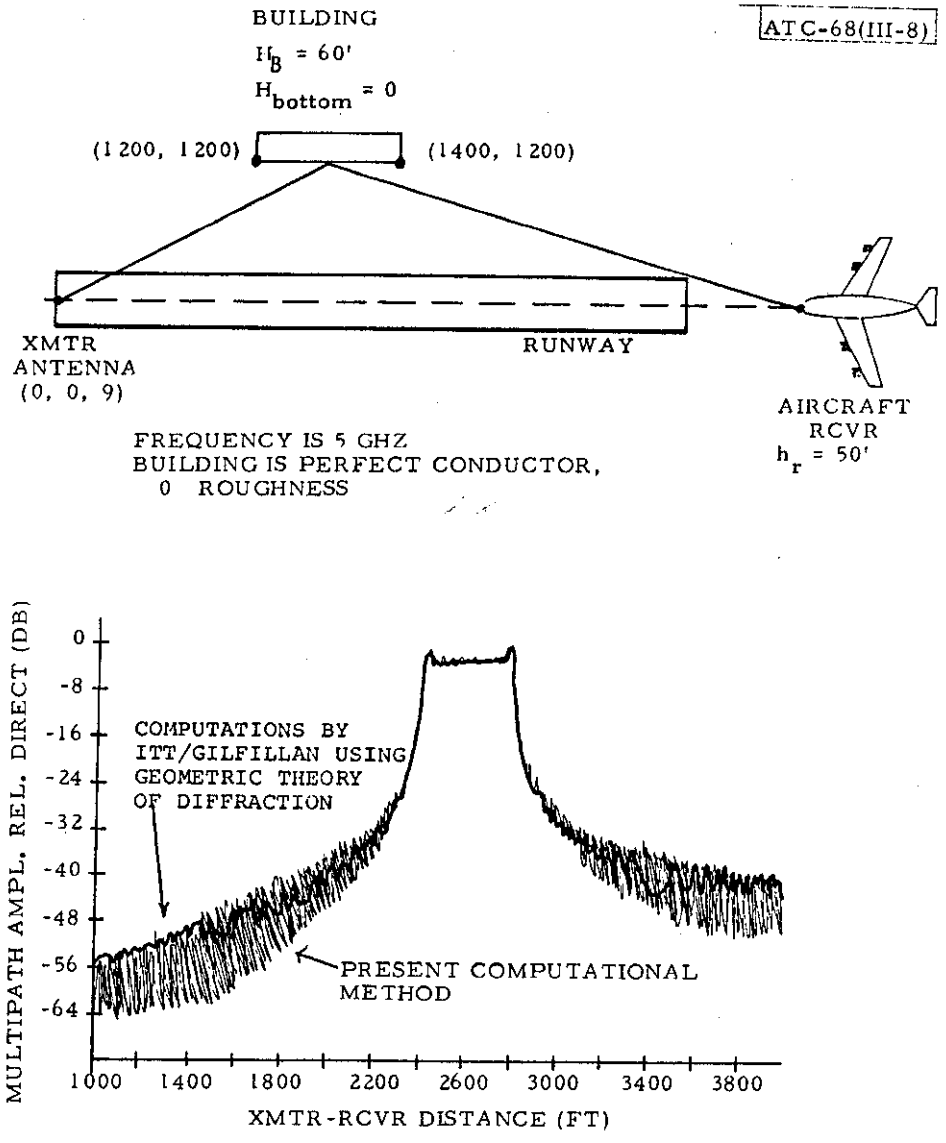

Fig. III-8. Comparison of results with those obtained using geometric theory of diffraction, for scattering from a large building.

along with the physical geometric arrangement of the building, transmitter, receiver, and the parameters used in the measurement. The corresponding result obtained using the computational procedures given in Section III A-D is also shown in Fig. III-8. This result applies, of course, to the X-O-R ray path which does not include any of the ground reflections between building and transmitter, or receiver, that were discussed in Section III D. The data for these latter ray paths are presented subsequently.

If we compare the results in Fig. III-8, it is seen that there is reasonably good agreement between the two sets of data. The peak magnitude of the reflection for both results is about -3 dB and occurs in a specular region of reflection that extends from 2400 to 2800 feet from the transmitter. The geometric diffraction theory data of Fig. III-8 show a decrease to about 55 dB and 42 dB at 1000 ft and 4000 ft , respectively, which is also true of the computational results. Thus, the two results are quite compatible. It is worthwhile to point out that the present computational procedure presented in Section III A-D is relatively simple and requires a small fraction of the computer time required by the method based on the geometric theory of diffraction. In fact, this latter method, as implemented by ITT/Gilfillan, would require such large amounts of computer time as to rule out its use in the present program for MLS simulation. In addition, as pointed out previously, the results of the present method are quite compatible with those based on geometric theory of diffraction.

The results obtained for the other three ray paths, X-G-O-R, X-O-G-R, X-G-O-G-R, discussed in Section II D, are presented in Fig. III-9. It is

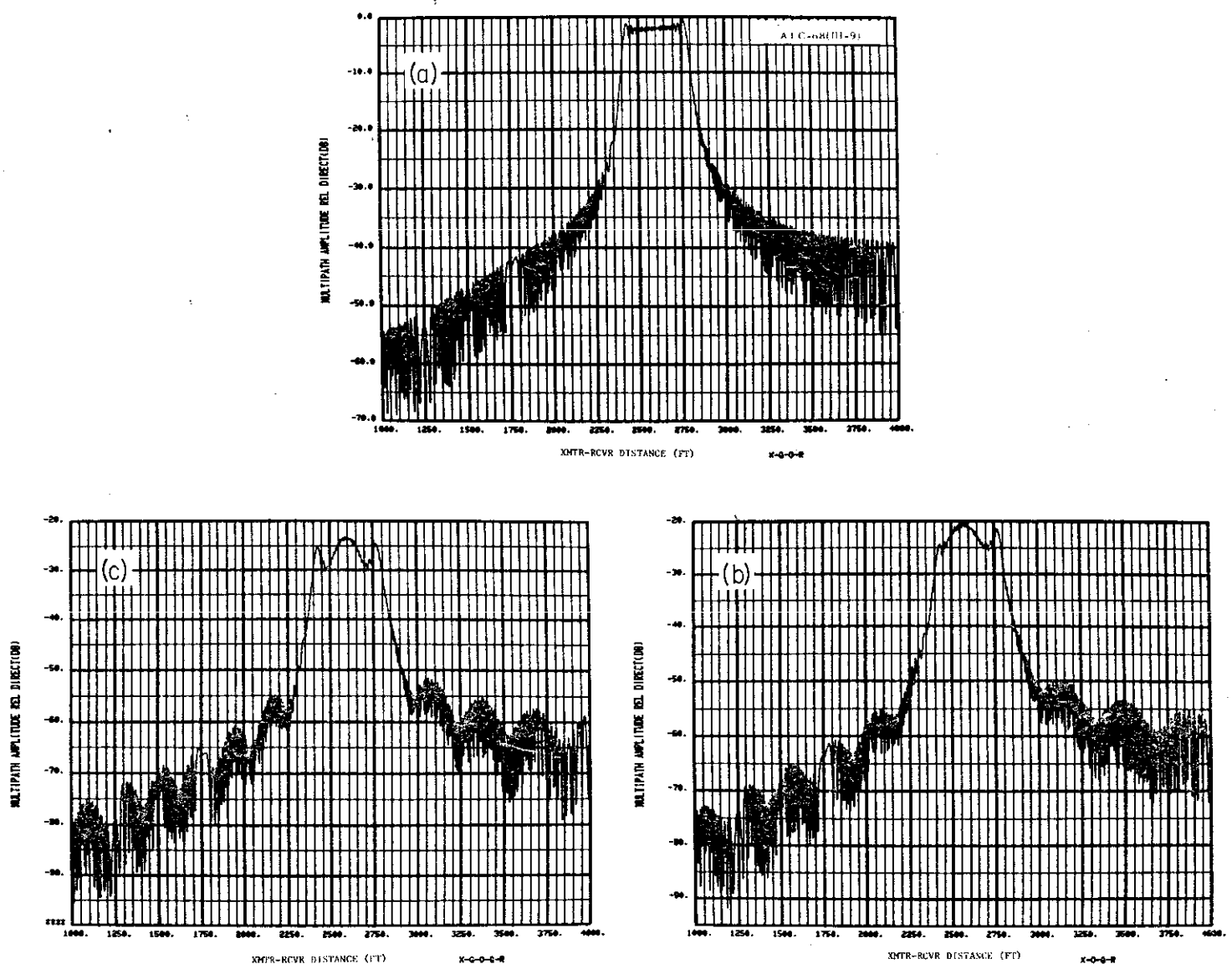

Fig. III-9. Results of computation of multipath amplitude, for geometry shown in Fig. III-8, by means of present method, for ray paths X-G-O-R, X-O-G-R, X-G-O-G-R.

interesting to note that the multipath amplitude levels depicted in Figs. III-9b,c are significantly lower than those given in Figs. III-8 and III-9a. The reason for this is that the position of the specular point, for the ray paths X-G-O-R, X-G-O-G-R, given in Figs. III-9b,c, does not lie on the building, so that small values for ρ_{Ba}, ρ_{Be}, are obtained when Eqs. (III-4) and (III-8) are employed, respectively.

We now point out that the results obtained using the computational procedures presented in Section III A-D have also been compared with experimental data for multipath amplitude levels measured at Logan airport, and at NAFEC. These experimental data were obtained at C-band, 1 GHz, for hangars and aircraft at Logan airport, and for the screen located at NAFEC. Reasonably good agreement was obtained between the results of the computer program and these experimental data.[12,13] For the sake of completeness, some of these comparisons with experimental data are now presented.

The Delta hangar depicted in Fig. III-10 is a simple faced building. The section to the left is metal clad and reflections from it can be compared quantitatively to the results obtained with the model. The transmitter and receiver were positioned as shown in Fig. III-11a, so that as the receiver antenna height was changed, referred to as a mast run, the specular point moved vertically along the face of this left-hand section. As the specular point moved across the lower edge of the large metal part at the top of the building, edge diffraction was observed. The results are compared to that of the model in Fig. III-11, and it is seen that there is good agreement.[13]

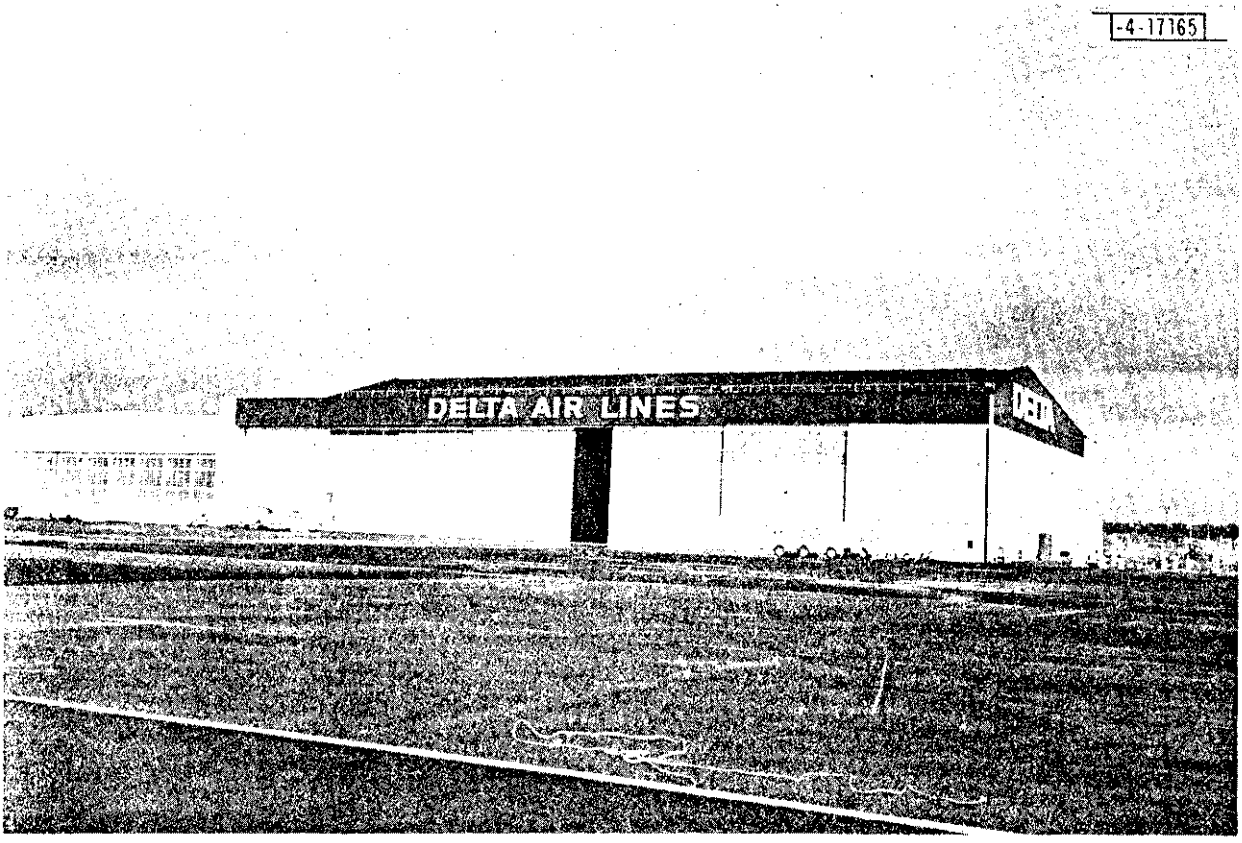

Fig. III-10. The Delta hangar located at Logan airport.

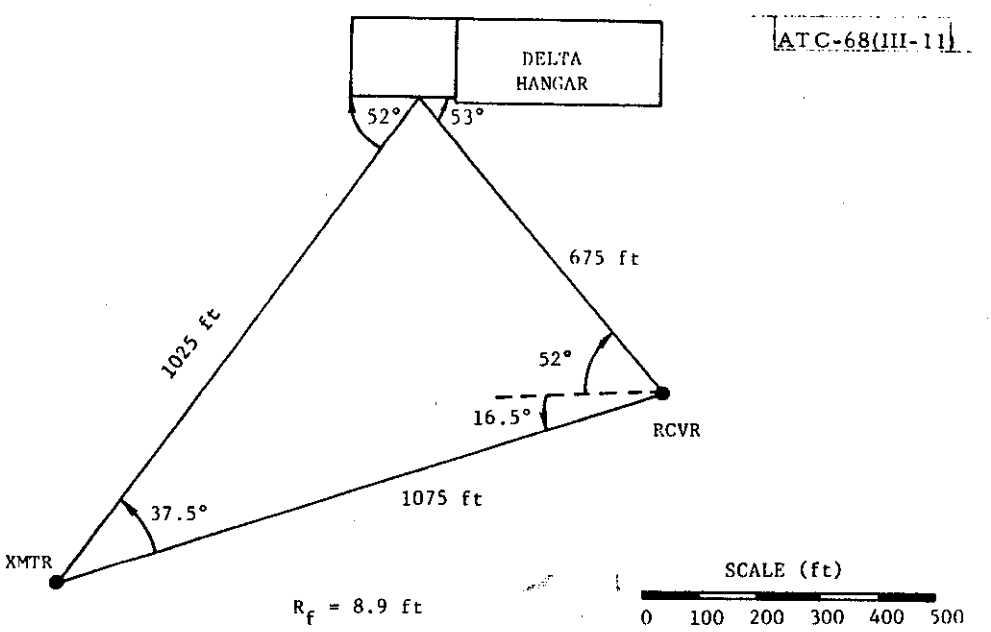

(a) GEOMETRY

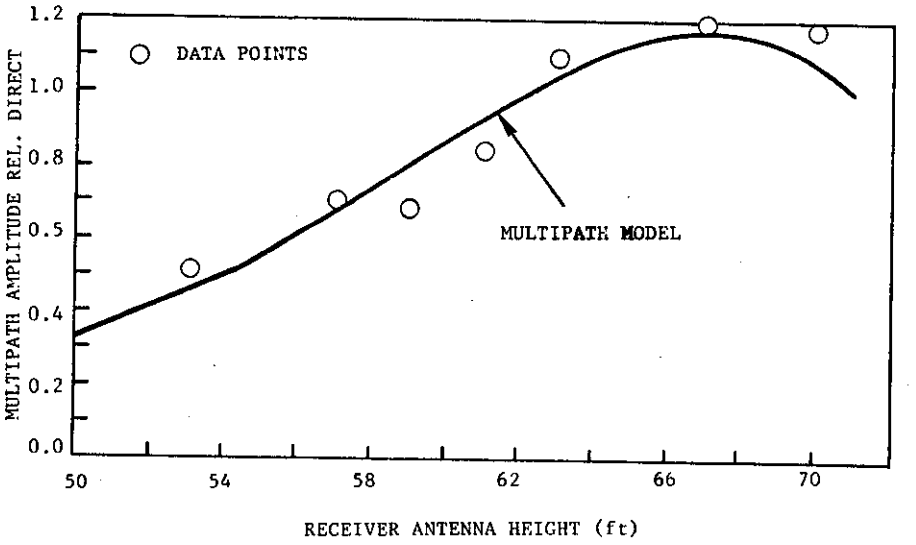

(b)

Fig. III-11. Comparison of computational results with experimental C-band measurements for the Delta hangar, and for 8 December 1974 data.

We now present some of the experimental data obtained by some of the Phase II MLS contractors for the screen located at NAFEC, which is depicted in Fig. III-12. An illustration of this is provided by the data for test 1, azimuth multipath at rollout, as shown in Fig. III-13a. The screen is oriented to produce maximum multipath at 5500 ft from the azimuth site. The multipath is out of beam by 30° in the azimuth plane and is, therefore, easily resolved from the direct signal by the directivity of the scanning function. Figures III-13b and III-13c indicate relative multipath amplitude levels obtained from computer simulation, and three contractors' data for the two required tests. The simulation concurs with the Bendix data from the original Phase II tests.[12] In the supplemental tests, the screen was apparently misaligned horizontally and vertically.

Similar behavior also occurred in test 2, azimuth multipath at threshold. The screen is oriented for a multipath maximum at 7500 ft from the azimuth transmitter, as shown in Fig. III-14a. The relative multipath amplitude levels for two horizontal cuts are illustrated in Fig. III-14b,c. The simulation, with parameters selected to fit the Bendix configuration, concurs with the original Bendix tests on the horizontal cuts.

ATC-68(III-12)

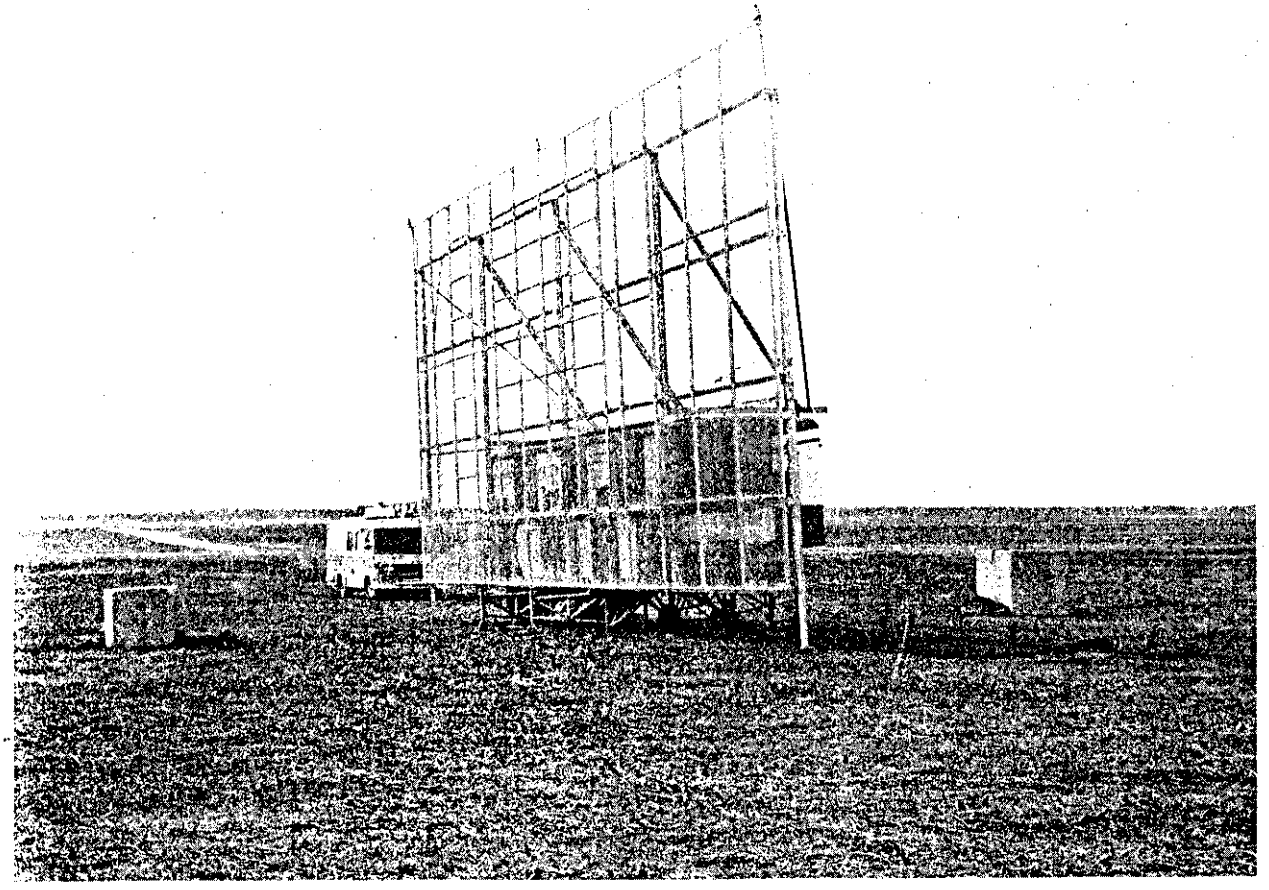

Fig. III-12. Screen at NAFEC used in MLS Phase II tests.

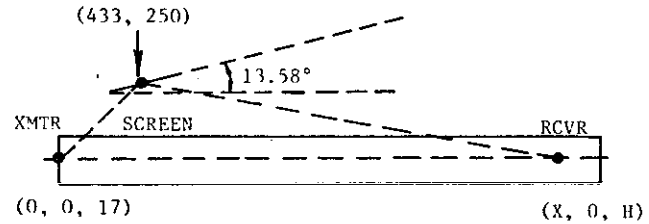

SCREEN REFLECTOR IS 52 FT LONG, 25 FT HIGH, 2 FT OFF GROUND

(a)

GEOMETRY FOR TEST 1

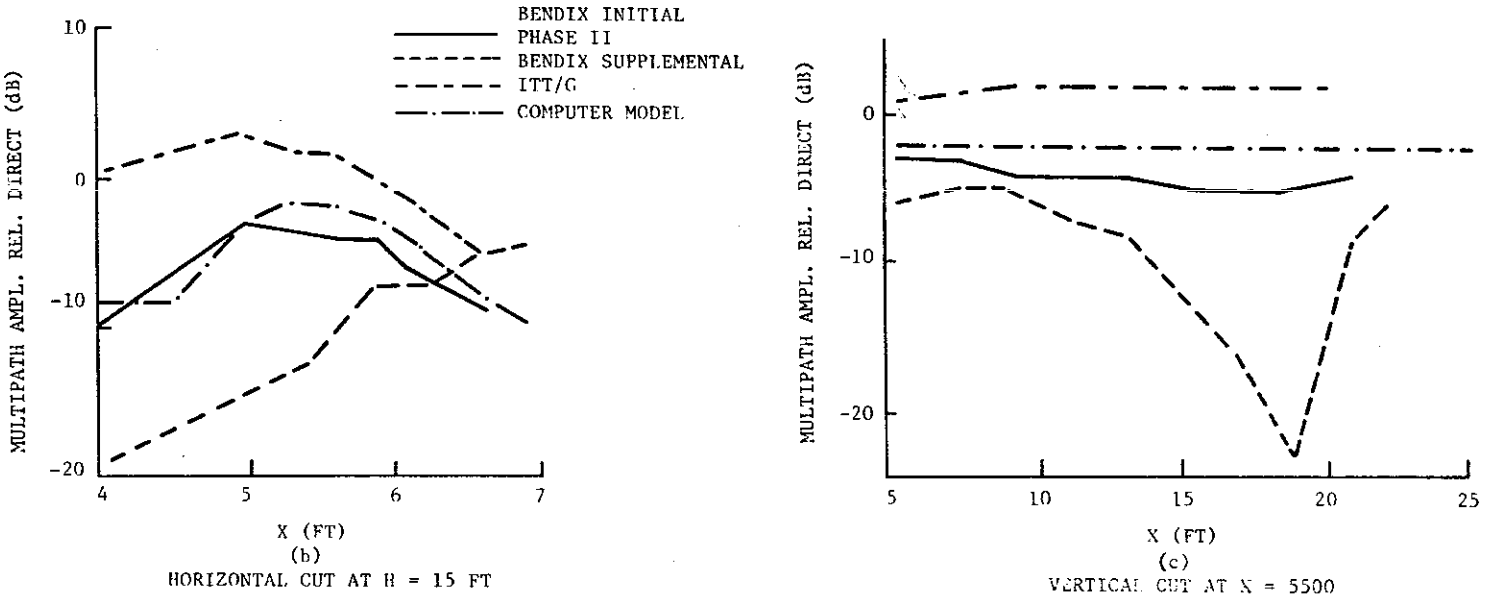

Fig. III-13. Comparison of computational results with experimental C-band measurements for the NAFEC screen, Test 1.

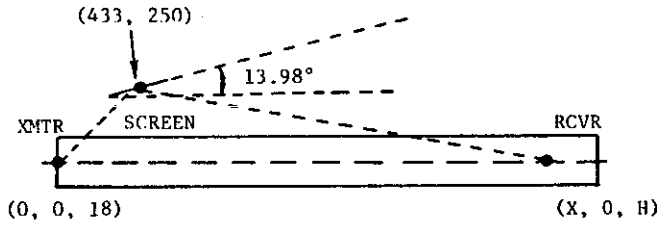

SCREEN REFLECTOR IS 52 FT LONG, 25 FT HIGH, 2 FT OFF GROUND

(a)
GEOMETRY FOR TEST 2

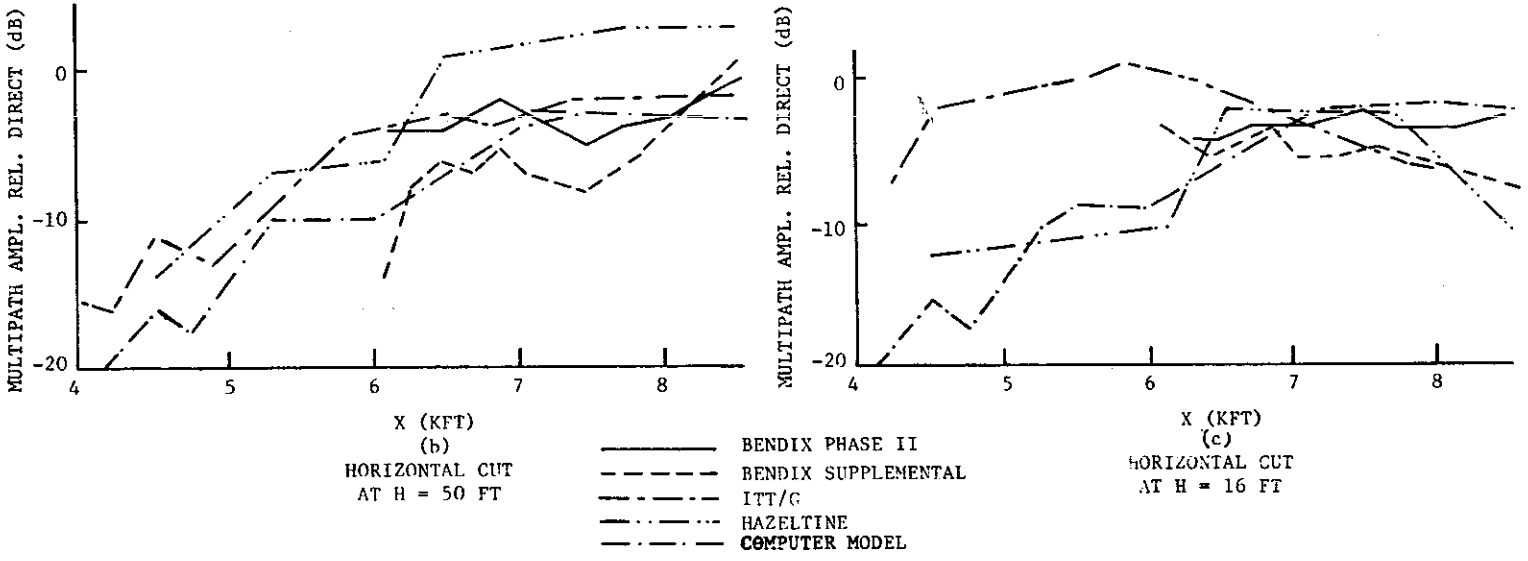

Fig. III-14. Comparison of computational results with experimental C-band measurements for the NAFEC screen, Test 2.

IV. SCATTERING FROM AIRCRAFT

A discussion is now presented of the computations that were used to obtain the multipath propagation components due to scattering from aircraft. The computations are similar to those given in Section III for scattering from buildings. This algorithm, described in Section IV C, is based on diffraction by a rectangular aperture and divergence of rays. This computational method has been checked by comparing its results with experimental field measurements, as well as geometric theory of diffraction,[8] and the data are presented in Section IV D.

It is assumed that only the fuselage, i.e., main body, and the tail fin are likely to produce significant multipath levels, due to scattering, for representative geometries. Moreover, we neglect shielding by the wings. This model is quite similar to the more elaborate model presented in Crispin and Siegel,[9] pp. 318-319. It might be observed that many secondary details, such as the front and rear of the fuselage, leading and trailing edges of wings, and engines, which are ignored in our model do not seem important insofar as significant MLS multipath levels are conerned. For example, the theoretical and experimental results for a Convair 990 model in Crispin and Siegel,[9] pp. 322-323, suggest that the multipath amplitude levels from these other surfaces are always at least 15 dB below that of the fuselage and tail fin. The fuselage and tail fin are treated independently in the subsequent analysis.

A. Circular Cylinder Model For Fuselage

As pointed out previously, it is assumed that the fuselage is likely to

produce significant multipath levels due to scattering from aircraft. The specific model assumed for the fuselage is that it can be considered as a horizontal circular cylinder of length ℓ_F and diameter D_F whose center is at a height of h_F above the ground, as shown in Fig. IV-1. In addition, it is assumed that the fuselage can be modeled as a smooth perfect conductor.

The actual fuselage length entered in the computer table, or memory, is ℓ_F' and is typically the length that would be obtained from an engineering drawing for the aircraft. However, the fuselage length used in the subsequent computations is $\ell_F = \ell_F' - \ell_T$, where ℓ_T is the length of the tail fin, cf. Fig. IV-1. This fuselage length extends from the front edge of the tail fin to the cockpit end of the aircraft. This procedure was found to be desirable in order to provide agreement between the results of the computation and multipath field measurements taken at Logan airport.[13]

It is assumed that the transmitter and receiver are on the same side of the fuselage in order to observe scattering from the fuselage at the receiver. If this is not true, then the fuselage is not oriented for scattering and the multipath signal amplitude is set to zero. These assumptions are discussed in greater detail in Appendix G.

B. Circular Cylinder Model For Tail Fin

It has been mentioned previously that the tail fin is likely to produce significant multipath levels due to scattering from aircraft. The tail fin is modeled as two sections of a vertical circular cylinder of height H_T and radius R_{tail}, as shown in Fig. IV-2. In addition, it is assumed that the tail

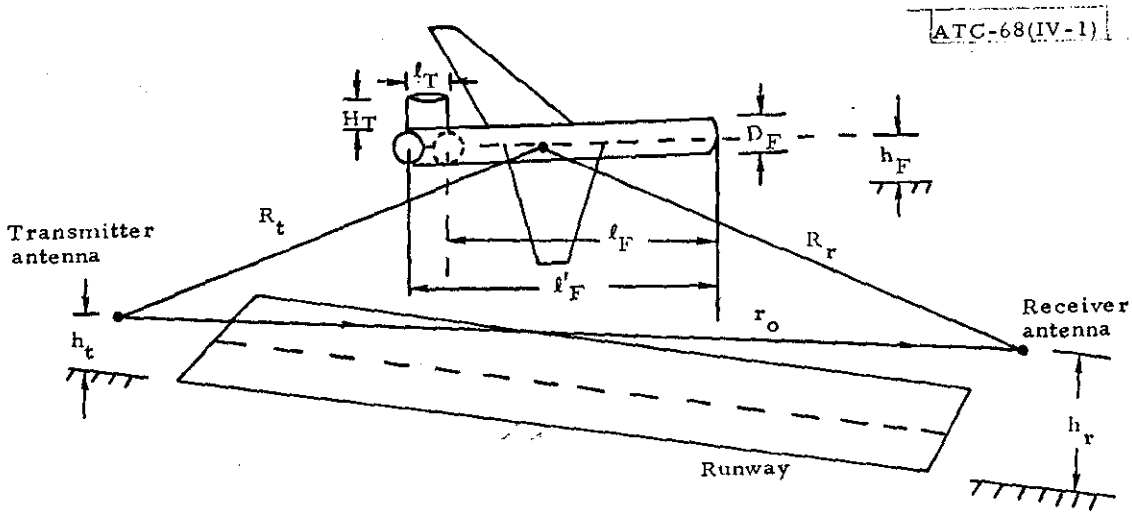

ℓ'_F = fuselage length entered in computer table

ℓ_F ($= \ell'_F - \ell_T$) = fuselage length used in computations

Fig. IV-1. Model used to determine multipath parameters due to scattering from aircraft.

fin can be modeled as a smooth perfect conductor. This assumption is similar to that presented previously in Section IV A for the fuselage.

The transmitter and receiver are assumed to be on the same side of the tail fin in order to observe scattering from the tail fin at the receiver. If this is not true, then the tail fin is not oriented for scattering and the receiver signal is set to zero. These assumptions are discussed in detail in Appendix G.

C. Method Based On Diffraction By Rectangular Aperture And Divergence Of Rays

The amplitude and phase of the multipath components due to scattering from aircraft are computed by employing the method of images and Babinet's principle, cf. Sommerfeld,[5] p. 204 and Silver,[7] p. 167, so that we may consider the equivalent problem of diffraction by a rectangular opening in an opaque screen. This procedure is similar to that described previously in Section III for the corresponding problem involving buildings. However, in the present case, when dealing with aircraft, a correction factor[14] is applied to take into account the divergence of rays from the cylindrical surfaces used to model the fuselage and tail fin.

The complex reflection coefficient of the multipath component due to scattering from aircraft is computed in a manner similar to that for buildings given in Eq. (III-1), as

$$\rho_A = \rho_{Aa}\rho_{Ae}\rho_R\rho_t R_{eq} \quad , \qquad \text{(IV-1)}$$

where ρ_t and ρ_R were given in Eqs. (III-2) and (III-3), respectively, and R_{eq} is computed similar to the manner indicated in Eqs. (II-10) and (II-11). In computing R_{eq}, it is assumed that the depolarization loss is due to reflection from a tilted planar facet which is tangent to the cylinder at the specular point. The quantities ρ_{Aa}, ρ_{Ae} are the azimuthal and elevation factors, respectively, and are computed differently for the fuselage and the tail fin. The computation of these quantities depends on the determination of the specular point, so that the details for computing the position of this specular point for reflection from a cylinder are given in Appendix G and apply to both fuselage and tail fin computations.

We first consider the case of the fuselage, so that the factor ρ_{Aa} corresponds to the azimuthal factor for a building, i.e., the geometry of Fig. IV-3 is applicable with ℓ_F playing the role of W_B, which was defined previously as the width of the building. Thus the computation of ρ_{Aa} is done in a manner similar to that for ρ_{Ba} given previously in Eqs. (III-8) - (III-10).

The factor ρ_{Ae} accounts for the divergence due to the curved surface of the fuselage. Since the factor ρ_{Aa} accounts for the finite length of the fuselage, ρ_{Ae} is computed as if the fuselage were an infinite cylinder. For purposes of discussion, we will use a coordinate system whose x'-axis coincides with that of the fuselage center, with the y'-axis located above, or below, the specular point as illustrated in Fig. IV-3. We can use the divergence formula, Eq. (22), p. 69, given by Riblet and Barker[14] to obtain

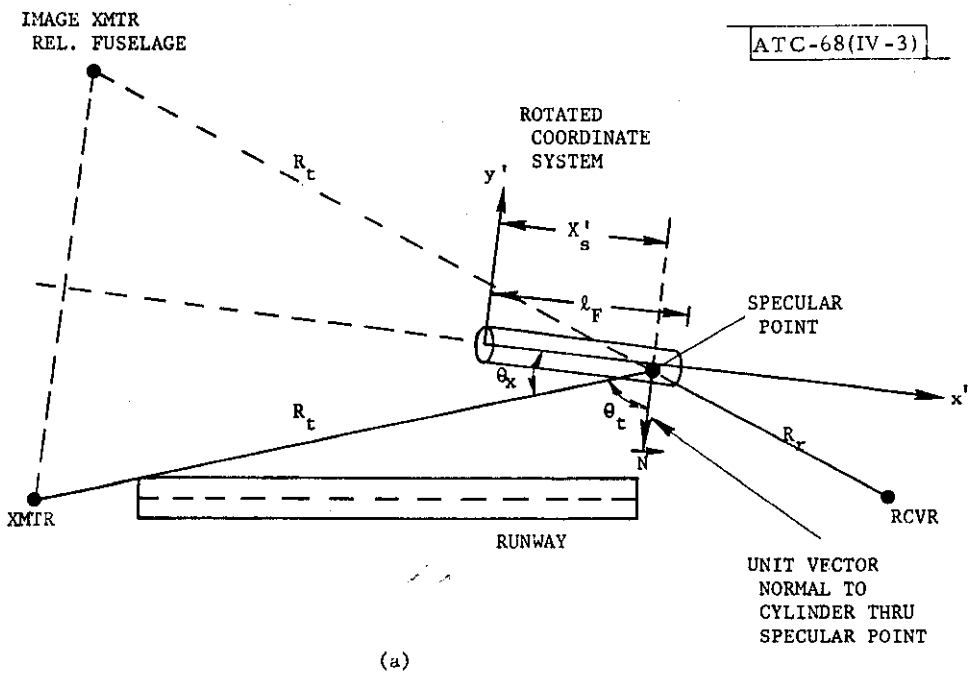

(a)

TOP VIEW

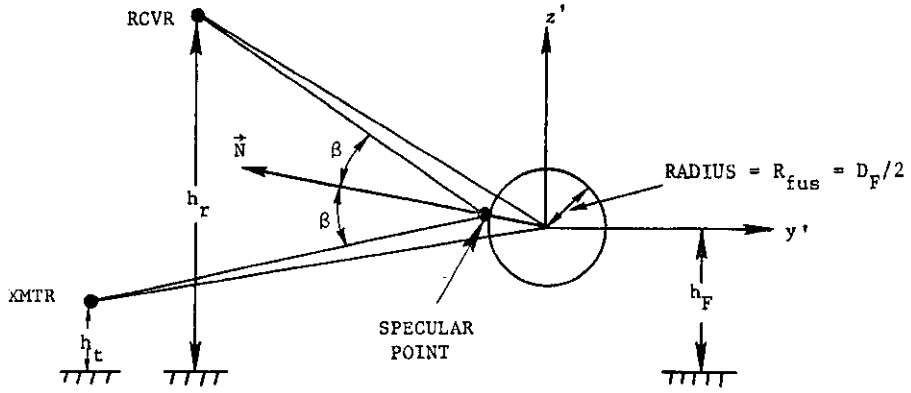

(b)

SIDE VIEW

Fig. IV-3. Side and top views of fuselage scattering geometry.

$$\rho_{Ae} = \left[1 + \frac{2R_o \sin^2\theta_x}{R_{fus} \cos \theta_t}\right]^{-1/2} , \qquad \text{(IV-2)}$$

where $R_o = \frac{R_t R_r}{R_t + R_r}$, R_{fus} is the radius of the cylinder, or fuselage, and the angles θ_t, θ_x are the angles between the incident vector $\vec{R}_t$ and the normal to the cylinder, and between $\vec{R}_t$ and the axis of the cylinder, respectively, as shown in Fig. IV-3.

If the specular point does not lie on the fuselage, then it is repositioned as follows. If $X'_s < 0$, then X'_s is set equal to zero, while if $X'_s > \ell_F$, then X'_s is set equal to ℓ_F, cf. Fig. IV-3. The justification for repositioning the specular point in this way is based on the geometric theory of diffraction.[8]

We now consider scattering from the tail fin of an aircraft. Once again, it is assumed that the tail fin is a perfect conductor whose multipath-to-direct signal amplitude ratio is given by Eq. (IV-1). The factor ρ_{Ae} for the tail fin corresponds to the elevation factor for a building, i.e., the geometry of Fig. III-1 should be compared to that of Fig. IV-2a, so that we have the correspondence $h_b = H_{bottom}$, $H_t = H_B$. The appropriate expressions to employ for computing ρ_{Be} are given by Eq. (III-4) - (III-6).

The computation of the azimuthal factor, ρ_{Aa}, is complicated by the fact that the tail fin has been modeled as only a section of a cylinder, so that it does not scatter energy over a wide range of angles. We have assumed the following conditions in performing the computations:

(1) The multipath signal is zero if the specular point lies outside the tail fin in azimuth, i.e., outside the angular limits defined by the angle θ_{tail} in Fig. IV-2b.

(2) The multipath signal can be predicted by the general divergence formula for a full cylinder if the specular point lies within the tail fin in azimuth.

It should be noted that condition (1) implies that energy scattered from the tail fin will be observable, i.e., non-zero, over an angular sector of approximately $2\theta_{tail}$ radians in extent. If the transmitter-tail fin-receiver orientation does satisfy condition (1), then we can use the divergence formula, Eq. (22), p. 69, given by Riblet and Barker[14] to obtain

$$\rho_{Aa} = \left[1 + \frac{2R_o \sin^2\theta_x}{R_{tail} \cos \theta_t}\right]^{-1/2} , \qquad \text{(IV-3)}$$

where R_o was defined previously as $\frac{R_t R_r}{R_t + R_r}$, R_{tail} is the radius of the cylinder, or tail fin, and the angles θ_t, θ_x are defined in a manner similar to that for the fuselage scattering problem, cf. Eq. (IV-2), and are shown in Fig. IV-4.

If the specular point does not lie on the tail fin, then it is repositioned as follows. If $Z'_s < h_b$, then Z'_s is set equal to h_b, and if $Z'_s > h_b + H_t$, then Z'_s is set equal to $h_b + H_t$. The justification for repositioning the specular point in this manner is, once again, based on the geometric theory of diffraction.[8]

It should also be noted that the ground reflection multipath components

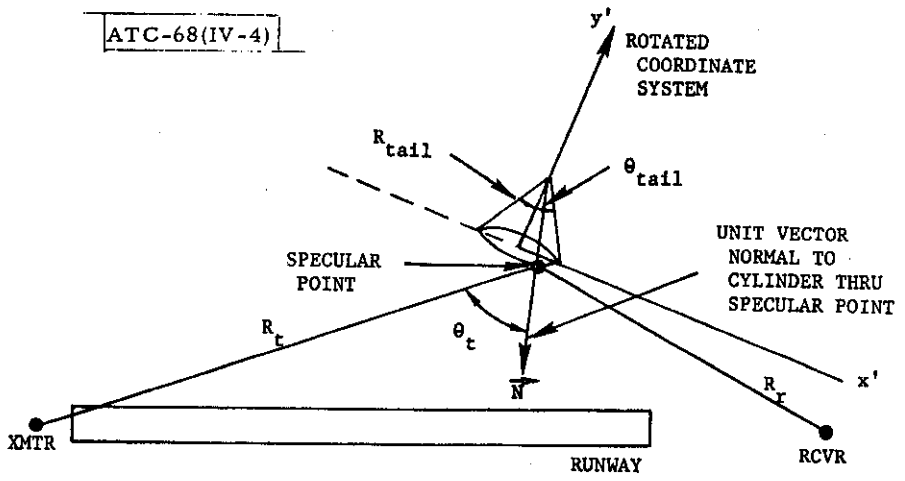

(a)
TOP VIEW

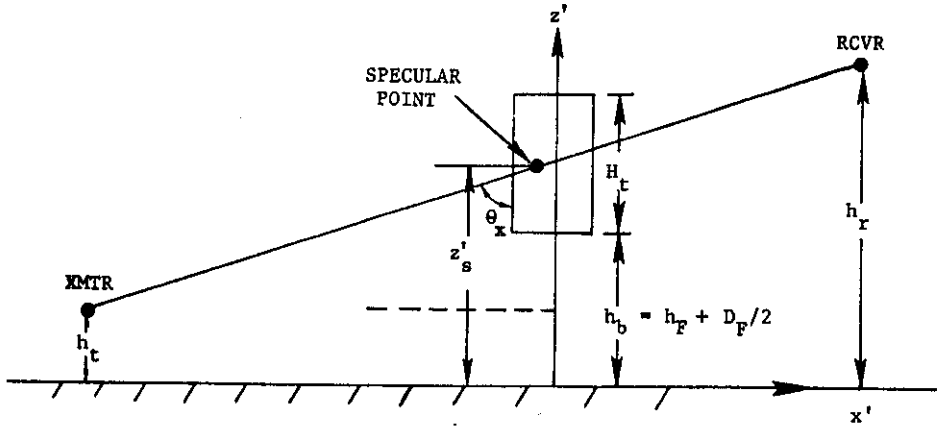

(b)
SIDE VIEW

Fig. IV-4. Side and top views of tail fin scattering geometry.

are computed for the fuselage and tail fin in a manner similar to that for buildings given in Section III D. Thus, there is a total of eight multipath components for each aircraft, four are associated with scattering from the fuselage, and the other four are due to the tail fin. In addition, we mention that the justification for removing the transmitter antenna pattern from inside the Fresnel integrals, for the aircraft scattering problem, is similar to that given previously in Section III B for the case of scattering from buildings.

D. Computation Of Multipath Parameters

The amplitude and phase of the multipath component due to scattering from either the fuselage or tail fin are given by

$$V_A = |\rho_A| \quad , \tag{IV-4}$$

$$\psi_A = \text{ARG}\{\rho_{Aa}\rho_{Ae}\, R_{eq}\} + k(R'_t + R'_r - R_t - R_r) \quad , \tag{IV-5}$$

where R'_t, R'_r are the distances from the repositioned specular point to the transmitter, receiver, respectively. If the specular point is not repositioned, then we have, of course, $R'_t = R_t$, $R'_r = R_r$. The computations required for the planar directional angles, fractional Doppler frequency and relative time delay are similar to those for the specular ground reflection given previously in Eqs. (II-23) - (II-28). However, it should be noted that these parameters are computed using the repositioned specular point. If there is no repositioning, then, of course, the original specular point is used to derive these parameters. The additional considerations required for the X-G-O-R, X-O-G-R,

X-G-O-G-R ray paths are similar to those used in the computations for scattering from buildings, discussed in detail in Section III D.

E. Comparison of Results With Experiments And Geometric Diffraction Theory

We now present some computer validation data for the computational procedures presented in Sections IV A-D. An indication of the operation of this computer program can be obtained from the flow chart depicted in Fig. IV-5. In order to present the computer validation results we employ some data due to ITT/Gilfillan[11] for reflections from a DC-10 fuselage. The ITT/Gilfillan computations used the geometric theory of diffraction.[8] These data are shown in Fig. IV-6 along with the physical geometric arrangement of the aircraft fuselage, transmitter and receiver, and the parameters used in the measurement. The corresponding data gotten by using the computational procedures given in Sections IV A-D are depicted in Fig. IV-6. This result applies to the X-O-R path, for which the ray path does not include any of the ground reflections between aircraft and transmitter, or receiver, that were discussed in Section IIID. The results for these latter ray paths are presented subsequently.

If we compare the data in Fig. IV-6, we see that there is good agreement between the two sets of results. The magnitude of the reflection for both results is about -20 to -30 dB in a specular region of reflection that extends from about 60 to 260 feet from the transmitter. The geometric diffraction theory data of Fig. IV-6 show a decrease to 40 dB at 40 and 280 feet, which is also true of the computational results presented in Fig. IV-6. Thus, the two sets of data are quite compatible. The data obtained for the other

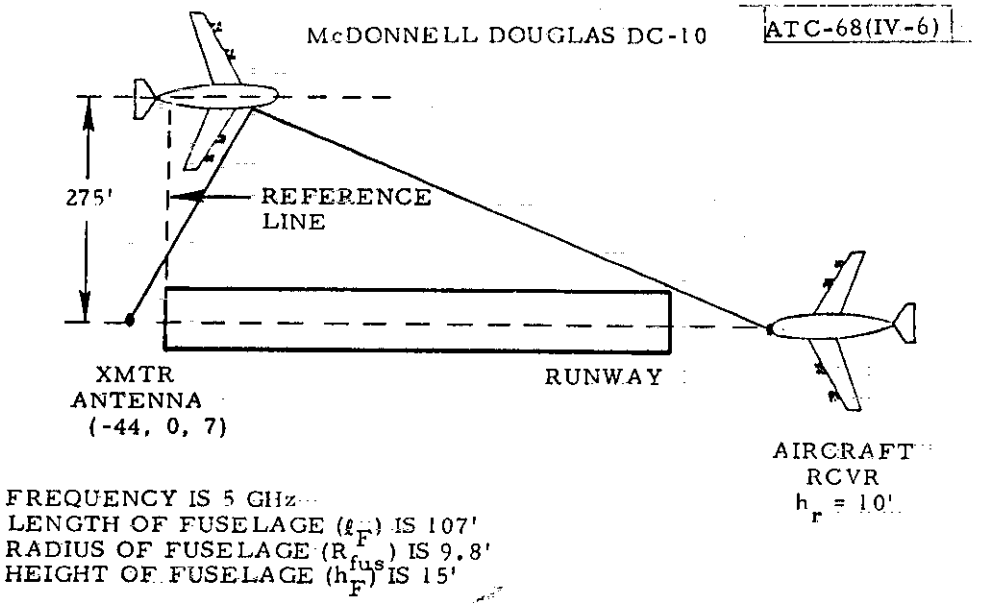

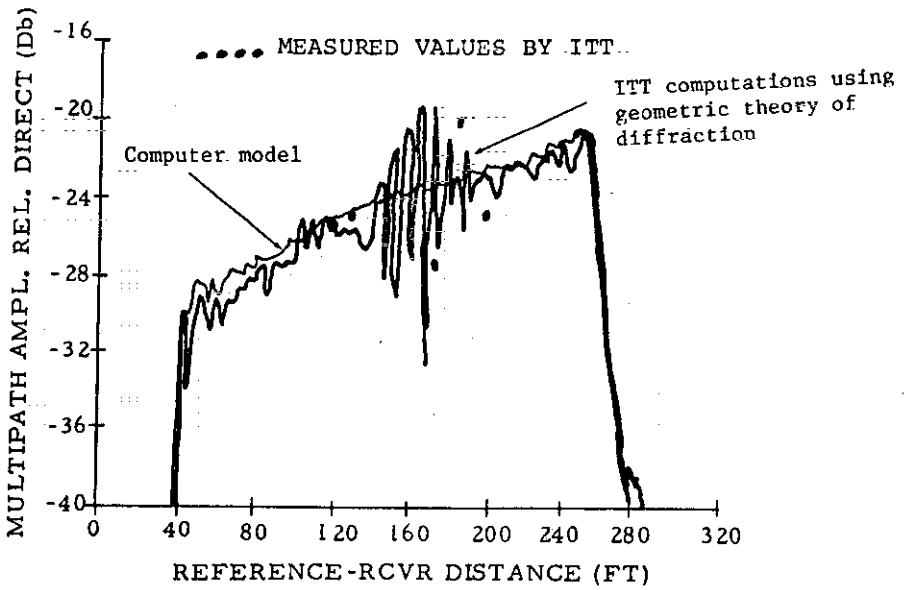

Fig. IV-6. Comparison of results with those obtained using geometric theory of diffraction, and with field measurement data, for scattering from aircraft fuselage.

three ray paths, X-G-O-R, X-O-G-R, X-G-O-G-R, discussed in Section III D, are presented in Fig. IV-7. It should be noted that directive antennas were used by ITT/Gilfillan, at the transmitter and receiver, so that the multipath amplitude levels, for the ray paths given in Fig. IV-7 would have a minimal effect on those observed in Fig. IV-6.

We now point out that the results obtained using the computational procedures presented in Section IV have also been compared with experimental data for multipath amplitude levels measured at Logan airport. These experimental data were obtained at C-band for various aircraft, such as the Boeing 747, shown in Fig. IV-8, in a series of measurements which were supervised by Lincoln Laboratory. Reasonably good agreement was also obtained between the results of the computer program and these experimental data.[13] We now present some of these measurements for relative multipath amplitude levels observed due to scattering from the tail fin of a B747 at Logan airport. These measurements will serve as validation data for the computational model, for scattering from a tail fin, discussed in Section IV C.

Figure IV-9a illustrates the geometry of the transmitter and receiver relative to the Boeing 747 shown in Fig. IV-8. Note that the angle of the incoming ray, referenced to the centerline of the plane, is 20° while that of the outgoing ray is 35°. The curvature of the tail is responsible for this result. A receiver mast run was performed and the measured levels are superimposed on top of the model results, for the ray path X-O-R, in Fig. IV-9b. We see that the data follow the overall shape of the model curve as well as agreeing in level. Similar measurements and results were also obtained for DC-10 and B 727 aircraft.

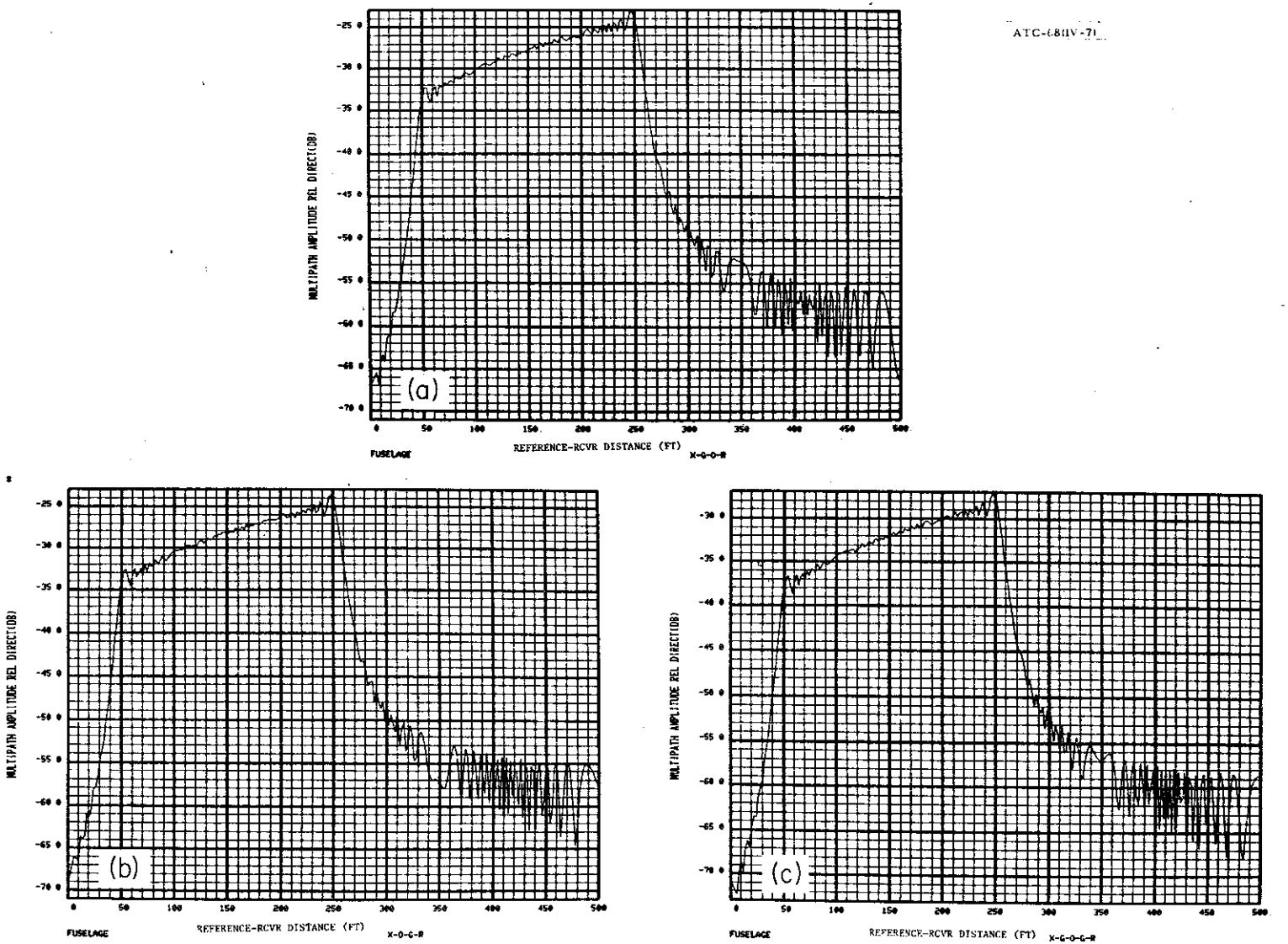

Fig. IV-7. Results of computation of multipath amplitude, for geometry shown in Fig. IV-6, by means of present method, for ray paths X-G-O-R, X-O-G-R, X-G-O-G-R.

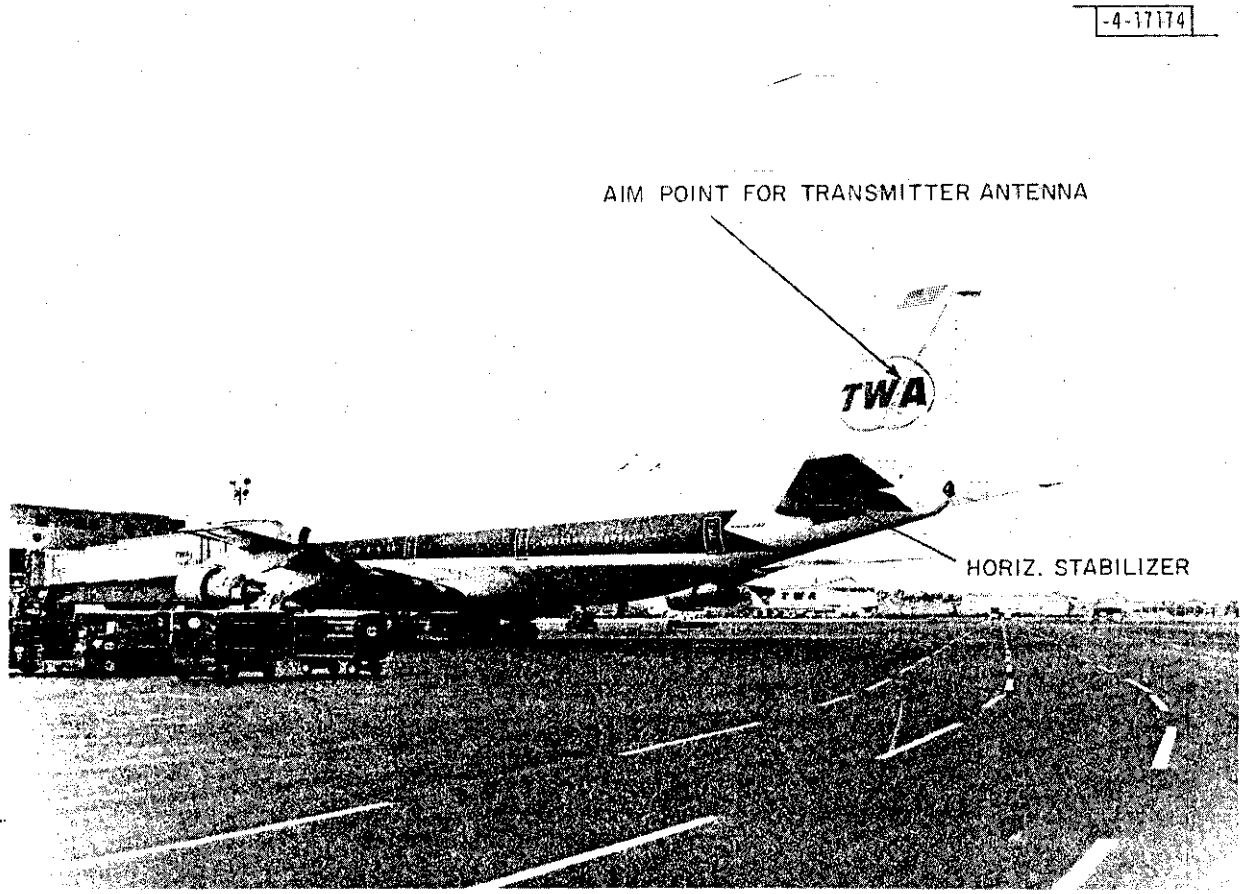

Fig. IV-8. Boeing 747 airplane used in tail fin multipath measurements at Logan airport.

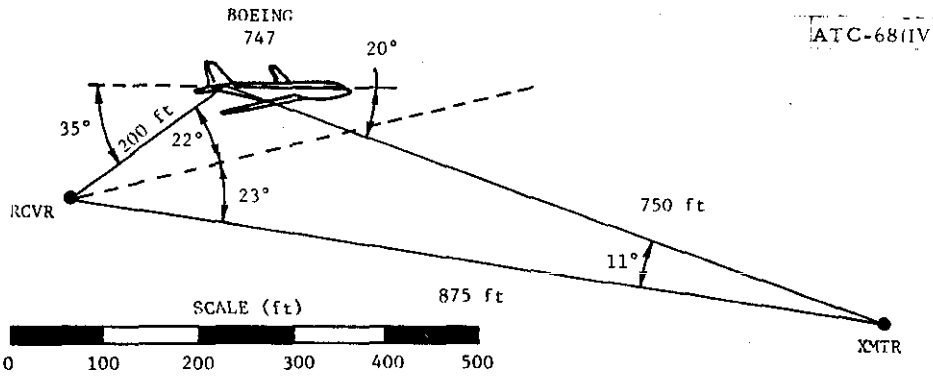

(a) Geometry for 12 December 1974 Boeing 747 mast run.

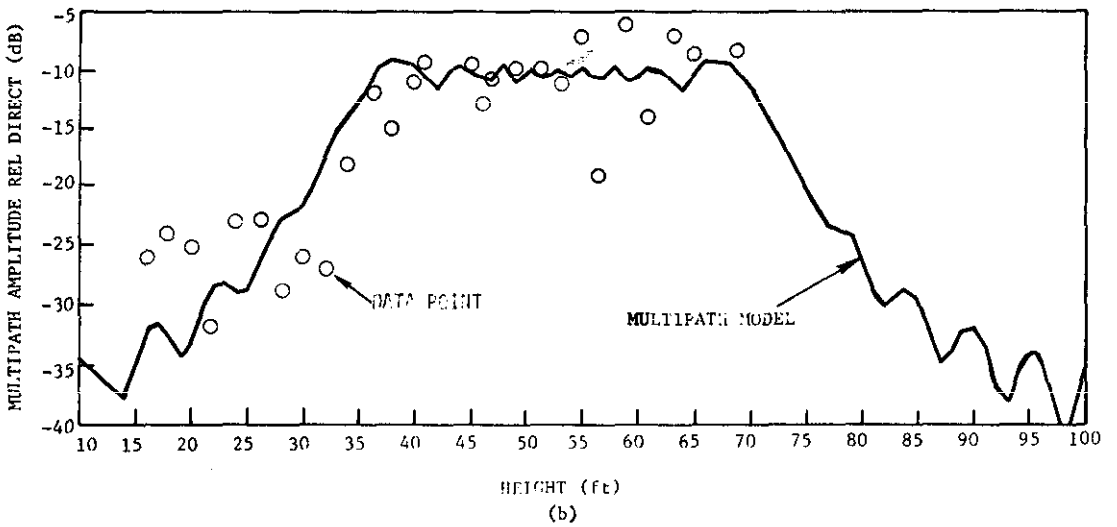

(b)

Fig. IV-9. Comparison of computational results with experimental C-band measurements for the B747 tail fin at Logan airport, and for 12 December 1974 data.

V. DIFFUSE SCATTERING FROM GROUND

A. Method Based on Very Rough Surface Model

A presentation is now given of the computations which were used to obtain the multipath propagation components due to diffuse scattering from the ground. These diffusely scattered waves arrive at the aircraft receiver antenna from a wide range of angles in both azimuth and elevation, due to radiation from a large surface area on the ground known as the glistening surface, cf. Ref. 3 , p. 356. In addition, the phase angles and amplitudes of these diffusely scattered waves cannot be predicted, from a practical computational point of view, for any rough surface which is a sample function from the ensemble of such rough surfaces. It is only possible to obtain average functionals for these values, where, as usual, the averages are taken with respect to the ensemble of rough surfaces.

Once again, as was done in Section II, the ground is assumed to be modeled as a rough surface with a Gaussian height distribution, with root-mean-square roughness height, σ_h, and a Gaussian correlation coefficient with correlation length, σ_ℓ. The parameter, σ_h, may, or may not, be the same as the corresponding parameter introduced in Section II. In order to obtain tractable computations, it is assumed that the surface is very rough, and that it is perfectly conducting. In this case, we may use the theory developed by Kodis,[15] and Barrick,[16] and used by McGarty,[17] in assessing the performance of the Discrete Address Beacon System (DABS). The following assumptions are required in the analysis:

(1) The radius of curvature everywhere on the scattering surface must be much greater than the wavelength of the incident radiation.

(2) Multiple scattering effects can be neglected.

(3) The root-mean-square surface height is much greater than the wavelength.

The condition given in assumption (3) implies that the surface is very rough.

The geometry assumed for diffuse scattering is shown in Fig. V-1. The mean-square value of the scattered field at the receiver, relative to the directly transmitted field, is

$$\frac{\langle |E_S|^2 \rangle}{|E_o|^2} = \frac{1}{4\pi} \int\int_{\substack{\text{ground} \\ \text{surface}}} \left(\frac{r_o}{R_t R_r} \right)^2 \sigma \, ds \quad , \tag{V-1}$$

where σ is the bistatic radar cross section for the rough surface. It has been shown by Barrick[16] that

$$\sigma(\theta_S, \phi_S, \phi_i) = \frac{\sec^4 \gamma}{S^2} \exp\left[- \frac{\tan^2 \gamma}{S^2} \right] |R(\xi)|^2 \quad , \tag{V-2}$$

where θ_S, ϕ_S are the scattering angles, ϕ_i is the incidence angle, all depicted in Fig. V-1, and

$$\tan \gamma = \frac{(\sin^2\phi_i - 2 \sin\phi_i \sin\phi_S \cos\theta_S + \sin^2\phi_S)^{1/2}}{\cos\phi_i + \cos\phi_S} \quad , \tag{V-3}$$

$$S = 2 \sigma_h / \sigma_\ell \quad , \tag{V-4}$$

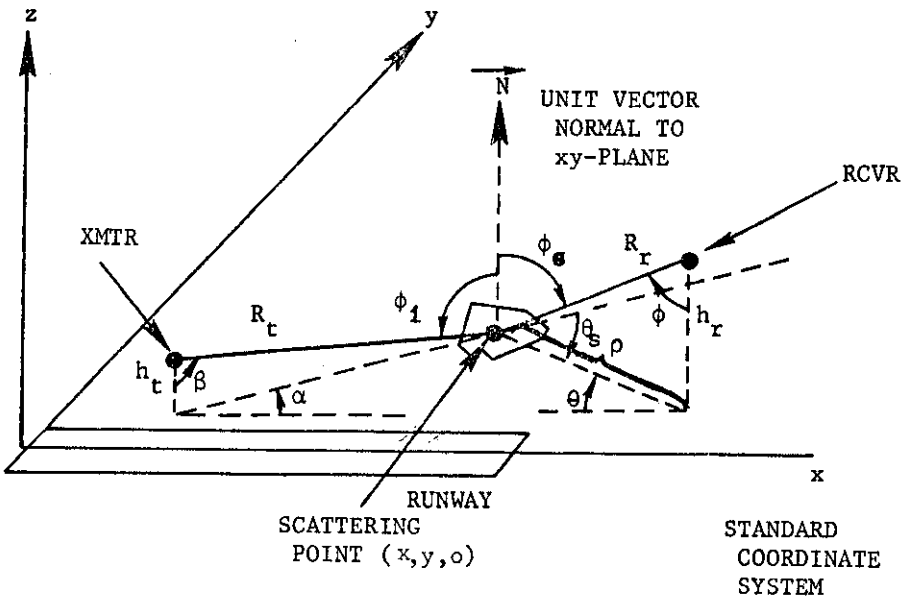

$$\phi_i = \beta$$
$$\phi_s = \phi$$
$$\theta_s = \theta + \alpha$$
$$\rho = h_r \tan\phi$$

Fig. V-1. Geometry for diffuse scattering from ground.

$$R(\xi) = \frac{-\sin\phi_i \sin\phi_S \sin^2\theta_S + a_2 a_3}{4 \sin^2\xi \cos^2\xi} \quad , \tag{V-5}$$

$$a_2 = \cos\phi_i \sin\phi_S + \sin\phi_i \cos\phi_S \cos\theta_S \quad , \tag{V-6}$$

$$a_3 = \sin\phi_i \cos\phi_S + \cos\phi_i \sin\phi_S \cos\theta_S \quad , \tag{V-7}$$

$$\cos\xi = \sqrt{\frac{1}{2}} \sqrt{(1 - \sin\phi_i \sin\phi_S \cos\theta_S + \cos\phi_i \cos\phi_S)} \quad . \tag{V-8}$$

We now define the channel spread function, $K(\theta,\phi)$, as the power per square radian incident at the receiver, relative to the directly transmitted power, coming from directions θ in azimuth and ϕ in elevation, cf. Fig. V-1. This function may be obtained from Eq. (V-1) as

$$K(\theta,\phi) = \frac{1}{\Delta\theta\Delta\phi} \frac{< |E_S|^2 >}{|E_o|^2}$$

$$= \frac{1}{4\pi\Delta\theta\Delta\phi} \iint_S \left(\frac{r_o}{R_t R_r}\right)^2 \sigma \, dxdy \quad , \tag{V-9}$$

where S is the incremental area defined in the xy-plane by the increments $\Delta\theta$, $\Delta\phi$. It is straightforward to evaluate $K(\theta,\phi)$ from Eqs. (V-2) and (V-9) by noting that $dxdy = \rho d\rho d\theta$, $\rho = h_r \tan\phi$, $\frac{d\rho}{d\phi} = h_r \sec^2\phi = R_r^2(\theta,\phi)$, so that

$$K(\theta,\phi) = \frac{r_o^2}{4\pi} \frac{\sigma(\theta + \alpha(\theta,\phi), \phi; \beta(\theta,\phi))\tan\phi}{R_t^2(\theta,\phi)} \quad , \tag{V-10}$$

where it has been assumed that $\Delta\theta$, $\Delta\phi \to 0$, and where the dependence of the various quantities in Eq. (V-10) on θ,ϕ has been taken into account and use has been made of the fact that $\theta_s = \theta + \alpha$, $\phi_s = \phi$, $\phi_i = \beta$, cf. Fig. V-1. In theory, $\Delta\theta,\Delta\phi$ would be chosen so that the incremental area $\Delta x\ \Delta y$ defined in the xy-plane is, say, $\sigma_\ell \times \sigma_\ell$ in area. However, in general, this would lead to a prohibitively large number of grid cells defined in the xy-plane, unless some effort is made to limit the range of the angles θ and ϕ. One method for doing this is to limit the grid cells to lie within the glistening surface, as defined by Beckmann and Spizzichino,[3] pp. 255-266. An alternative simpler method is used in which the channel spread function, $K(\theta,\phi)$, given in Eq. (V-10) is examined for various values of θ,ϕ to determine the range of angles in which $K(\theta,\phi)$ is significant, i.e., within 10 dB of its maximum value. This range of values for θ,ϕ is then retained to determine the grid mesh defined in the xy-plane. If the total number of grid cells defined in this manner is still too large, greater than 25, then the incremental area is taken as a square whose side is as large as, say, $3\sigma_\ell$. In the event that the number of grid cells is still too large, the range of θ,ϕ is limited further, so that $K(\theta,\phi)$ is within 5 dB of its peak value. This procedure produces a computationally feasible method for obtaining the diffusely scattered component from the ground.

The relative magnitude of the scattered wave coming from the direction θ to $\theta + \Delta\theta$, in azimuth, and ϕ to $\phi + \Delta\phi$, in elevation, is

$$V_D(\theta,\phi) = K^{1/2}(\theta,\phi) \cdot (\Delta\theta\Delta\phi)^{1/2} , \qquad \text{(V-11)}$$

where the relative phase shift, $\psi_D(\theta,\phi)$, is randomly selected from the interval $(-\pi,\pi)$ for each different pair of angles (θ,ϕ). The planar directional angles, fractional Doppler frequency, and time delay for each multipath component is computed in a manner similar to that given in Section II, Eqs. (II-23 through (II-28).

It is necessary to be aware of how the phase angle $\psi_D(\theta,\phi)$ changes as the receiver moves to a new position. In order to do this, the following procedure is used. We consider the phase angle $\psi_D(\theta_i,\phi_j)$, i = 1, M, j = 1, N, associated with the i j-th pair of spatial angles, θ_i, ϕ_j, and the vector $\vec{R}_{ij}$ which points from the receiver along the direction defined by this pair of angles. This vector intersects the ground, or xy-plane, at a point whose coordinates are (x_i,y_j) at the center of the i j-th cell defined in the ground plane grid mesh. Now, as the receiver, or aircraft, moves to a new position, the vector $R_{i'j'}$ intersects the ground plane at a new point $(x_{i'}, y_{j'})$. A search is made to determine in which cell, of the original grid mesh, this point lies, and let us call it the k ℓ-th cell. In this case, the phase angle $\psi_D(\theta_{i'},\phi_{j'})$ is set equal to $\psi_D(\theta_k, \phi_\ell)$. If the k ℓ-th cell falls outside the boundaries of the original grid mesh, then $\psi_D(\theta_k, \theta_\ell)$ is chosen randomly and independently, once again, from the interval $(-\pi,\pi)$ and set equal to $\psi_D(\theta_{i'}, \phi_{j'})$. This procedure is repeated a number of times, depending on the number of receiver positions which are of interest. We note that to obtain the total signal at the receiver due to the diffuse scattering from the ground, it is necessary to sum the contributions for the individual waves for

all angles θ_i, ϕ_j, i = 1, M, j = 1, N. In addition, the computer program limits the total number of multipath components to be less than or equal to 25, i.e., $MN \leq 25$. This is found to be adequate for considering only those components with significant amplitude, as noted previously.

The computations required for the planar directional angles, fractional Doppler frequency and relative time delay, for each diffusely scattered ground multipath component, are similar to those for the specular ground reflection given previously in Eqs. (II-23) - (II-28).

B. Computer Validation Data

We now present some computer validation results for the multipath subroutine which performs the computations for diffuse scattering from the ground which were described in Section V A. In order to do this, we have plotted in Fig. V-2 contours of constant levels, in dB, for $K(\theta,\phi)$, as given in Eq. (V-10), versus the angles θ and ϕ. This diagram corresponds to that given in Fig. 45, p. 96, by McGarty.[17] It is seen that the two sets of data agree quite well, so that they serve, at least, as a partial check for the program.

In Fig. V-3, we have plotted $\max_{-\pi\leq\theta,\phi\leq\pi} V_D(\theta,\phi)$ for a typical linear 3° flight path. The fluctuation of this multipath component is seen from this figure to be quite rapid along the flight path. In addition, the level of this multipath component is quite small, on the order of -35 dB, and less. This behavior appears to be quite typical for the diffuse ground scattered multipath component. It should be observed that the low level of this multipath component tends to make it relatively unimportant for the evaluation of MLS performance by means of the computer simulation program.

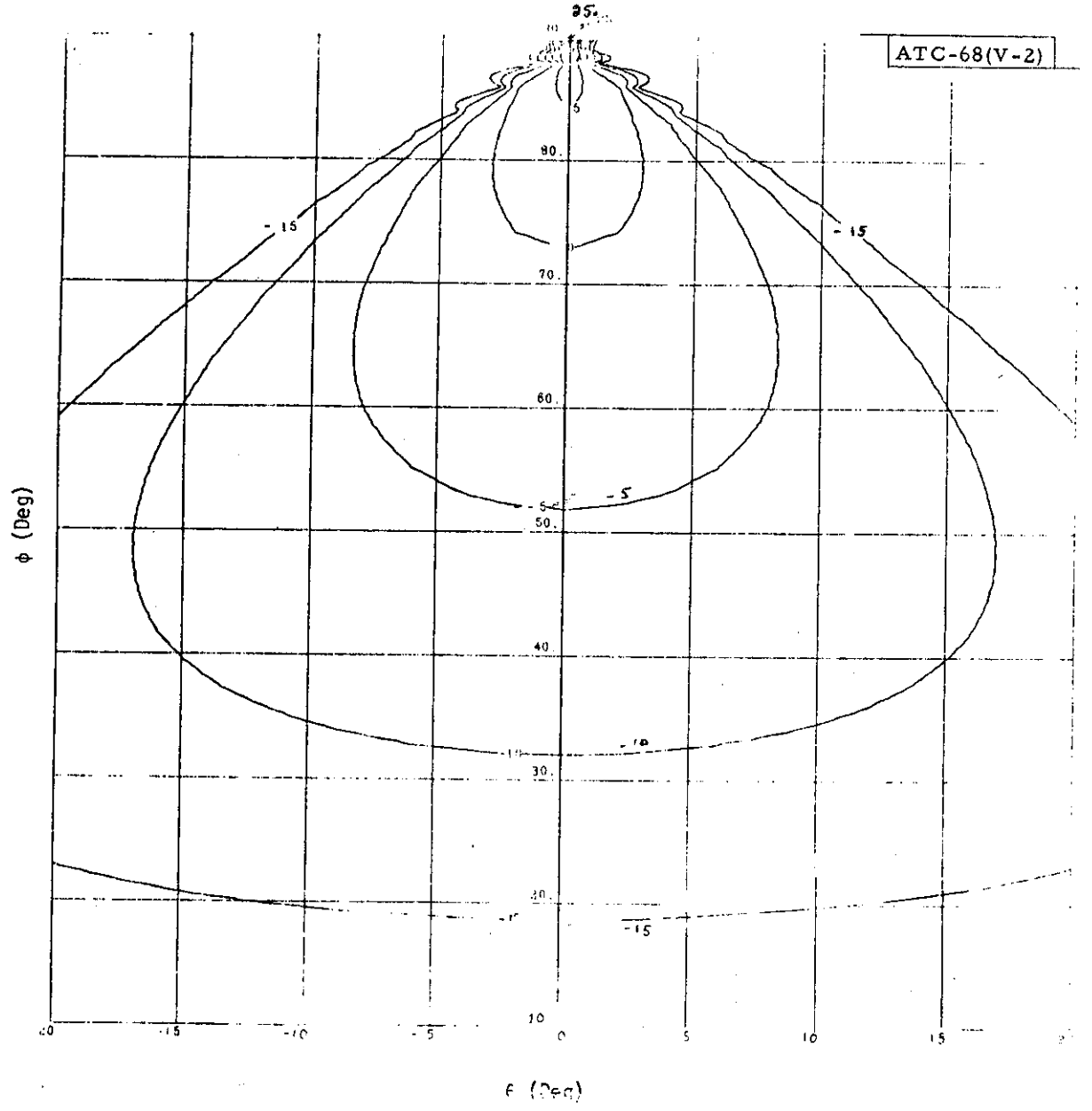

Fig. V-2. Contours of channel spread function, $K(\theta,\phi)$, in dB vs θ and ϕ for transmitter at (0, 0, 3281), receiver at (32810, 0, 66) σ_h = 1', σ_ℓ = 4'.

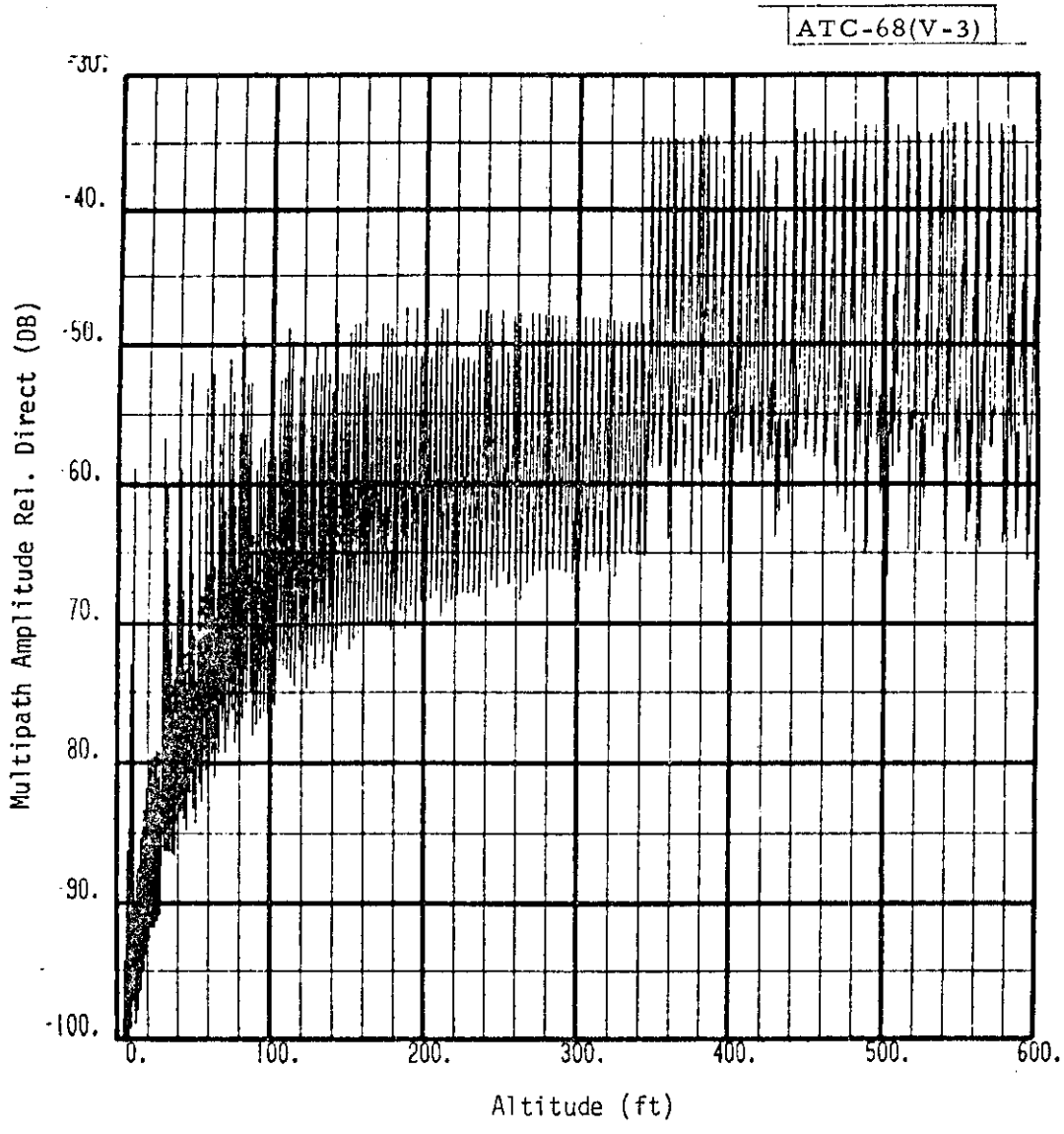

Fig. V-3. Plot of amplitude, in dB, of diffuse ground scattering multipath component, with largest amplitude, vs altitude for transmitter at (-500, 0, 8), receiver on linear 3° flight path between (9000, 0, 0) and (21000, 0, 600), σ_h = 0.5', σ_ℓ = 1.0'.

It should be mentioned that the computer program which computes the amplitudes of the diffusely scattered ground multipath components requires a considerable amount of computer time per flight evaluation point, typically about 0.1 seconds of IBM 370/168 computer time, cf. Section VIII. Thus, there is an option in the program which enables one to skip this computation and perform only those for the other multipath parameters. This latter computation does not require a significant amount of computer time. The operation of this computer program can be determined from the flow chart given in Fig. V-4.

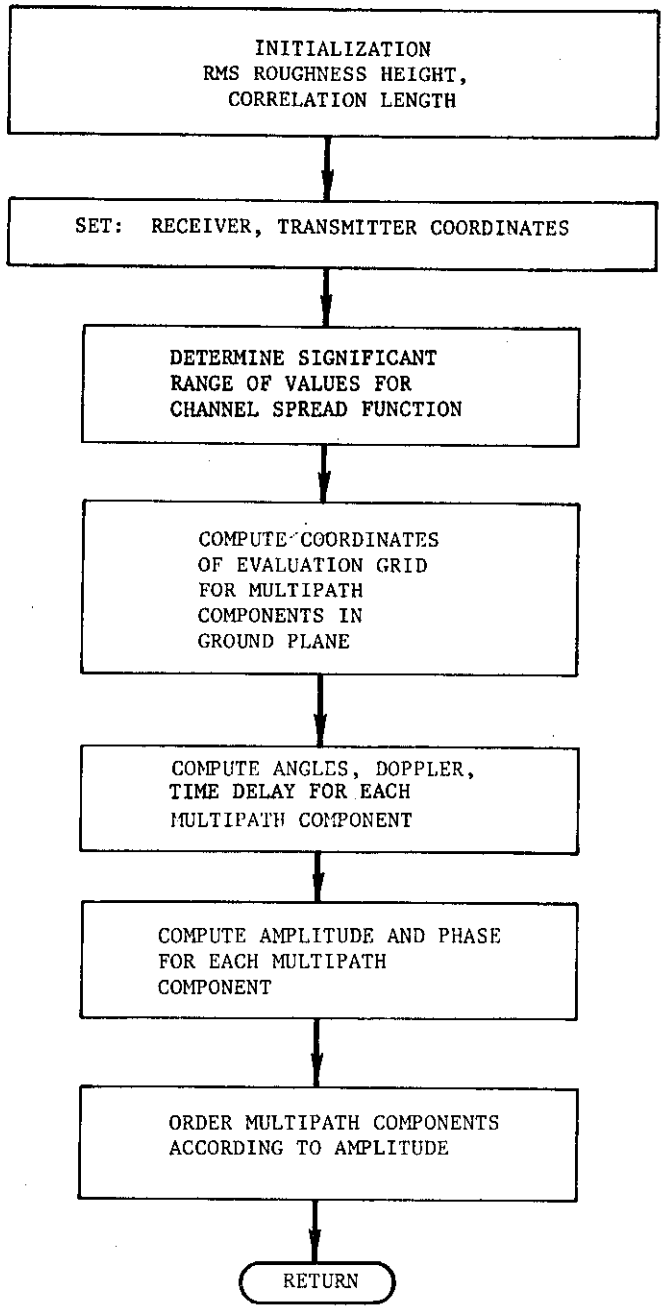

Fig. V-4. Flow chart for program which computes multipath parameters for diffuse scattering from ground.

VI. SHADOWING DUE TO RUNWAY HUMPS

A. Circular Cylindrical Model For Runway Hump

A discussion is now presented of the shadowing, or attenuation, of the directly transmitted signal due to the convex runway surfaces, or humps, which occur in a typical airport environment. It is assumed that a circular cylindrical model can be employed for the runway hump, as shown in Fig. VI-1. The hump is assumed to lie on the runway, so that the axis of the cylinder is perpendicular to the xz-plane of the standard coordinate system shown in Fig. II-1. The circular cylindrical runway hump thus straddles the x-axis of the standard coordinate system shown in Fig. II-1. In order to have shadowing take place, it is assumed that both the transmitter and receiver must lie close to the xz-plane. In Fig. VI-1 we have shown a side view of the runway hump. This view represents a coordinate system which has been rotated from the standard coordinate system into that defined by the line-of-sight vector between the transmitter and receiver. All computations are performed in this rotated coordinate system.

It is easily seen from Fig. VI-1 that

$$S_1 = (T_x^2 + T_z^2 - a^2)^{1/2} \quad , \qquad \text{(VI-1)}$$

$$S_2 = (R_x^2 + R_z^2 - a^2)^{1/2} \quad , \qquad \text{(VI-2)}$$

where a is the radius of the circular cylindrical runway hump, as shown in Fig. VI-1. We also have

$$\theta_2 = \tan^{-1}(R_z/R_x) \quad , \qquad \text{(VI-3)}$$

ATC-68(VI-1)

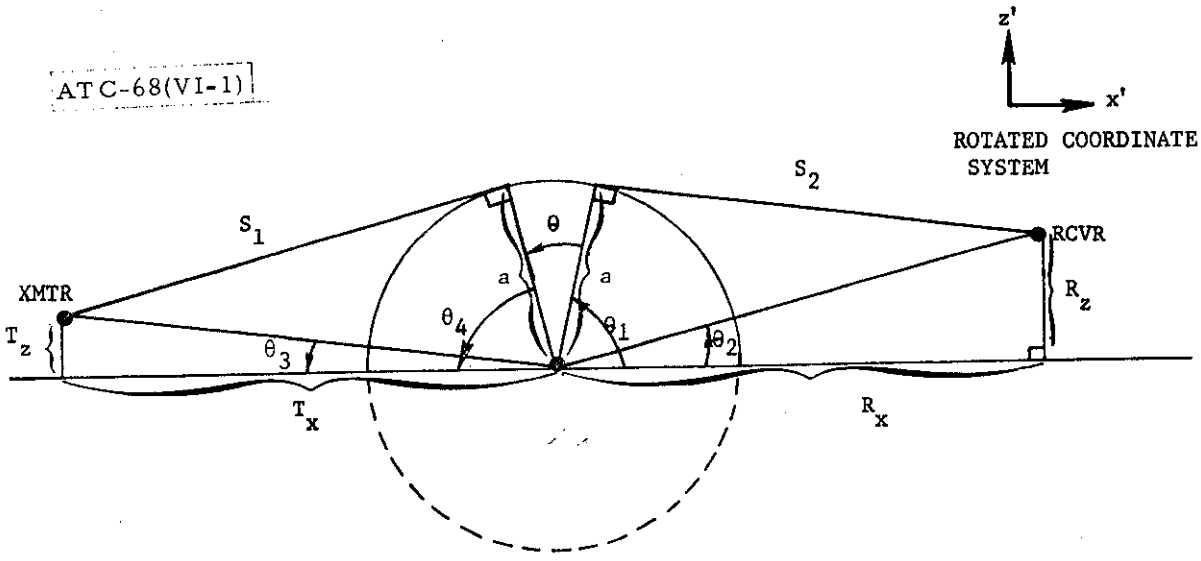

Fig. VI-1. Side view of runway hump.

$$\theta_1 = \theta_2 + \tan^{-1}(S_2/a) \quad , \tag{VI-4}$$

$$\theta_3 = \tan^{-1}(T_Z/T_X) \quad , \tag{VI-5}$$

$$\theta_4 = \theta_3 + \tan^{-1}(S_1/a) \quad , \tag{VI-6}$$

so that the angle θ may be determined from Eqs. (VI-3) - (VI-6) as

$$\begin{aligned}\theta &= \pi - \theta_1 - \theta_4 \\ &= \pi - \tan^{-1}(R_Z/R_X) - \tan^{-1}(S_2/a) \\ &\quad - \tan^{-1}(T_Z/T_X) - \tan^{-1}(S_1/a) \quad .\end{aligned} \tag{VI-7}$$

The ratio of the diffracted wave to free-space signal has been shown by Wait and Conda[18] to be given by

$$\frac{E_D}{E_0} = \left\{ \frac{\varepsilon^{j\pi/4}}{\sqrt{2}} \left(F(\infty) - F\left(\sqrt{\frac{2}{\pi}}\,\alpha\right)\right) - \frac{G(X)}{u}\, \varepsilon^{-j\alpha^2} \right\} \quad , \tag{VI-8}$$

where $F(x)$ is the Fresnel integral defined previously in Eq. (II-34),

$F(\infty) = \dfrac{\varepsilon^{-j\pi/4}}{\sqrt{2}}$, and

$$X = \left(\frac{ka}{2}\right)^{1/3} \theta \quad , \tag{VI-9}$$

$$\alpha = \left(\frac{2kS_1S_2}{S_1 + S_2}\right)^{1/2} \left(\frac{\theta}{2}\right) \quad , \qquad \text{(VI-10)}$$

$$u = \frac{\alpha}{X} = \left(\frac{2kS_1S_2}{S_1 + S_2}\right)^{1/2} \frac{(2/ka)^{1/3}}{2} \quad , \qquad \text{(VI-11)}$$

where k is the wavenumber. The complex-valued function G(x) has been given by Wait and Conda[18] in Fig. 2 on p. 187. In particular, we are interested in their function G(x) depicted in Fig. 2b since it applies to the case of horizontal polarization, or for the case of vertical polarization, dielectric surface, as implied by Wait and Conda.[18]

We have used the following approximations for the real and imaginary parts of G(x)

$$\mathrm{Re}\{G(x)\} = -0.216\,x^2 - 0.593x + 0.103 \quad , \quad -2 \leq x \leq -1$$

$$= -0.133x + 0.346, \quad -1 < x \leq 1.25$$

$$= 0.09067x^2 - 0.388x + 0.52333, \quad 1.25 < x \leq 2.00$$

$$= \frac{\cos\left(\frac{\pi}{4}\right)}{2x\sqrt{\pi}} = 0.1994711/x, \text{ asymptotic case} \qquad \text{(VI-12)}$$

$$\text{Im}\{G(x)\} = -0.24x^2-0.36x-0.22, \quad -2 \leq x \leq -1$$

$$= -0.0704x^2-0.0616x-0.0912, \quad -1 < x \leq 0.125$$

$$= 0.03371x^2-0.06629x-.09224, \quad 0.125 < x \leq 2.0$$

$$= -\frac{\sin(\frac{\pi}{4})}{2x\sqrt{\pi}} = -0.1994711/x, \text{ asymptotic case.} \qquad \text{(VI-13)}$$

We have plotted the real and negative imaginary parts of G(x) in Fig. VI-2. A comparison of this figure with Fig. 2b of Wait and Conda,[18] p. 187, shows that a good approximation for G(x) has been obtained.

The amplitude and phase of the direct wave, after the effect of shadowing is taken into account, are obtained from Eq. (VI-8) as

$$V_{SH} = \left|E_D/D_0\right| \quad , \qquad \text{(VI-14}$$

$$\phi_{SH} = \text{ARG}\{E_D/E_0\} \quad . \qquad \text{(VI-15)}$$

The relative time delay of the shadowed direct wave is taken to be zero. If the line of sight between the transmitter and receiver lies above the top of the runway hump, then the planar directional angles and fractional Doppler frequency of the shadowed direct wave are computed as indicated previously in Section II A, Eqs. (II-23) - (II-27). If this line of sight falls below the

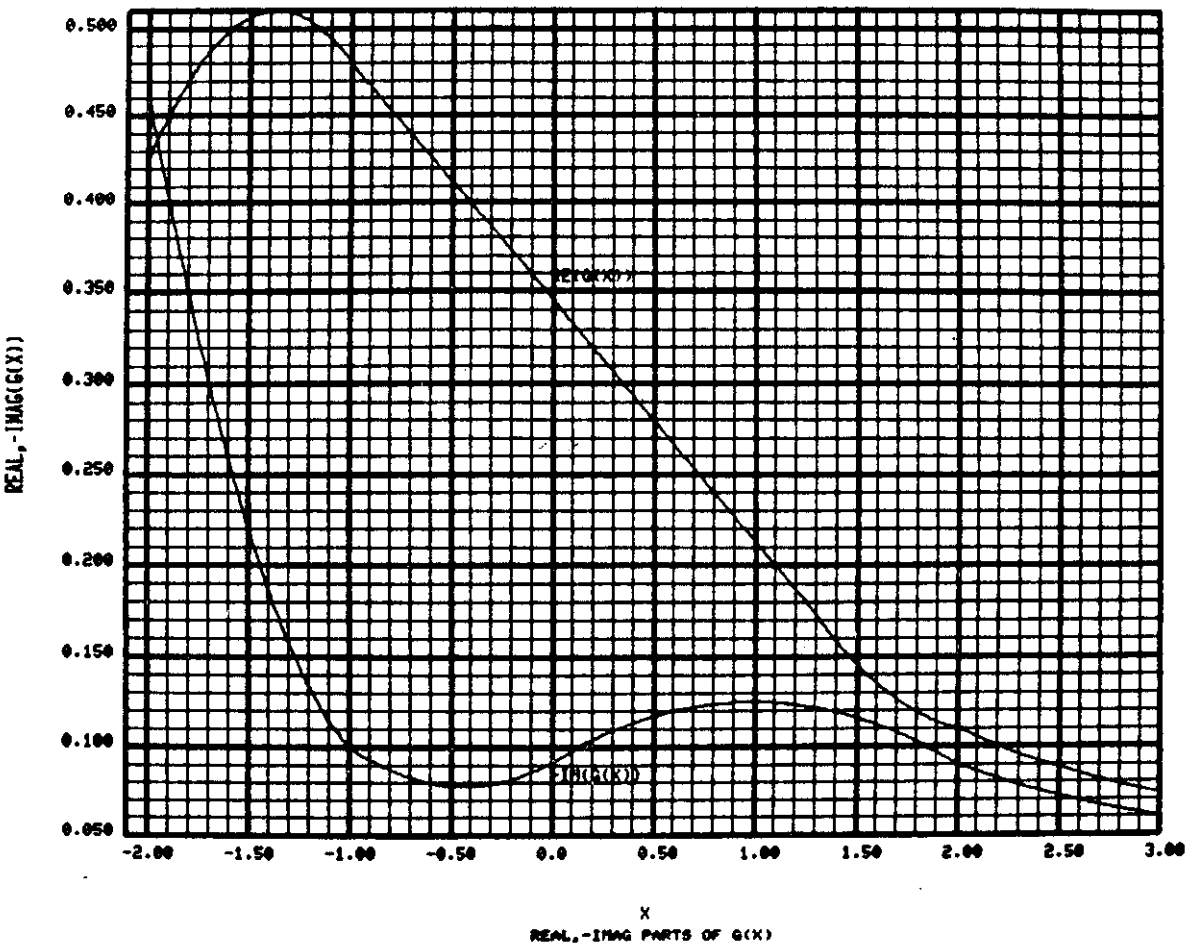

Fig. VI-2. Plots of real and negative imaginary parts of G(x) vs x.

top of the hump, then it is repositioned to obtain an equivalent specular point, so to speak, at the top of the hump. Using the coordinates of this equivalent specular point, the planar directional angles and fractional Doppler frequency are computed in the usual manner.

If the shadowing effect due to a runway hump is computed using the preceding algorithm, then the computation of the specular ground reflection multipath component, outlined in Section II, is omitted. The reason for this is that the shadowed direct wave includes this component as a consequence of the theoretical development due to Wait and Conda[18] which has been employed in the computations.

It is desirable to check for certain conditions in order to determine whether it is appropriate to compute the shadowing effect due to a runway hump using the preceding algorithm. If any one of the following conditions is true, then the shadowing effect is not determined and the computation is performed for the multipath component due to specular ground reflection indicated in Section II. This multipath component is then used along with the unattenuated direct wave to determine the total signal observed at the receiver. These conditions are

(A) $u \leq 0.7$,

(B) $X \leq -2$,

(C) $u' \leq 0.65$,

$\alpha \leq 0$,

(D) Receiver or transmitter position interior to runway hump,

(E) Receiver and transmitter positions on same side, relative to top of runway hump,

(F) Runway hump is not in line of sight,

(G) System is EL1 or EL2, but not azimuth or DME,

where u' is defined in a manner similar to u given in Eq. (VI-11) except that distances S_1', S_2' are used, which are defined as distances from the top of the runway hump to the transmitter and receiver, respectively. Conditions (A) and (B) were obtained from the results of Wait and Conda,[18] and are related to the criteria required for their solution to be applicable. The condition (C) was obtained empirically by attempting to match the results of the computation with experimental data due to the R.A.E. (U.K.).[19] taken at C-band at Bedford airport, which will be discussed extensively in Section VI B. This latter condition is required in order to limit the applicability of the solution when the receiver position is close to the top of the runway hump.

Conditions (D), (E) and (F) are obvious ones and require no explanation, while condition (G) is required since runway hump shadowing occurs for azimuth and DME systems but not for EL1 and flare systems. The reason for this is that the azimuth and DME systems are usually located beyond the stop end of the runway, while EL1 and flare are located off to the side of the runway, near the glide path intercept point, so that these former systems will have their transmitted signals shadowed by the hump, but these latter systems will not be shadowed from the receiver.

B. Comparison Of Results With Experimental Measurements

The flow chart for the computer program which determines the shadowing effect due to a runway hump is given in Fig. VI-3. We now wish to compare the results obtained with this subprogram with some experimental measurements due to Neugebauer and Bachynski.[20] These data were obtained from model experiments made in the laboratory at K-band. The geometry of the diffraction experiment is shown in Fig. VI-4 along with the corresponding results obtained using the computational procedure given in Section VI A. In particular, we have plotted

$$P = 20\ \mathrm{LOG}_{10}\ (V_{SH}) - 8 - 20\ \mathrm{LOG}_{10}\ (\frac{D + 30}{70}) \quad , \qquad \text{(VI-15)}$$

where D is the distance from the top of the knife edge. The last two terms in Eq. (VI-15) represent the path loss, in dB, due to distance and can be derived from the results for diffraction by a knife edge[21] given in Fig. 7b of reference 20 by noting that the diffraction loss is 6 dB when the receiver is at the same height as the top of the knife edge.

If we compare the results of Fig. VI-4 with those in Fig. 8b of reference 20 , we see that there is excellent agreement. These latter results have been plotted as a function of wavelength, but the wavelength can be considered to be a normalizing parameter so that a correspondence with the present results may be made by letting λ = 0.2 feet, which is the wavelength, at C-band

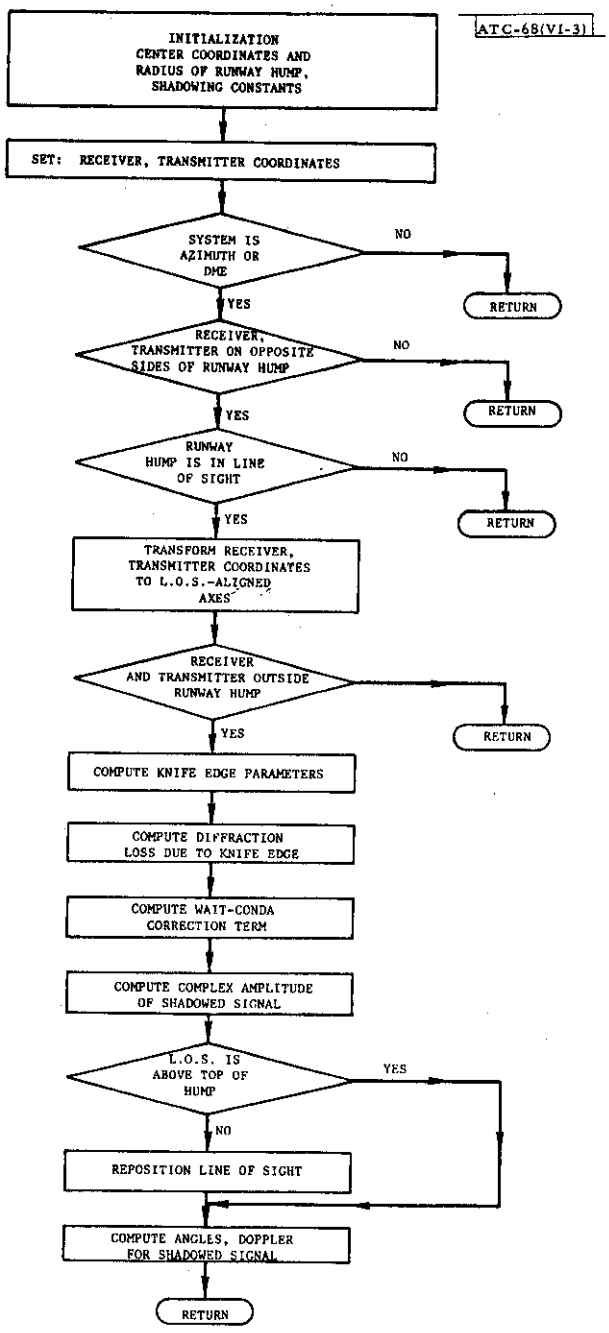

Fig. VI-3. Flow chart for program which computes shadowing effect due to runway hump.

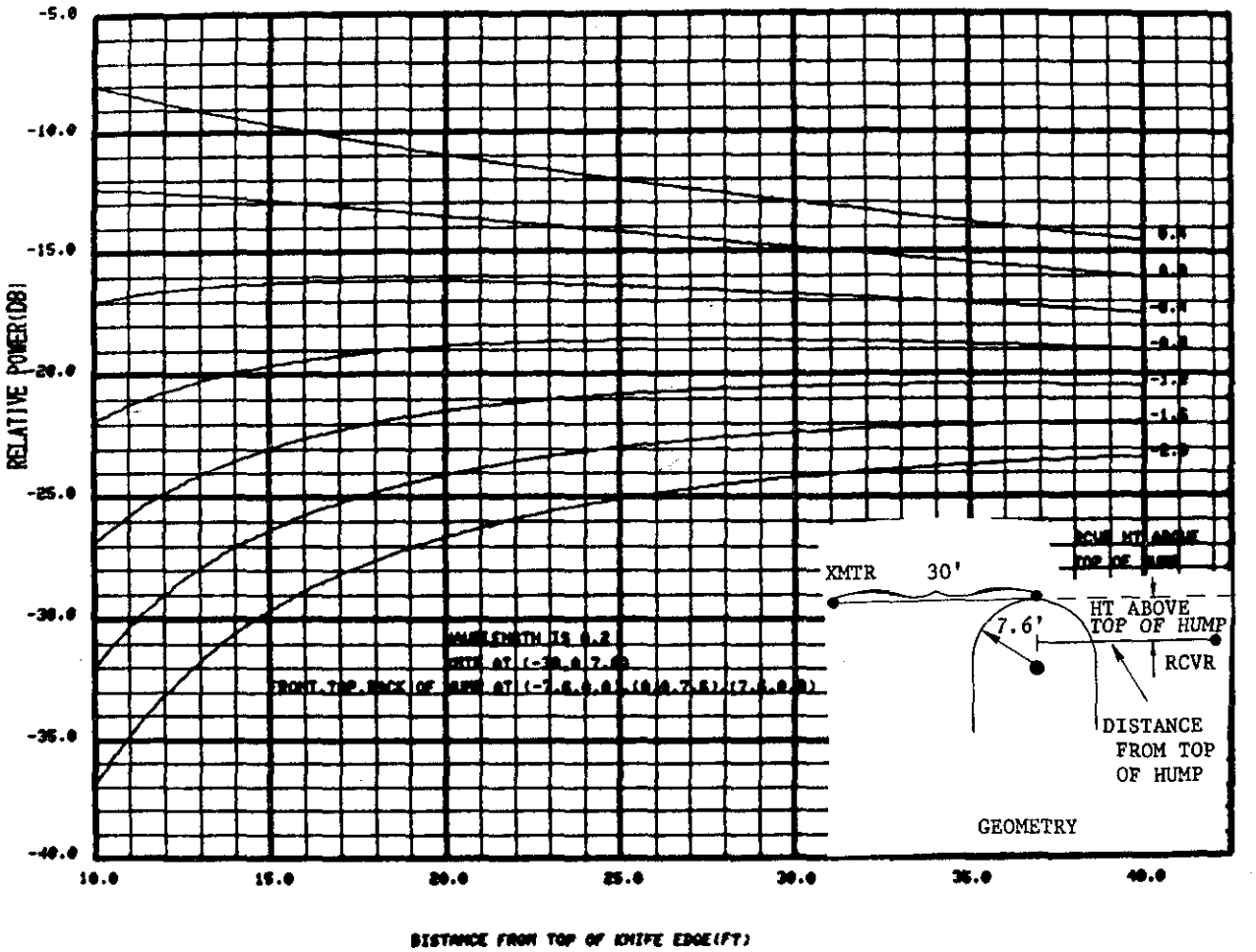

Fig. VI-4. Results of computation for relative power of signal observed behind circular cylindrical hump vs distance from top of hump, for various receiver heights above top of hump.

that was employed in the computations. This correspondence has also been made by Wait and Conda,[18] cf. Fig. 4b, p. 189.

A comparison is now given of the computational results obtained for the signal loss due to runway hump shadowing, as outlined in Section VI A, with some experimental data due to the R.A.E. (U.K.).[19] These data are shown in Fig. VI-5 which depicts the C-band signal loss along the Bedford main runway, as well as the runway profile. The corresponding computational results are also shown in Fig. VI-5, and it is seen that there is reasonably good agreement between the two sets of data all along the runway. This agreement was also observed between the R.A.E.[19] experimental data at the Farnborough main runway and the corresponding computational results.

We also wish to compare the present computational results with experimental data due to Thomson - CSF.[22] These results are shown in Fig. VI-6, which depicts the C-band signal loss at Coulommiers airport, and the runway profile. The corresponding computational results are also shown in Fig. VI-6 for three possible values for the radius of the circular cylindrical runway hump. The best agreement is obtained for the largest value of the radius for which there is excellent agreement with the experimental data.

We mention finally that a triangular model was considered for the runway hump, the details of which are presented in reference 19 . However, the computational results obtained for this model could not be made to agree with any of the experimental data due to the R. A. E.[19] at C-band. Thus, this model was abandoned in favor of the circular cylindrical model for the runway hump.

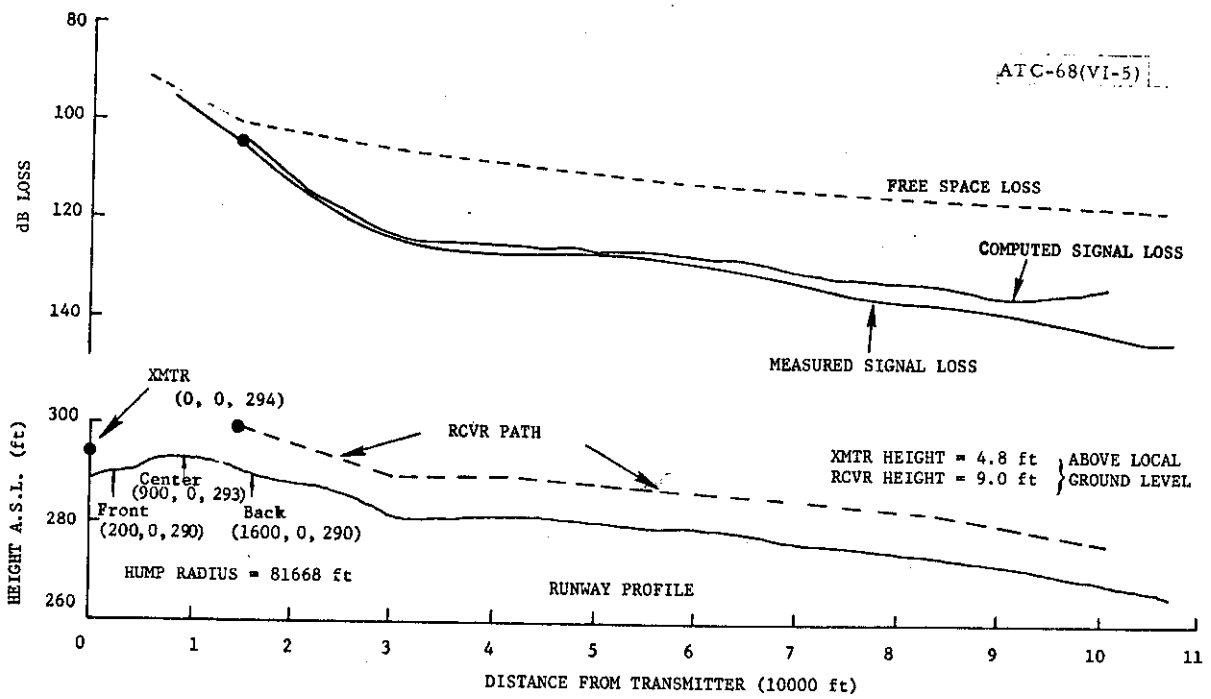

Fig. VI-5. Comparison of computational results with experimental C-band signal shadowing loss measured at Bedford (R.A.E.) main runway.

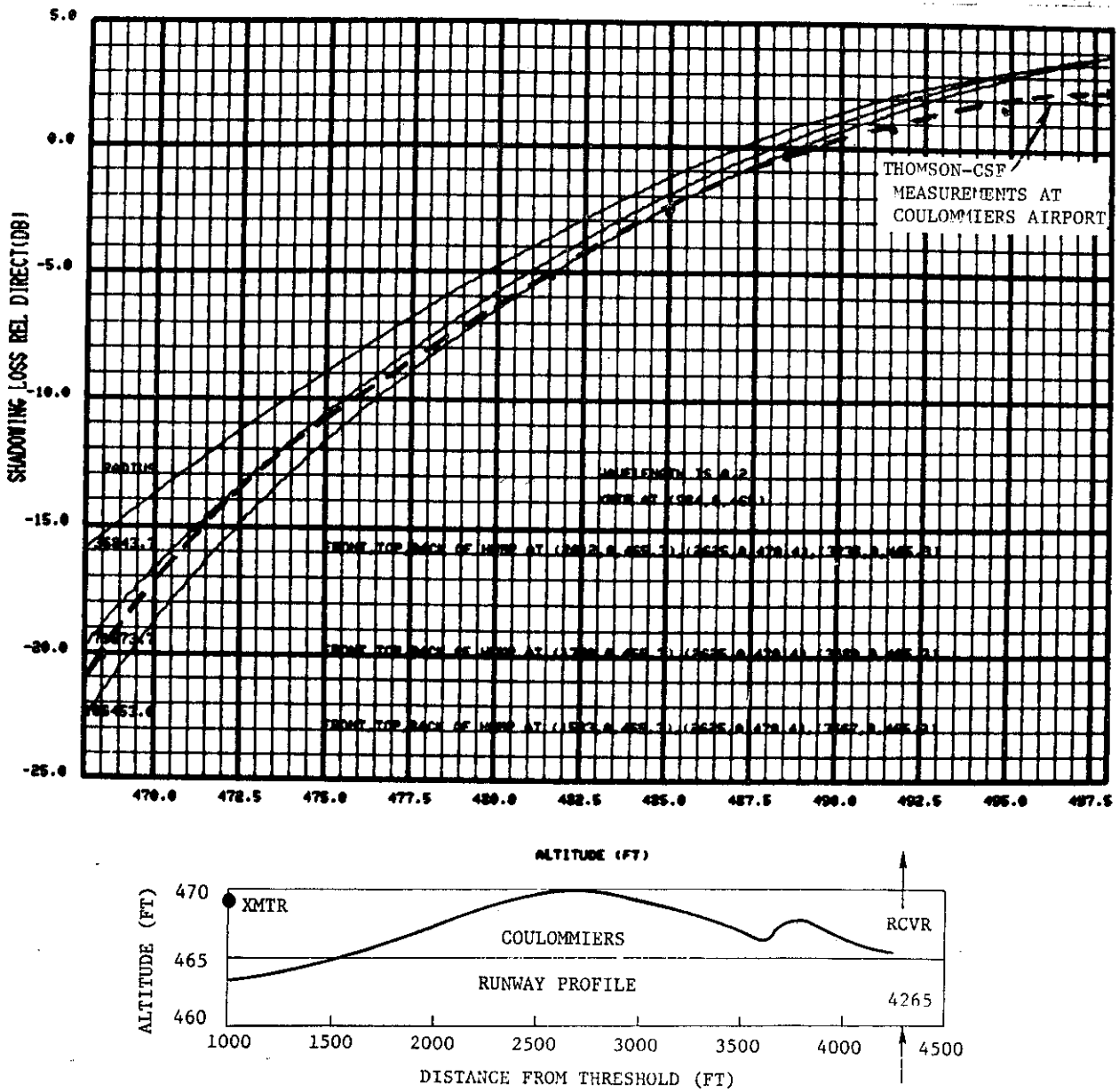

Fig. VI-6. Comparison of computational results with experimental C-band signal shadowing loss measured at Coulommiers (Thomson-CSF) runway.

VII. SHADOWING DUE TO AIRCRAFT OR BUILDINGS APPROACHING LINE OF SIGHT

We now wish to discuss the shadowing, or attenuation, of the directly-transmitted signal due to buildings and aircraft which can lie close to the line of sight between transmitter and receiver. Unlike the situations described in Sections III and IV, the plane containing the obstacle is located between the transmitter and the receiver so that a shadowing, and not a scattering, phenomenon is observed. The shadowing buildings consist typically of hangars, or large-size trucks, located at the side of the runway, while the shadowing due to aircraft can occur for any of the following situations:

(1) Blockage of transmitted signal by another landing aircraft on the same glide path as the aircraft receiver.

(2) Blockage of transmitted signal by an aircraft rolling out, or possibly taking off over the azimuth site.

(3) Blockage of transmitted signal by a taxiing aircraft passing through, or very near, the line of sight between the transmitter and aircraft receiver.

These cases are depicted in Fig. VII-1.

A. Models for Shadowing Aircraft and Buildings

For the purpose of computing the shadowing effect, the building is modeled as a vertical flat plate as shown in Fig. VII-2a. This model is similar to that presented in Section III for scattering from buildings, cf. Fig. III-1, with the sole exception that no provision is made for a possible tilt of the

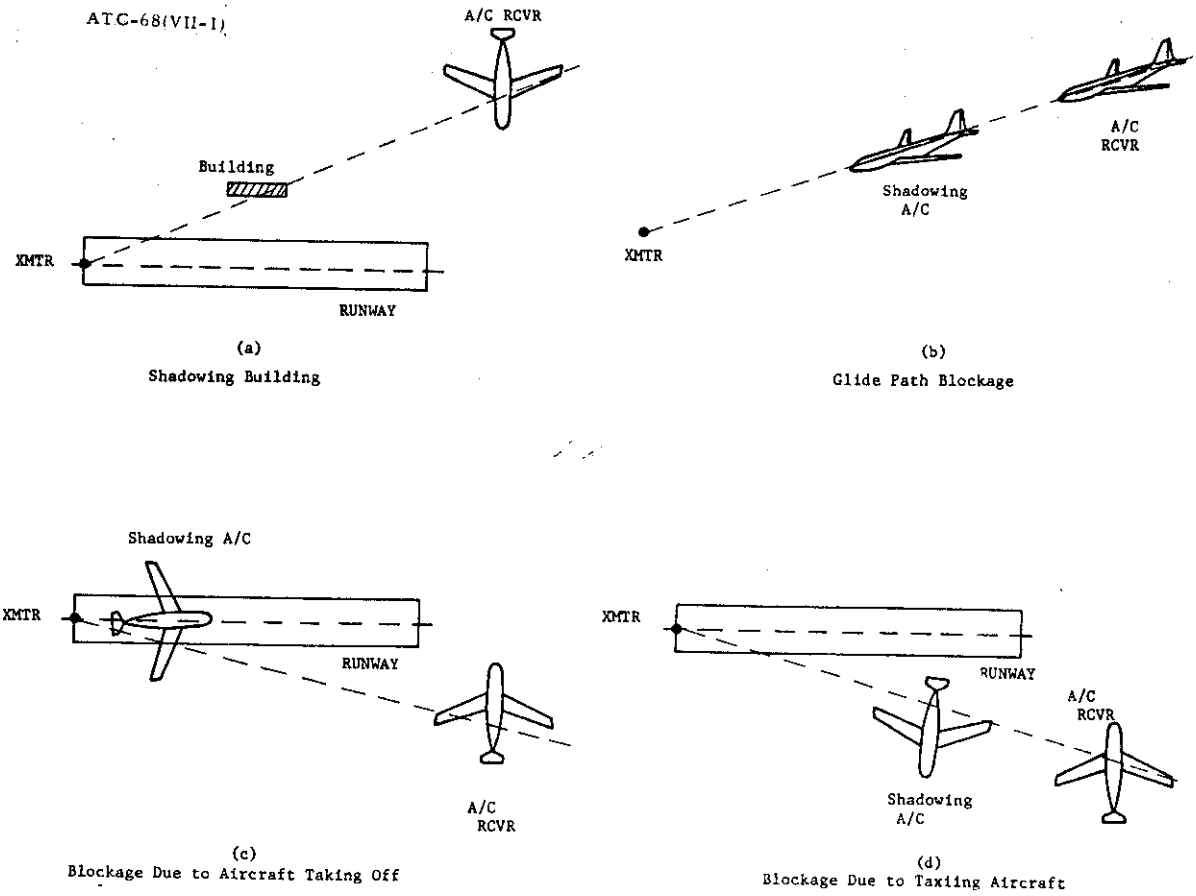

Fig. VII-1. Illustration of shadowing effect due to aircraft and buildings near the line of sight between transmitter and receiver.

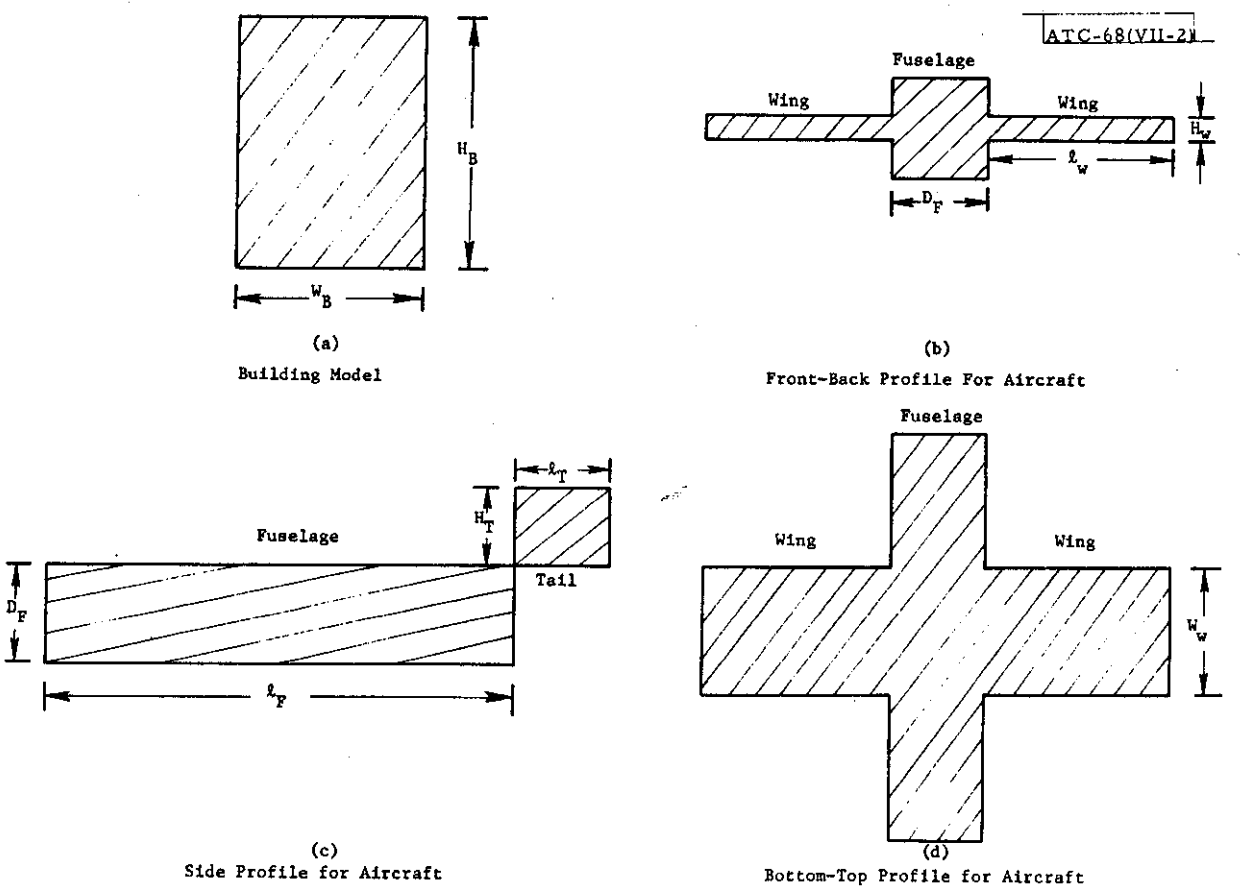

Fig. VII-2. Models used for computing shadowing loss due to aircraft and buildings.

building, relative to the ground plane, in the present case. That is, the shadowing building is assumed to lie in a vertical plane which is perpendicular to the ground plane.

The shadowing aircraft is assumed to be modeled in terms of three possible profiles, as shown in Fig. VII-2b through VII-2d. These profiles are determined by the viewing angles of the shadowing aircraft, as seen from the transmitter. The details of the method used to compute these viewing angles, and the determination of the aircraft profile therefrom, are presented in Appendix H. The front-back, bottom-top, profiles for aircraft, shown in Figs. VII-2b, d, respectively, would be obtained typically for the shadowing aircraft traveling on the same glide path as, and in front of, the aircraft receiver, as shown in Fig. VII-1b,c. However, the side profile for aircraft, shown in Fig. VII-2c, would be obtained typically for the shadowing aircraft taxiing near the runway, as indicated in Fig. VII-1d.

B. Method Based on Computation of Complex Amplitudes of Edge Rays

We now wish to present the method which was employed to compute the shadowing effect due to buildings and aircraft which can lie close to the line of sight between transmitter and receiver. The basis of the method lies in a straightforward application of Babinet's principle, cf. Sommerfeld,[5] p. 204, which states that the field due to a blocking screen, or rectangle, is equal to the unperturbed field less the field through a rectangular opening in an opaque screen. In this result, the shape of the blocking rectangle is, of course, identical to that of the rectangular opening, i.e., these diffraction

openings are said to be complementary.

It was assumed in Section VII A that the shadowing building could be modeled as a rectangular screen, and that the shadowing aircraft could be modeled as three, or possibly two, rectangular screens, cf. Fig. VII-2. Thus, the problem is equivalent to that of diffraction by a rectangular opening in an opaque screen as shown in Fig. VII-3. The y'z'-axes are located in the plane defined by the rectangular opening, with the origin located at the center of the rectangle, as depicted in Fig. VII-3. The coordinates of the transmitter and receiver must be obtained by means of a transformation of coordinates. For the case of a shadowing building, these transformations are similar to those given in Appendix E, with the sole exception that the second transformation of coordinates due to the tilt angle of the building is not required. When dealing with shadowing aircraft, the transformation of coordinates required is somewhat more complex, and is described in detail in Appendix H. Once the positions of the transmitter and receiver have been determined in the x'y'z'-coordinate system, shown in Fig. VII-3, the point of intersection of the line of sight with the y'z'-plane can be computed in a manner similar to that presented in Appendix E for computing the position of the specular point for scattering from buildings.

Thus, using the results of Sommerfeld,[5] pp. 237-247, we can obtain the complex amplitude of the received signal due to plane wave blockage by a rectangular obstacle which is the complement of the rectangular opening shown in Fig. VII-3, relative to the receiver signal with no obstacle present, as

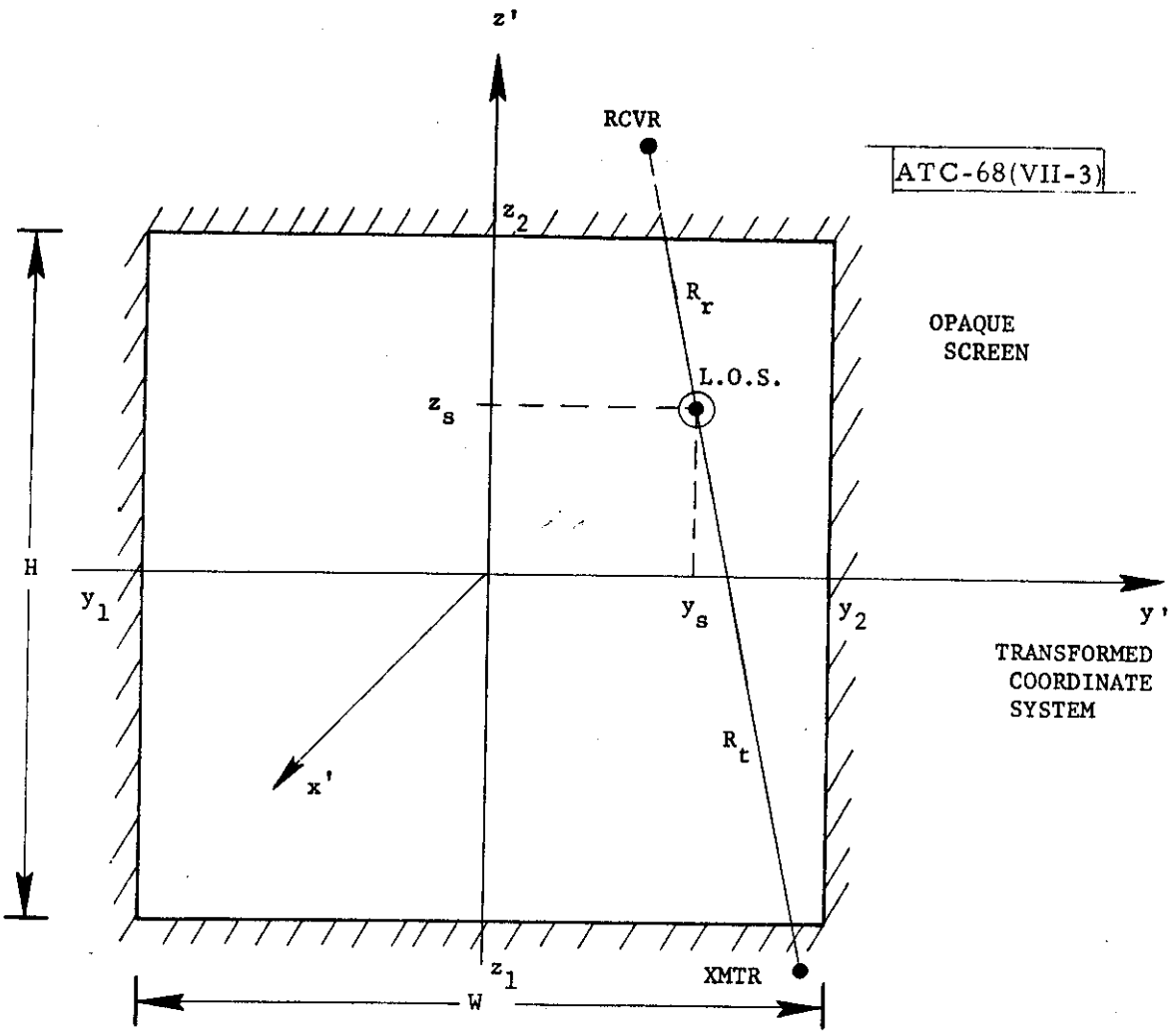

Fig. VII-3. Geometry for diffraction by rectangular opening in opaque screen.

$$V_{SH} = 1 - \frac{e^{j\pi/2}}{2}\left[F(\tilde{y}_2) - F(\tilde{y}_1)\right]\left[F(\tilde{z}_2) - F(\tilde{z}_1)\right] \quad , \quad \text{(VII-1)}$$

where

$$\tilde{y}_2 = \sqrt{2}\,(y_2 - y_s)\,(1 - \alpha_1^2)^{1/2}/R_f \quad , \quad \text{(VII-2)}$$

$$\tilde{y}_1 = \sqrt{2}\,(y_1 - y_s)\,(1 - \alpha_1^2)^{1/2}/R_f \quad , \quad \text{(VII-3)}$$

$$\tilde{z}_2 = \sqrt{2}\,(z_2 - z_s)\,(1 - \beta_1^2)^{1/2}/R_f \quad , \quad \text{(VII-4)}$$

$$\tilde{z}_1 = \sqrt{2}\,(z_1 - z_s)\,(1 - \beta_1^2)^{1/2}/R_f \quad , \quad \text{(VII-5)}$$

where α_1, β_1 are the direction cosines of the line of sight relative to the y', z'-axis, respectively, R_f is the Fresnel zone size defined previously in Eq. (III-7) and F(x) is the Fresnel integral defined previously in Eq. (II-34). If the blocking obstacle consists of two, or possibly three blocking rectangles, such as shadowing aircraft, then we may use the principle of superposition to modify the result given in Eq. (VII-1) for a single rectangle. In this case we need only subtract from the second term given in Eq. (VII-1) the appropriate products of Fresnel integrals evaluated at the appropriate rectangular edges. The approximations involved in using Eq. (VII-1), when α_1, or β_1, or both, are not equal to zero, are similar to those discussed previously in Section III B and Appendix F.

In order to proceed with the description of the method, it is desirable to consider two different types of systems, namely:

(1) Azimuth system,

(2) DME, or Elevation system.

The azimuth, DME, and elevation systems comprise, of course, a complete MLS system and provide all of the landing guidance information for MLS. It is assumed that the two-dimensional transmitter radiation pattern, for both types of systems listed above, can be approximated as a product of one-dimensional patterns. One dimension consists of the azimuth direction, while the other consists of the elevation direction. It is also assumed that the azimuth direction is along the y'-axis, while the elevation direction is along the z'-axis, where these axes are contained in the plane of the diffraction aperture for the canonical case illustrated in Fig. VII-3. This is a reasonable assumption for the building model, and for the front-back, and side, profiles for the aircraft model, cf. Fig. VII-2. It is also a reasonable assumption for the bottom-top profile for the aircraft model shown in Fig. VII-2d, provided that the aircraft is making a centerline approach to the runway. If the aircraft fuselage axis makes a large angle with respect to the runway centerline, or xz-plane depicted in Fig. II-1, then the assumption is no longer valid and should be considered as an approximation. The azimuth system is assumed to have an azimuthal pattern which is narrow, or selective in the y'-direction, and an elevation pattern which is broad, or non-selective in the z'-direction. The DME and elevation systems are assumed to have an azimuthal pattern that is broad and an elevation pattern which is narrow.

We now consider the azimuth system. For this system it is necessary to analyze three cases, cf. Fig. VII-3, as follows:

(A) $W > R_f$, line of sight intersects $y'z'$-plane outside obstacle, or rectangle,

(B) $W > R_f$, line of sight intersects $y'z'$-plane inside obstacle,

(C) $W < R_f$, all line of sight cases.

These three cases comprise all possible situations. In each case the received signal is expressed as a sum of rays, as given in the following table:

Case	Number of Rays
A	2 edge rays plus direct wave
B	3 edge rays only, no direct wave
C	1 edge ray plus direct wave

The manner in which the directions of these edge rays are determined for cases A-C is depicted in Figs. VII-4 through VII-6, respectively. In these figures the point marked "x" represents the point at which the edge ray path intersects the $y'z'$-plane, or diffraction aperture, so that its propagation path extends from the transmitter to the point x, and thence to the receiver.

It now remains to describe how the complex amplitudes are assigned to these edge rays. These complex amplitudes of the edge rays, for the various cases, are assigned as follows, where L.O.S. denotes line of sight:

Case A ($W > R_f$, L.O.S. outside obstacle)

$$A_{\substack{\text{Left-hand}\\ \text{edge}}} = \frac{j}{\sqrt{2}} \rho_z \left[F(\tilde{y}_1) - u\,(\tilde{y}_1, \tilde{y}_2) F(\infty) \right] \quad , \qquad \text{(VII-6)}$$

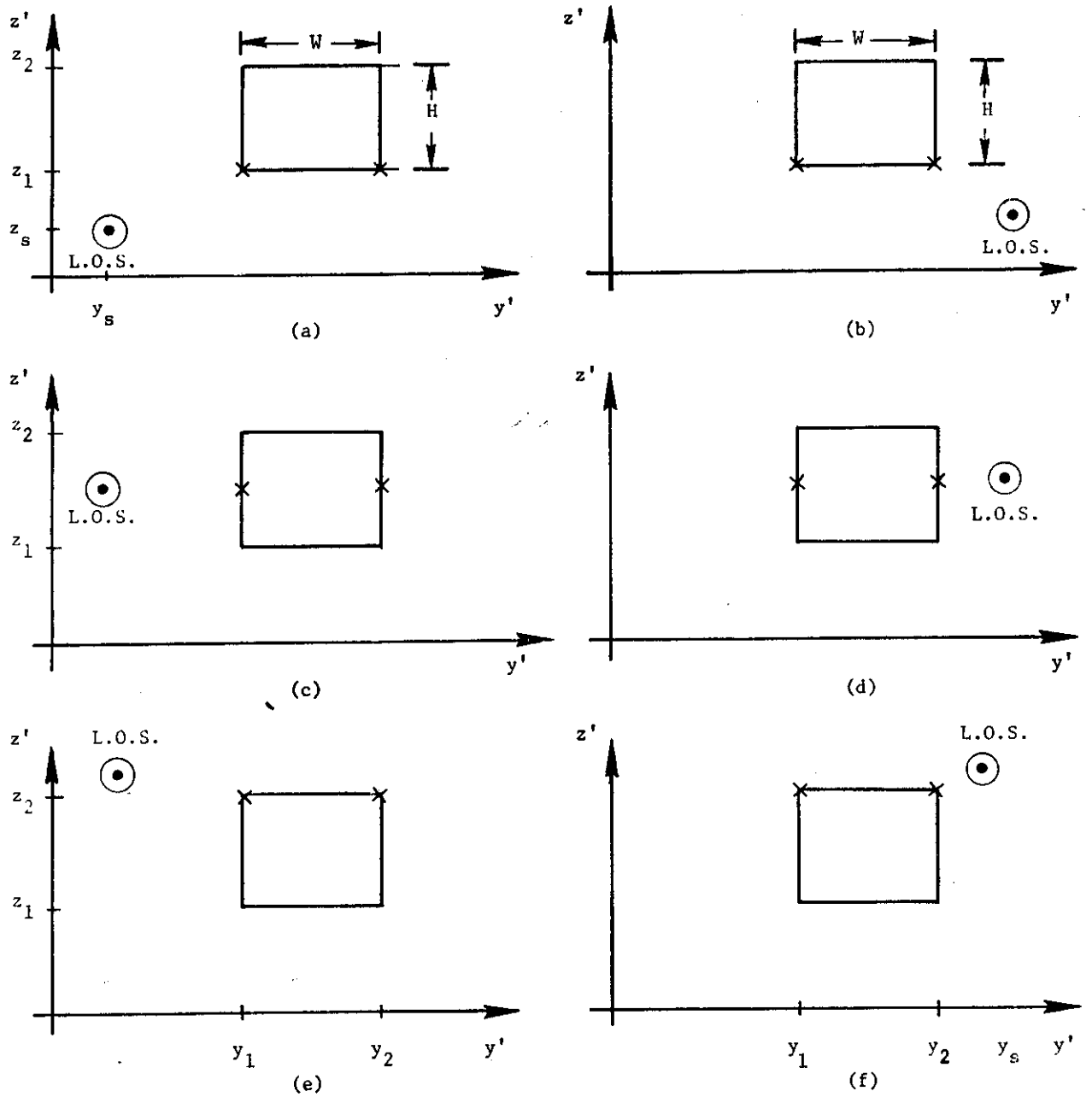

Fig. VII-4. Method for assigning directions to edge rays for azimuth system, when $W > R_f$ and the line of sight is outside the obstacle.

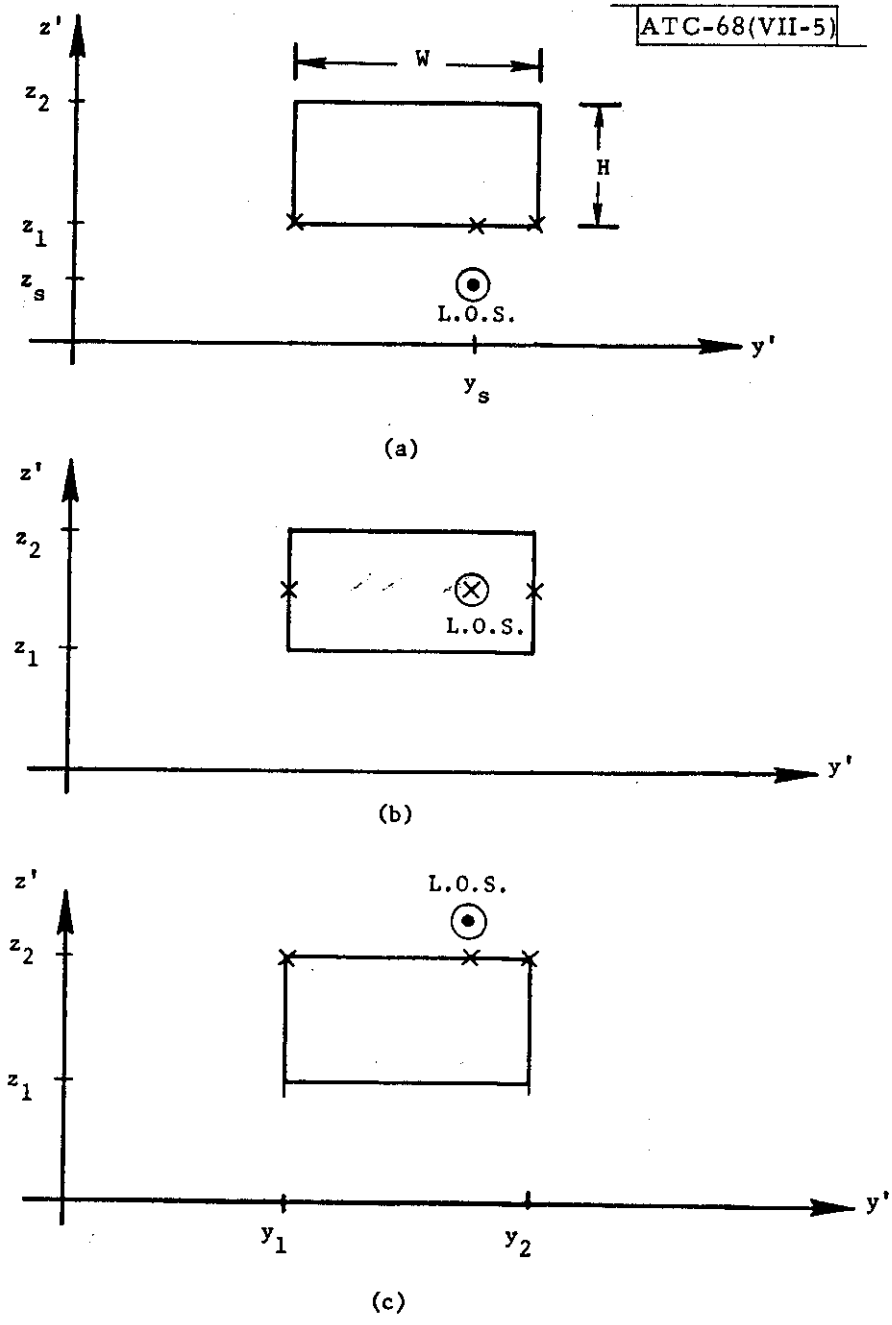

Fig. VII-5. Method for assigning directions to edge rays for azimuth system, when $W > R_f$ and the line of sight is inside the obstacle.

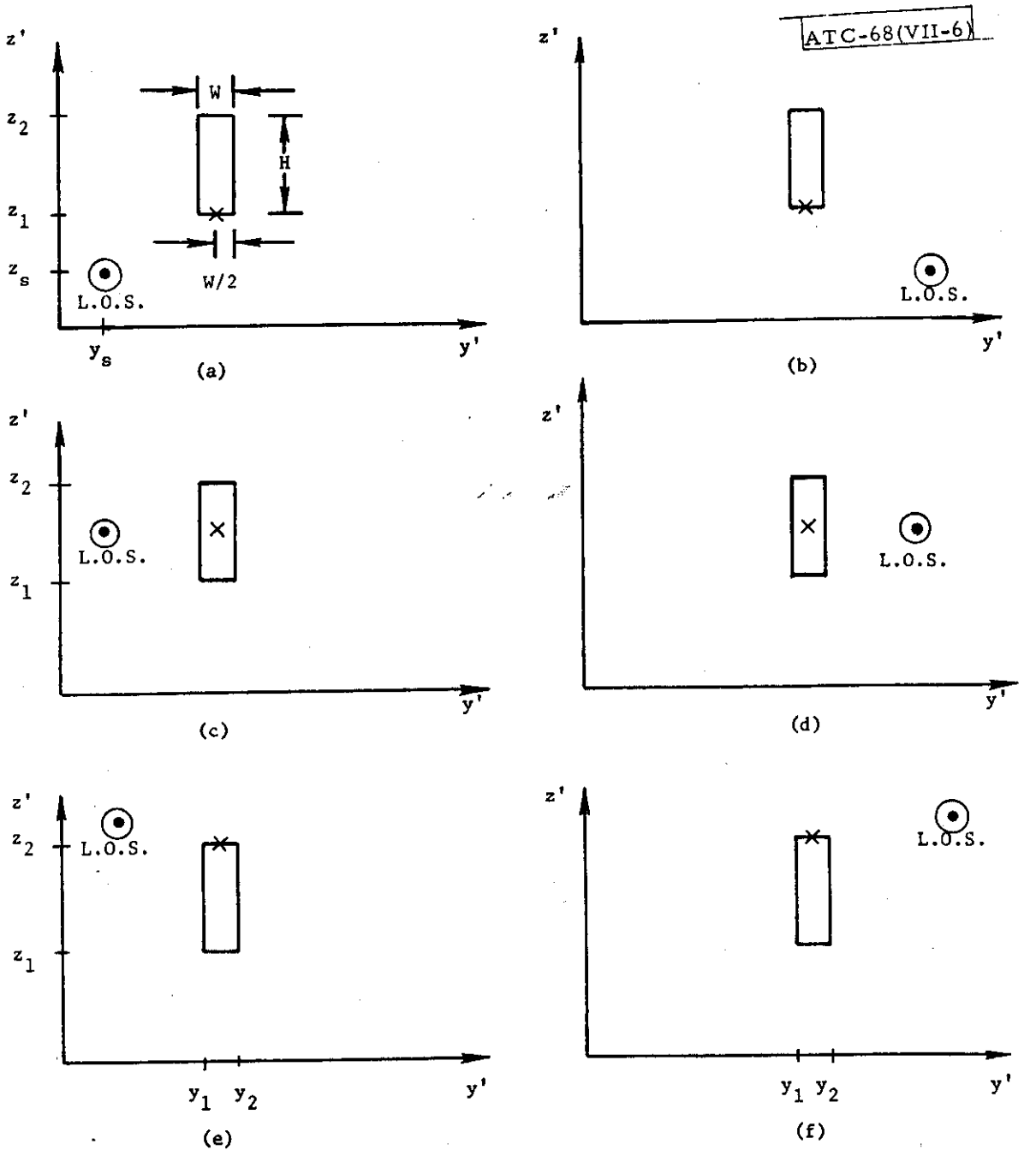

Fig. VII-6. Method for assigning directions to edge rays for azimuth system, when $W < R_f$.

$$A_{\substack{\text{Right-hand}\\ \text{Edge}}} = -\frac{j}{\sqrt{2}}\,\rho_Z\left[F(\tilde{y}_2) - u(\tilde{y}_1,\tilde{y}_2)F(\infty)\right] \quad , \quad \text{(VII-7)}$$

$$A_{\text{Direct}} = 1 \quad , \quad \text{(VII-8)}$$

Case B ($W > R_f$, L.O.S. inside obstacle)

$$A_{\substack{\text{Left-hand}\\ \text{Edge}}} = \frac{j}{\sqrt{2}}\,\rho_Z\left[F(\tilde{y}_1) + F(\infty)\right] \quad , \quad \text{(VII-9)}$$

$$A_{\substack{\text{Right-hand}\\ \text{Edge}}} = -\frac{j}{\sqrt{2}}\,\rho_Z\left[F(\tilde{y}_2) - F(\infty)\right] \quad , \quad \text{(VII-10)}$$

$$A_{\text{Center}} = \left(1 - \rho_Z \varepsilon^{j\pi/4}\right) \quad , \quad \text{(VII-11)}$$

Case C ($W < R_f$)

$$A_{\text{Center}} = -\frac{j}{\sqrt{2}}\,\rho_Z\rho_Y \quad , \quad \text{(VII-12)}$$

$$A_{\text{Direct}} = 1 \quad , \quad \text{(VII-13)}$$

where

$$\rho_Z = \frac{1}{\sqrt{2}}\left(F(\tilde{z}_2) - F(\tilde{z}_1)\right) \quad , \quad \text{(VII-14)}$$

$$\rho_Y = \frac{1}{\sqrt{2}}\left(F(\tilde{y}_2) - F(\tilde{y}_1)\right) \quad , \quad \text{(VII-15)}$$

$$u(\tilde{y}_1,\tilde{y}_2) = +1,\ \tilde{y}_1,\ \tilde{y}_2 \geq 0$$

$$= -1,\ \tilde{y}_1,\ \tilde{y}_2 < 0 \qquad , \quad \text{(VII-16)}$$

$\tilde{y}_2$, $\tilde{y}_1$, $\tilde{z}_2$, $\tilde{z}_1$ were defined previously in Eqs. (VII-2) through (VII-5), respectively, $F(u)$ is the Fresnel integral defined previously in Eq. (II-34), and $F(\infty) = \varepsilon^{-j\pi/4}/\sqrt{2}$.

It is easy to see that in each case A, B, or C, the sum of the complex amplitudes of the edge rays is equal to the expression for V_{SH} given in Eq. (VII-1). Thus, what has been accomplished is to provide a spatial decomposition of the received signal due to blockage by the obstacle. The justification for assigning the complex amplitudes to the edge rays, in the manner given in Eqs. (VII-6) through (VII-13), is based on the notion that the phase shift of the edge ray, relative to the receiver signal with no obstacle present, can be associated with its ray path direction. The theoretical development which shows this is presented in Appendix J. In addition, there is strong justification for this method based on the agreement obtained between the results of this model and some experimental shadowing data obtained in the DABS system. These results are presented subsequently in Section VII C.

We now consider the DME and elevation systems. For these systems we must discuss three cases, which are similar to cases A-C presented previously for the azimuth system, cf. Fig. VII-3, as follows:

(A') $H > R_f$, line of sight intersects y'z'-plane outside obstacle,

(B') $H > R_f$, line of sight intersects y'z'-plane inside obstacle,

(C') $H < R_f$, all line of sight cases.

The number of rays required in cases A'-C' is similar to that in cases A-C for the azimuth system which were presented previously. The manner in which the directions of these edge rays are determined for cases A'-C' is depicted in Figs. VII-7 through VII-9. The complex amplitudes of the edge rays, for the various cases, are assigned as follows:

Case A' ($H > R_f$, L.O.S. outside obstacle)

$$A_{\text{Bottom Edge}} = \frac{j}{\sqrt{2}} \rho_Y \left[F(\tilde{z}_1) - u(\tilde{z}_1, \tilde{z}_2)\, F(\infty) \right] \quad , \quad \text{(VII-17)}$$

$$A_{\text{Top Edge}} = -\frac{j}{\sqrt{2}} \rho_Y \left[F(\tilde{z}_2) - u(\tilde{z}_1, \tilde{z}_2)\, F(\infty) \right] \quad , \quad \text{(VII-18)}$$

$$A_{\text{Direct}} = 1 \quad , \quad \text{(VII-19)}$$

Case B' ($H > R_f$, L.O.S. inside obstacle)

$$A_{\text{Bottom Edge}} = \frac{j}{\sqrt{2}} \rho_Y \left[F(\tilde{z}_1) + F(\infty) \right] \quad , \quad \text{(VII-20)}$$

$$A_{\text{Top Edge}} = -\frac{j}{\sqrt{2}} \rho_Y \left[F(\tilde{z}_2) - F(\infty) \right] \quad , \quad \text{(VII-21)}$$

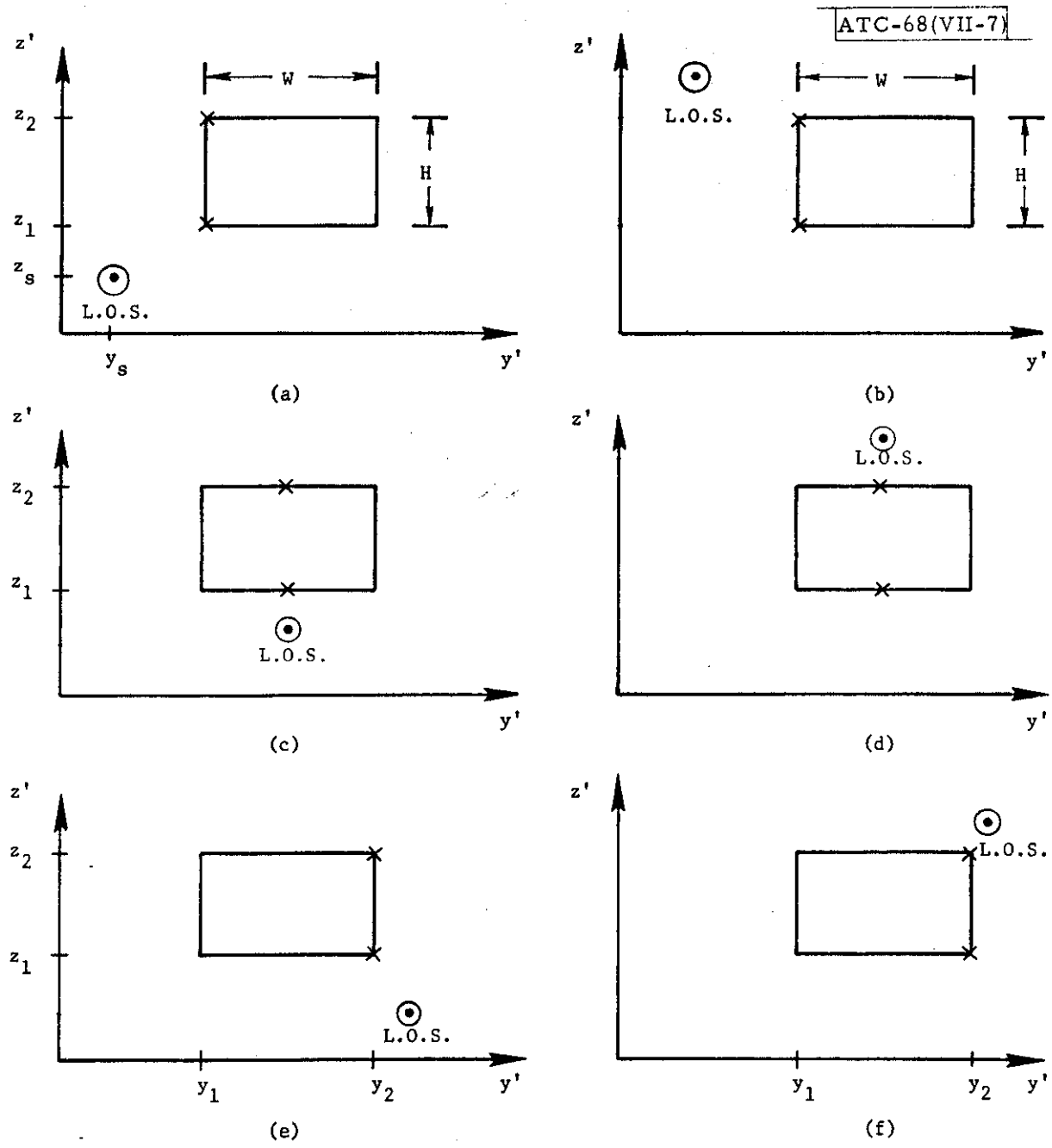

Fig. VII-7. Method for assigning directions to edge rays for DME and elevation systems, when H > R_f and the line of sight is outside the obstacle.

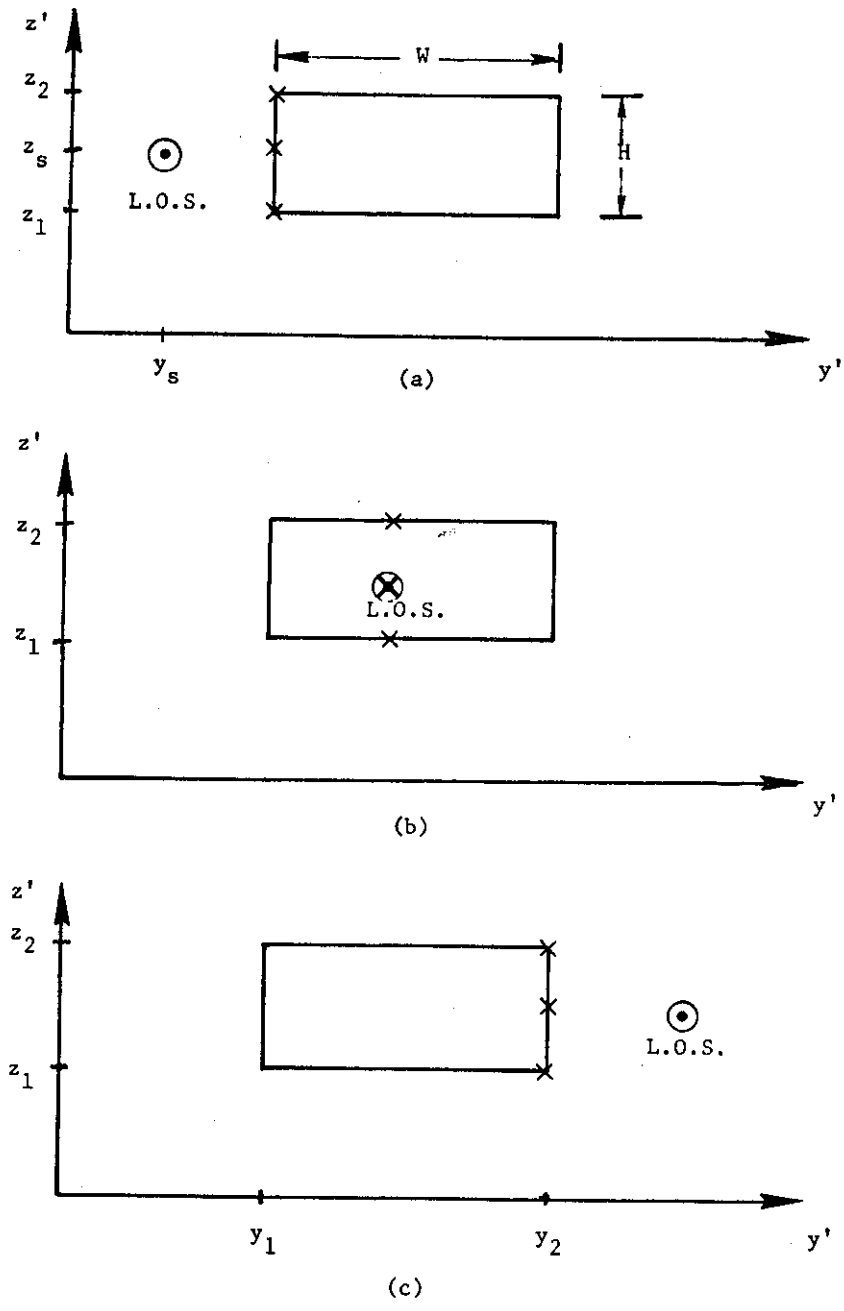

Fig. VII-8. Method for assigning directions to edge rays for DME and elevation systems, when H > R_f and the line of sight is inside the obstacle.

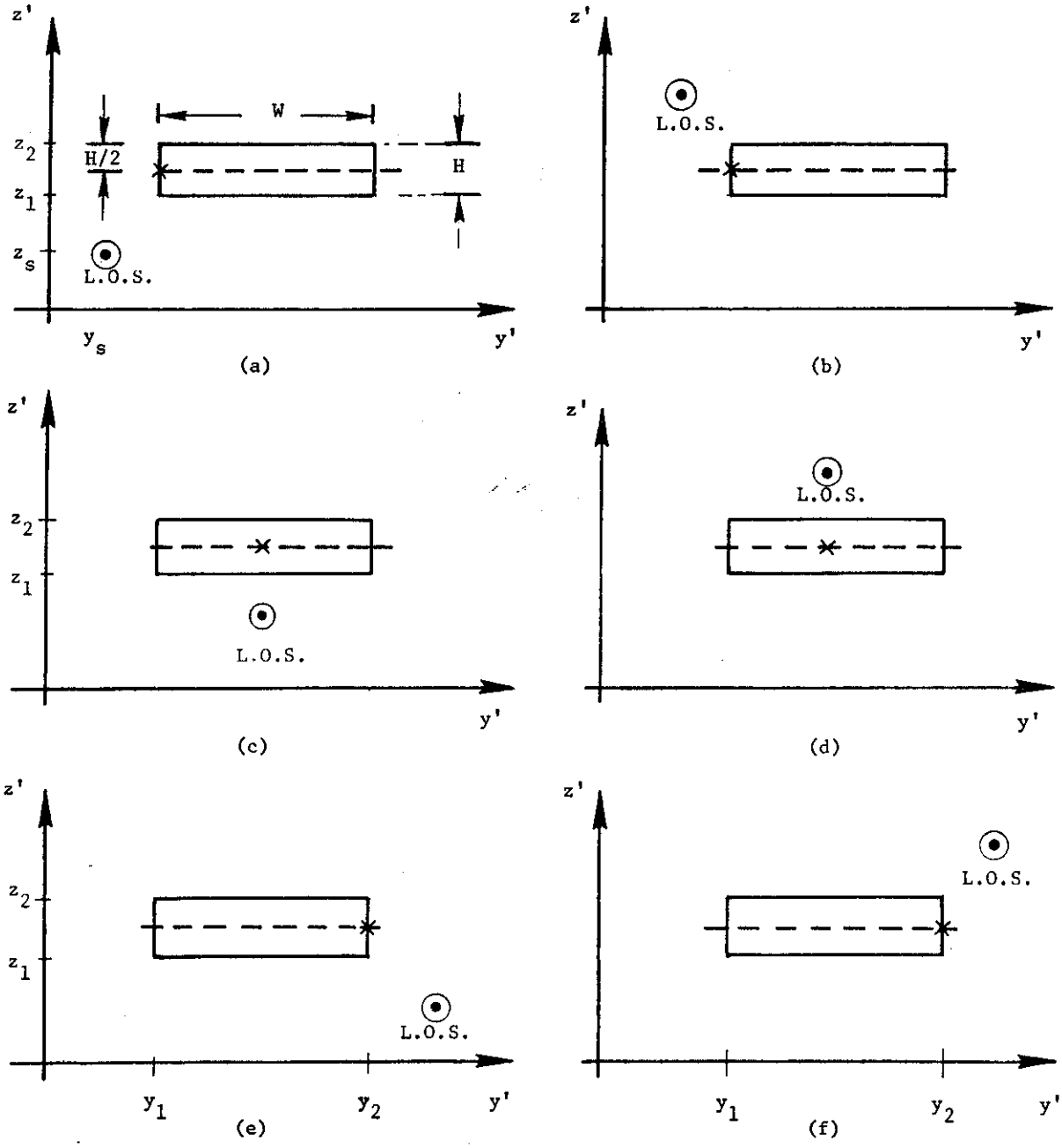

Fig. VII-9. Method for assigning directions to edge rays for DME and elevation systems, when $H > R_f$.

$$A_{Center} = \left(1 - \rho_Y \, \varepsilon^{j\pi/4}\right) \quad , \quad \text{(VII-22)}$$

Case C' ($H < R_f$)

$$A_{Center} = - \frac{j}{\sqrt{2}} \rho_Z \rho_Y \quad , \quad \text{(VII-23)}$$

$$A_{Direct} = 1 \quad , \quad \text{(VII-24)}$$

where all quantities have been defined previously in this section in the discussion of the azimuth system.

It has been pointed out that the shadowing effect due to aircraft and buildings can be determined by considering the received signal to consist of a number of edge rays. In general, there could be a large number of such edge rays, particularly if there is a large number of shadowing aircraft and buildings. The multipath parameters for these edge rays or multipath components, are computed as follows. The amplitude and phase of each multipath component are computed as the magnitude and argument of the complex amplitude of the edge ray, as given in Eqs. (VII-6) through (VII-13) for the azimuth system and Eqs. (VII-17) through (VII-24) for the DME and elevation systems. The time delay of the multipath component is taken as zero, while the planar directional angles and fractional Doppler frequency are computed as indicated previously in Eqs. (II-23) through (II-27).

The set of multipath components which have been determined previously in this section pertain to the X-O-R ray path. As pointed out previously in Section III D, it is possible to have sets of multipath components due to the

X-G-O-R, X-O-G-R, X-G-O-G-R ray paths. However, these latter two ray paths may be neglected, since the obstacle is usually located near the ground plane, and the aircraft receiver is usually at a reasonable altitude, so that the image receiver will be located well below the ground plane. In this case the line of sight from either the transmitter, or its image, will intersect the diffraction aperture plane at a point which is located at a distance from the obstacle which can be considered as a large multiple of the Fresnel zone size. Hence, the shadowing effect will be negligible for these ray paths.

However, the X-G-O-R ray path must be considered. A set of edge rays, or multipath components, is obtained for the X-G-O-R ray path in the same manner as for the X-O-R ray path, with the exception that the image transmitter location is employed in the computations instead of the actual transmitter position. In addition, each complex amplitude for the X-G-O-R ray path must be multiplied by the factor

$$\left(\frac{r_o}{r_I}\right) \cdot R_{eq} \cdot \rho_r \cdot \varepsilon^{-ik(r_I - r_o)} \quad ,$$

where r_o, r_I are the distances from the receiver to the transmitter and its image, respectively, R_{eq} is the Fresnel reflection coefficient for the ground surface and is given in Eqs. (II-10), (II-11), ρ_r is the attenuation factor due to the small-scale roughness of the ground, given in Eq. (II-7). The multipath parameters for this set of multipath components are computed as indicated previously for the X-O-R ray path.

When the subroutine is used, which computes the shadowing effect due to aircraft and buildings, then no use is made of the subprogram to compute the multipath parameters for the specular ground reflection which was described in Section II. The reason for this is that the former program contains a computation for obtaining a set of multipath components corresponding to a ground reflection. We mention finally that one should not use both this former subprogram, and the subroutine which computes the shadowing effect due to runway humps described in Section VI, in the MLS simulation program. That is, it is not possible to simultaneously determine the shadowing effect due to aircraft and buildings, and runway humps using the present computational procedures, since there appears to be no feasible manner in which the ground reflection can be treated when both of these situations are considered simultaneously.

C. Comparison of Results with Experimental Data

A comparison is now presented of some of the results obtained using the computer program which computes the shadowing effect due to aircraft and buildings, which was described in Section VII B, with some experimental shadowing data obtained at L-band, 1 GHz, C-band, 5 GHz, and K_u-band, 15 GHz. An idea can be obtained of the operation of this computer program from the flow chart shown in Fig. VII-10.

We now wish to compare the computational results with some experimental shadowing data due to the R.A.E.[19] taken at Farnborough runway, at both C-band,

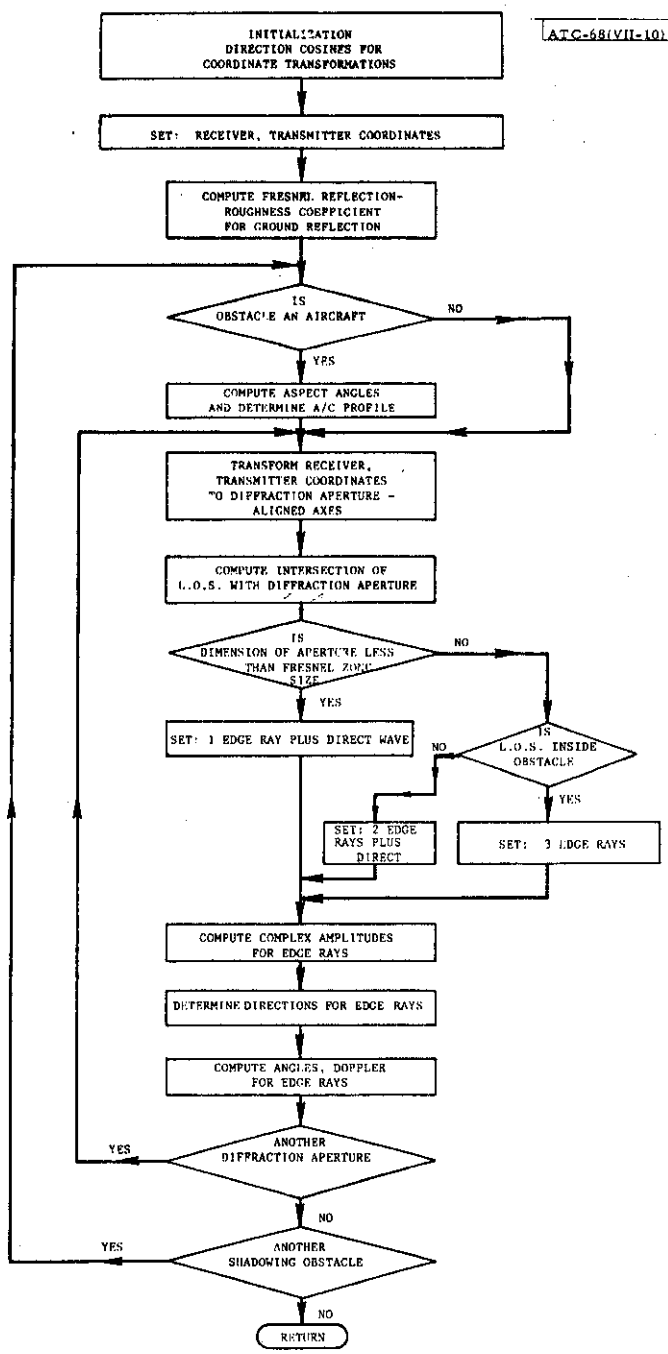

Fig. VII-10. Flow chart for program which computes shadowing effect due to aircraft and buildings.

5 GHz and K_u-band, 15 GHz. These data were obtained by towing an aircraft between the transmitter and receiver, and measuring the resultant shadowed signal at the receiver. The towed aircraft consisted of the Hastings type shown in Fig. VII-11. The plan view of the Farnborough runway configuration used in the measurements is shown in Fig. VII-12, as well as the experimental data and the corresponding computational results at C-band, 5 GHz, and K_u-band, 15 GHz. It is seen from Fig. VII-12 that there is reasonably good agreement between the computational and experimental results, at C-band and K_u-band, considering that simple rectangular shapes have been used to model the complex shapes depicted for the shadowing aircraft in Fig. VII-11. In these results the effect of the ground reflection has been neglected. That is, only the multipath components for the X-O-R, and not X-G-O-R, ray path have been considered. This corresponds to a situation where a shaped beam in elevation, cutting off sharply at the horizon, is employed at the transmitter, or possibly a case of a rough ground, so that a large attenuation of the ground reflection occurs.

We now compare the computational results with shadowing data obtained for the DABS system at L-band, 1 GHz. Once again, the effect of the ground reflection has been neglected. The DABS system employs a monopulse radar to obtain an estimate of the azimuth angle of an aircraft transponder. An indication is now given of the computations required to obtain this estimate of azimuth angle. The sum and difference channel signals of the monopulse radar are determined as follows

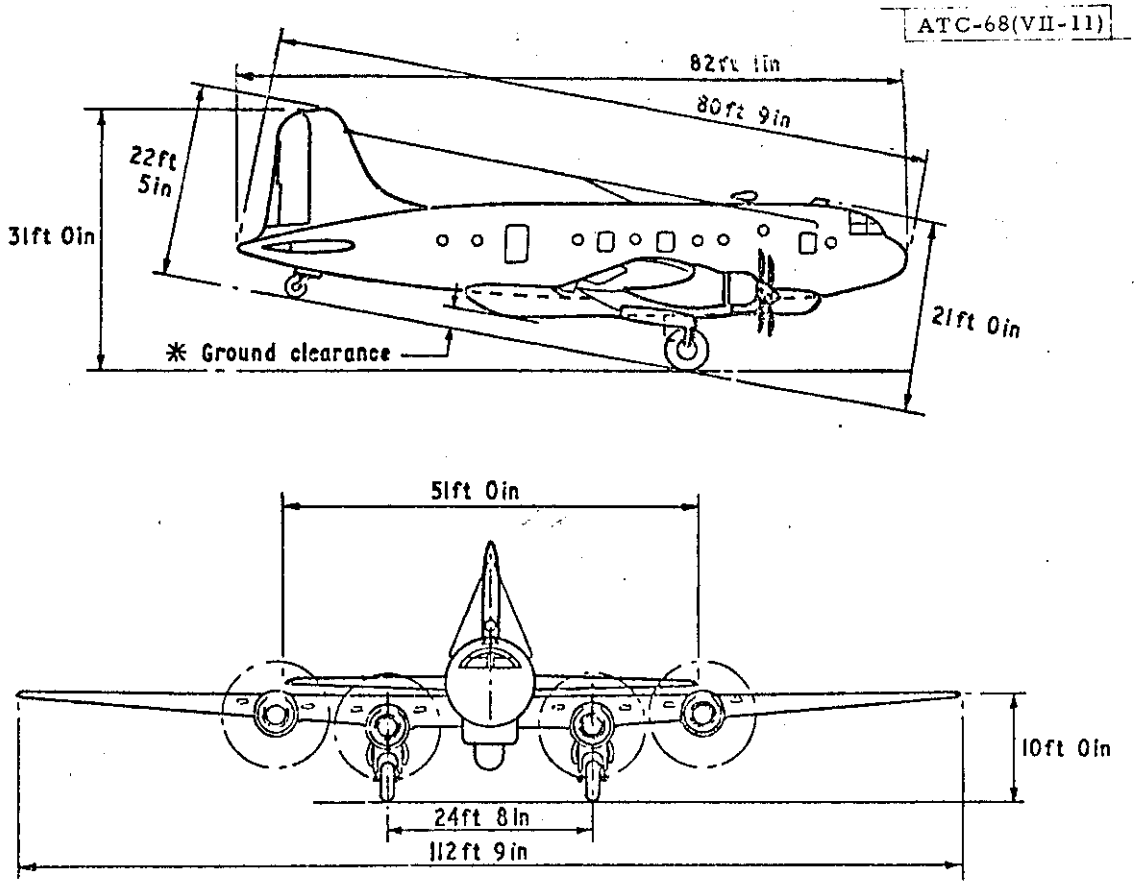

Fig. VII-11. Dimensions of Hastings aircraft used in towed aircraft tests.

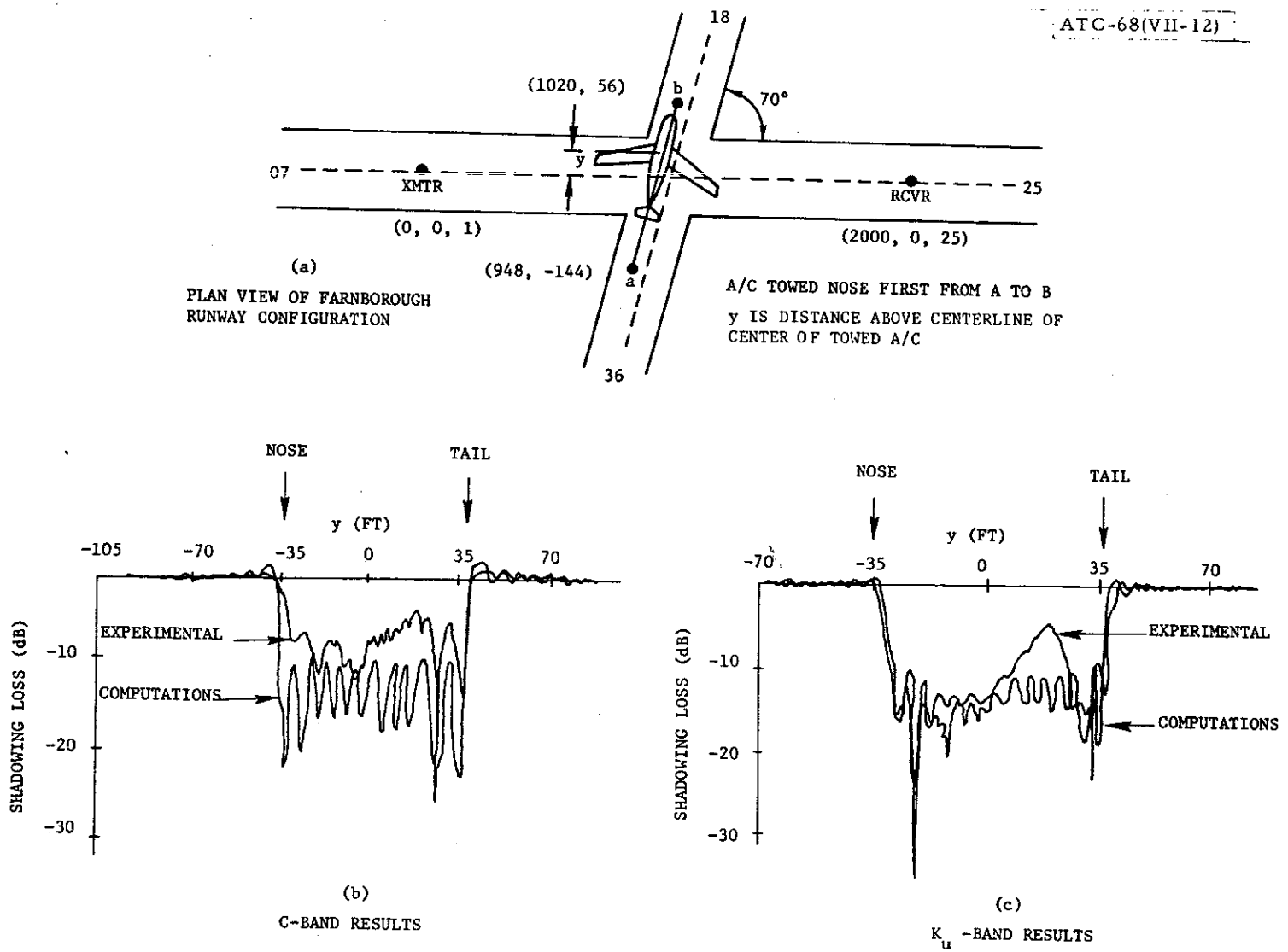

Fig. VII-12. Comparison of computational results with experimental K_u- and C-band signal shadowing loss for towed aircraft test at Farnborough (R.A.E.) runway.

$$\Sigma = \sum_{i=1}^{N} A_i \, G_{\Sigma}(\theta_i) \quad , \quad \text{(VII-25)}$$

$$\Delta = \sum_{i=1}^{N} A_i \, G_{\Delta}(\theta_i) \quad , \quad \text{(VII-26)}$$

where $G_{\Sigma}(\theta)$, $G_{\Delta}(\theta)$ are the DABS sum and difference antenna voltage patterns which can be approximated by

$$G_{\Sigma}(\theta) = \varepsilon^{-0.175\theta^2} \quad , \quad \text{(VII-27)}$$

$$G_{\Delta}(\theta) = \theta\varepsilon^{-0.103\theta^2} \quad , \quad \text{(VII-28)}$$

A_i is the complex amplitude of the i-th edge ray, N is the total number of edge rays and θ_i is the difference of planar azimuthal directional angles, in degrees, between the i-th edge ray and the boresight, or line of sight between transmitter and receiver. The monopulse processor forms the azimuth angle estimate defined as

$$\hat{\theta} = \text{Real} \{\Delta/\Sigma\} \quad , \quad \text{(VII-29)}$$

where $\hat{\theta}$ is in degrees, and is measured relative to the boresight direction.

It should be noted that we have used a form of reciprocity in the preceding computations. We have used the DABS ground station as the transmitter and the aircraft as the receiver in order to determine the edge rays. These edge rays would be determined in exactly the same manner if we had assumed the aircraft was transmitting and the DABS ground station was receiving, which is the actual situation.

The geometry employed in the measurement is depicted in Fig. VII-13, and corresponds to the situation where the obstacle consisted of the Hanscom smokestack shown in Fig. VII-14. In Fig. VII-13 there are also shown the DABSEF experimental data[23,24] for the monopulse angle error vs. the ground receiver-to-obstacle azimuth relative to the line of sight, as well as the corresponding computational results for $\hat{\theta}$ given in Eq. (VII-29). It is seen that there is excellent agreement between the two sets of data, providing additional justification for the edge ray model, which has been presented in Section VII B, for the purpose of computing the shadowing effect due to aircraft and buildings. This same comparison has been performed by Evans,[23] who also compares these results with an alternate, and somewhat more complicated, computational algorithm due to Spiridon.[24] Additional comparisons between the present model, Spiridon's model, and the DABSEF data will appear in a forthcoming report by Evans.[23]

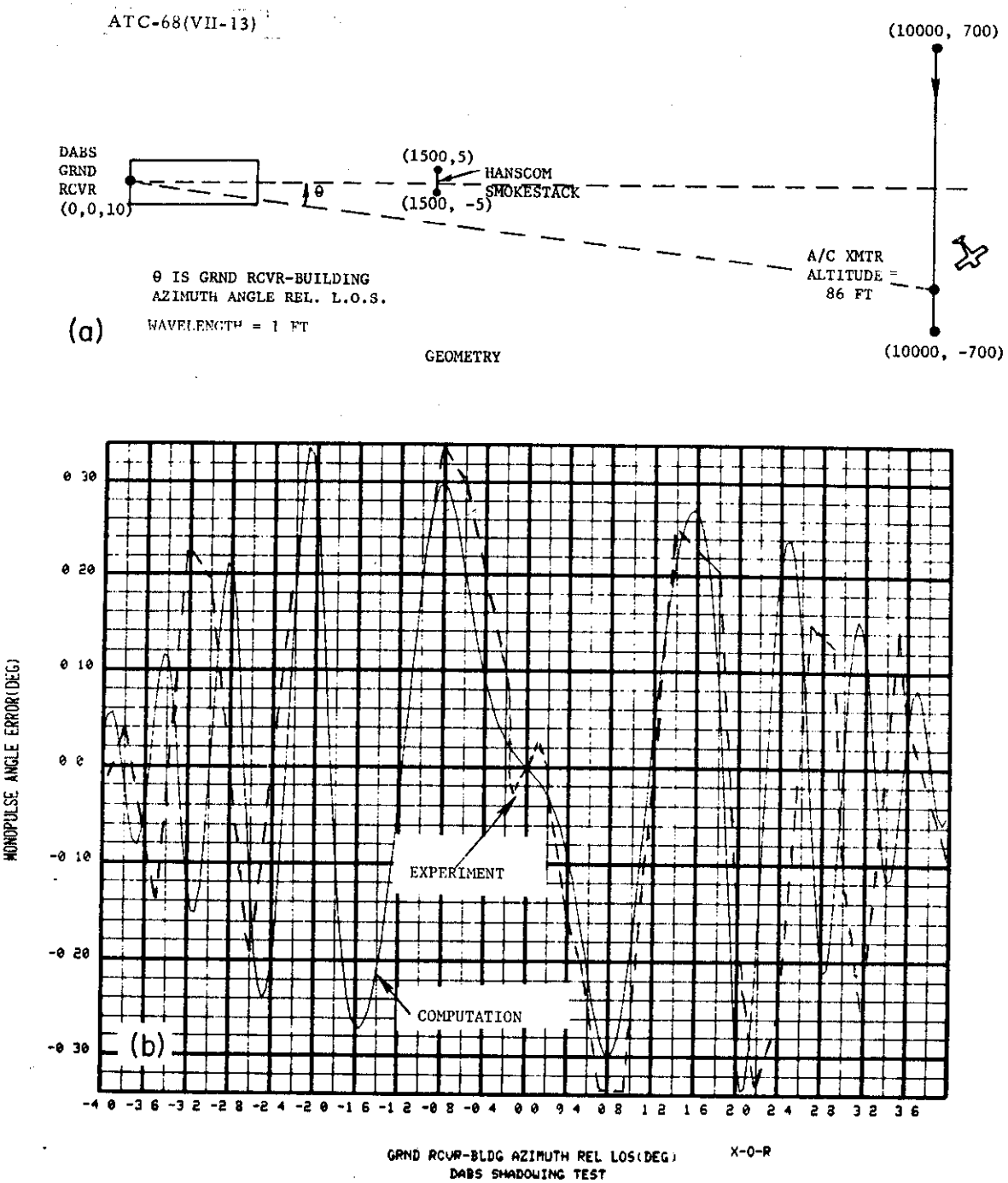

Fig. VII-13. Comparison of computational results with experimental DABS data for monopulse angle error due to shadowing by Hanscom smokestack.

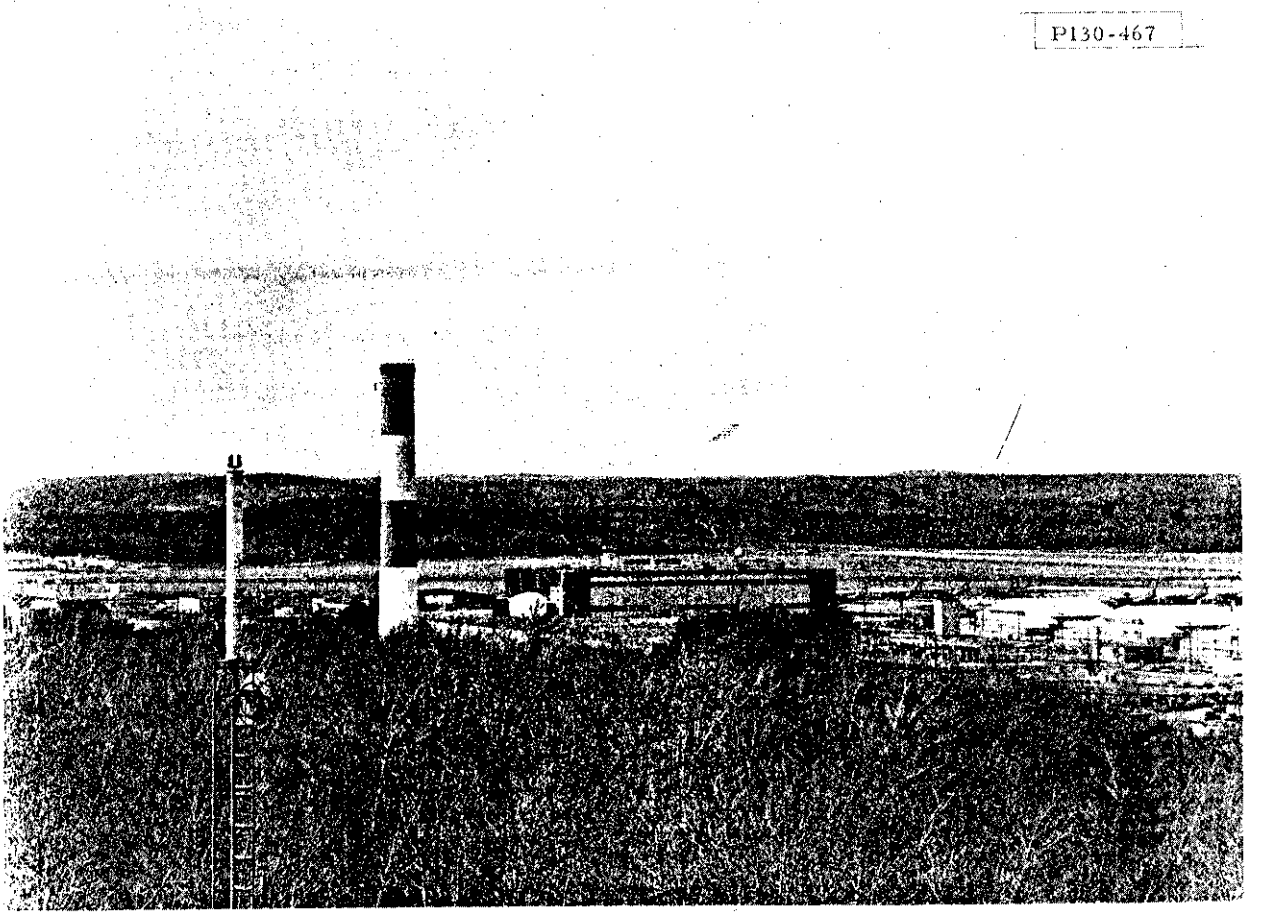

Fig. VII-14. View of the Hanscom smokestack as seen from DABSEF.

VIII. CONCLUSIONS

Models have been described for scattering and shadows from the more important obstacles to be encountered in an airport environment. These models have been used in a computer program to perform multipath modeling and simulation for MLS. Effort has been devoted to providing models which, while physically realistic, lead to analytical solutions which may be readily implemented with the computer.

In particular, the specular ground reflection has been considered, as well as scattering from buildings and aircraft. The diffusely scattered component from the ground has been obtained in a comparatively simple manner by assuming that the ground can be considered as a very rough surface. The shadowing effects due to runway humps, and aircraft, buildings approaching the line of sight, have also been considered. It is expected that these obstacles are the ones which will have the major effect on the performance of MLS in a multipath propagation environment.

Computer validation data have been presented for all of the multipath computations which have been described. In addition, comparisons have been made of the computational results with experimental field data. In all cases, these data indicate that the computational procedures provide reasonable models for the scattering and diffraction problems considered. For example, in the case of scattering from buildings and aircraft, the computations were compared with the results of measurements and geometric diffraction theory.[8] In all cases, there was reasonably good agreement between the two sets of data. In addition, the present computational procedures require much less computer

running time, for performing the calculations, than methods based on the geometric diffraction theory. This fact makes them more appropriate for use in the MLS computer simulation program.

These multipath computer programs have been written using the Fortran programming language,[25] with structured programming methods, such as Iftran, employed whenever this was feasible. The total amount of storage required by these multipath computer programs, including an executive program which calls all of these subroutines, is approximately 300 k bytes of IBM 370/168 machine memory. The computer running times for these subroutines, for each flight evaluation point and for each obstacle, using the IBM 370/168 computer are given in the following table:

Computer Program	Computer Time Required Per Flight Evaluation Point And Per Obstacle (Seconds)
Specular ground reflection	0.1
Specular ground reflection (with speedup)	0.001
Scattering from building	0.002
Scattering from aircraft	0.002
Diffuse ground scattering	0.1
Runway hump shadowing	0.001
Aircraft, building shadowing	0.002

As an example, a multipath computation run involving a typical airport environment, with about ten aircraft and building scattering and shadowing obstacles, requires about 10 to 20 minutes of IBM 370/168 computer time for a flight path consisting of about 1000 points. These computer times indicate the utility of the computational algorithms, which have been developed for multipath parameter determination, for the purpose of performing multipath modeling and simulation for MLS.

APPENDIX A

METHOD FOR COMPUTING FRESNEL REFLECTION COEFFICIENT FOR REFLECTION FROM TILTED PLANAR SURFACE

In this section we present the details of the computations which have been used to determine the Fresnel reflection coefficient, R_{eq}, for a near-specular reflection from a tilted planar surface. The geometry for this problem is shown in Fig. A-1. The formulae for R_{eq} were given in Section II, Eqs. (II-10) and (II-11) as

$$R_{eq} = R_V(\theta_t) \cos \alpha_1 \cos \alpha_2 + R_h(\theta_t) \sin \alpha_1 \sin \alpha_2 \quad , \quad \text{(vertical polarization)} \tag{A-1}$$

$$R_{eq} = R_V(\theta_t) \sin \alpha_1 \sin \alpha_2 + R_h(\theta_t) \cos \alpha_1 \cos \alpha_2 \quad \text{(horizontal polarization)} \tag{A-2}$$

where $R_V(\theta_t)$, $R_h(\theta_t)$, are the Fresnel reflection coefficients for vertical and horizontal polarization and are given by, cf. Eqs. (II-8) and (II-9),

$$R_V(\theta_t) = \frac{\varepsilon_r \cos \theta_t - \sqrt{\varepsilon_r - \sin^2\theta_t}}{\varepsilon_r \cos \theta_t + \sqrt{\varepsilon_r - \sin^2\theta_t}} \quad , \tag{A-3}$$

$$R_h(\theta_t) = \frac{\cos \theta_t - \sqrt{\varepsilon_r - \sin^2\theta_t}}{\cos \theta_t + \sqrt{\varepsilon_r - \sin^2\theta_t}} \quad , \tag{A-4}$$

and ε_r is the relative complex dielectric constant for the planar facet containing the point P, cf. Fig. A-1, and is given in Eq. (II-1).

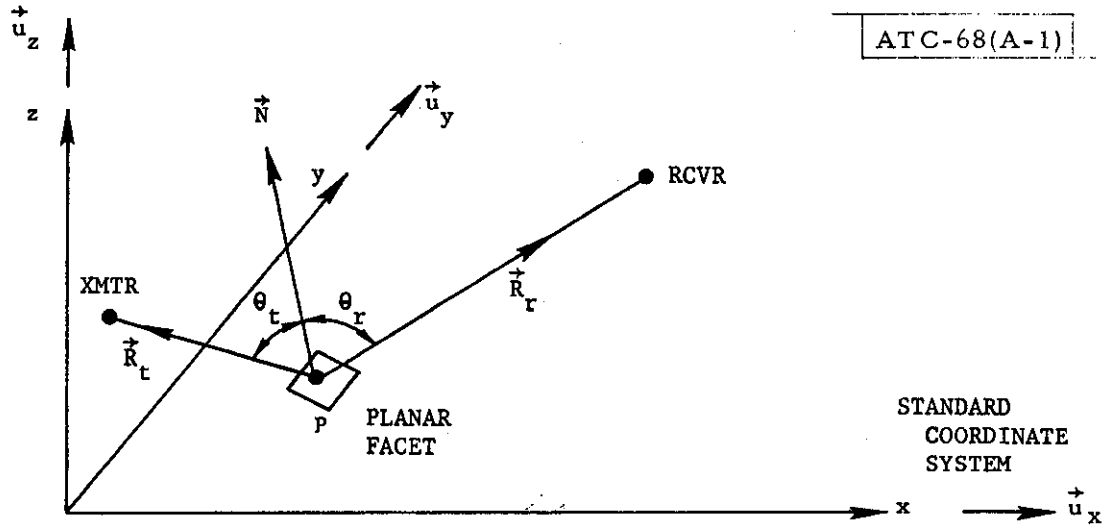

P IS ARBITRARY POINT IN PLANAR FACET, CLOSE TO SPECULAR POINT

$\vec{N}$ IS UNIT VECTOR NORMAL TO PLANAR FACET

$\vec{u}_x$, $\vec{u}_y$, $\vec{u}_z$ ARE UNIT VECTORS IN x, y, z DIRECTIONS, RESPECTIVELY

$$\vec{R}_t = R_{tx}\,\vec{u}_x + R_{ty}\,\vec{u}_y + R_{tz}\,\vec{u}_z$$

$$\vec{R}_r = R_{rx}\,\vec{u}_x + R_{ry}\,\vec{u}_y + R_{rz}\,\vec{u}_z$$

$$\vec{N} = N_x\,\vec{u}_x + N_y\,\vec{u}_y + N_z\,\vec{u}_z$$

Fig. A-1. Geometry employed in computing Fresnel reflection coefficient for a near-specular reflection from a tilted planar surface.

In order to determine the Fresnel coefficients $R_V(\theta_t)$, $R_h(\theta_t)$, it is necessary to compute the incidence angle, θ_t. We see from Fig. A-1 that θ_t is determined from the following vector dot product

$$\cos \theta_t = \vec{R}_t \cdot \vec{N}/R_t \quad , \tag{A-5}$$

where $R_t = |\vec{R}_t|$. In addition, we have

$$\cos \theta_r = \vec{R}_r \cdot \vec{N}/R_r \quad , \tag{A-6}$$

where $R_r = |\vec{R}_r|$.

The angle α_1 is equal to the angle between the plane determined by the vectors $(\vec{R}_t, \vec{u}_z)$, and the plane determined by the vectors $(\vec{R}_t, \vec{N})$. In addition, the angle α_2 is equal to the angle between the plane determined by the vectors $(\vec{R}_r, \vec{u}_z)$ and the plane determined by the vectors $(\vec{R}_t, \vec{N})$. Thus, we have

$$\cos \alpha_1 = \frac{(\vec{R}_t \times \vec{u}_z)}{(R_{tx}^2 + R_{ty}^2)^{1/2}} \cdot \frac{(\vec{R}_t \times \vec{N})}{R_t \sin \theta_t} \tag{A-7}$$

$$\cos \alpha_2 = \frac{(\vec{u}_z \times \vec{R}_r)}{(R_{rx}^2 + R_{ry}^2)^{1/2}} \cdot \frac{(\vec{R}_t \times \vec{N})}{R_t \sin \theta_t} \tag{A-8}$$

In order to simplify the Eqs. (A-7) and (A-8), we require the following vector identity involving the vectors a, b, c, d,

$$(a \times b) \cdot (c \times d) = \begin{vmatrix} (a \cdot c) & (b \cdot c) \\ (a \cdot d) & (b \cdot d) \end{vmatrix} \quad . \tag{A-9}$$

Using the vector identity in Eq. (A-9), we obtain

$$(\vec{R}_t \times \vec{u}_z) \cdot (\vec{R}_t \times \vec{N}) = (\vec{R}_t \cdot \vec{R}_t)(\vec{u}_z \cdot \vec{N}) - (\vec{R}_t \cdot \vec{N})(\vec{u}_z \cdot \vec{R}_t)$$

$$= R_t^2 N_z - R_{tz} R_t \cos \theta_t \quad , \tag{A-10}$$

$$(\vec{u}_z \times \vec{R}_r) \cdot (\vec{R}_t \times \vec{N}) = (\vec{u}_z \cdot \vec{R}_t)(\vec{R}_r \cdot \vec{N}) - (\vec{u}_z \cdot \vec{N})(\vec{R}_r \cdot \vec{R}_t)$$

$$= R_{tz} R_r \cos \theta_r - N_z(\vec{R}_t \cdot \vec{R}_r) \; . \tag{A-11}$$

If we use Eqs. (A-10) and (A-11) in (A-7) and (A-8), respectively, we get

$$\cos \alpha_1 = \frac{R_t N_z - R_{tz} \cos \theta_t}{(R_{tx}^2 + R_{ty}^2)^{1/2} \sin \theta_t} \quad , \tag{A-12}$$

$$\cos \alpha_2 = \frac{R_{tz} R_r \cos \theta_r - N_z(\vec{R}_t \cdot \vec{R}_r)}{(R_{rx}^2 + R_{ry}^2)^{1/2} R_t \sin \theta_t} \; . \tag{A-13}$$

We can determine sin α_1 and sin α_2 from Eqs. (A-12) and (A-13), respectively, so that using these along with $R_v(\theta_t)$, $R_h(\theta_t)$, as determined from Eqs. (A-3) and (A-4), respectively, we can compute R_{eq} from Eqs. (A-1) and (A-2), depending on whether the transmitted signal is vertically, or horizontally, polarized, respectively.

APPENDIX B

METHOD FOR COMPUTING POSITION OF SPECULAR POINT FOR REFLECTION FROM TILTED GROUND FACET

A discussion is now presented of the technique employed to compute the position of the specular for reflection from a slightly tilted ground facet, as discussed in Section II. The geometry for this problem is depicted in Fig. B-1. The solution for the coordinates of this specular point is best obtained by means of a transformation of coordinates. In order to transform from the standard coordinate system, i.e., x, y, z axes shown in Fig. B-1, to the primed system, x', y', z' axes, we must have, using matrix notation

$$\begin{bmatrix} x' \\ y' \\ z' \end{bmatrix} = \begin{bmatrix} d_{xx'} & d_{yx'} & d_{zx'} \\ d_{xy'} & d_{yy'} & d_{zy'} \\ d_{xz'} & d_{yz'} & d_{zz'} \end{bmatrix} \begin{bmatrix} x-x_o \\ y-y_o \\ z-z_o \end{bmatrix} , \qquad \text{(B-1)}$$

where $d_{xx'}$ is the cosine of the angle between the x, x' axes, with a similar notation for the other eight coefficients given in the matrix in Eq. (B-1). In a similar manner, to transform from the primed to the unprimed coordinates we have

$$\begin{bmatrix} x \\ y \\ z \end{bmatrix} = \begin{bmatrix} d_{xx'} & d_{xy'} & d_{xz'} \\ d_{yx'} & d_{yy'} & d_{yz'} \\ d_{zx'} & d_{zy'} & d_{zz'} \end{bmatrix} \begin{bmatrix} x' \\ y' \\ z' \end{bmatrix} + \begin{bmatrix} x_o \\ y_o \\ z_o \end{bmatrix} . \qquad \text{(B-2)}$$

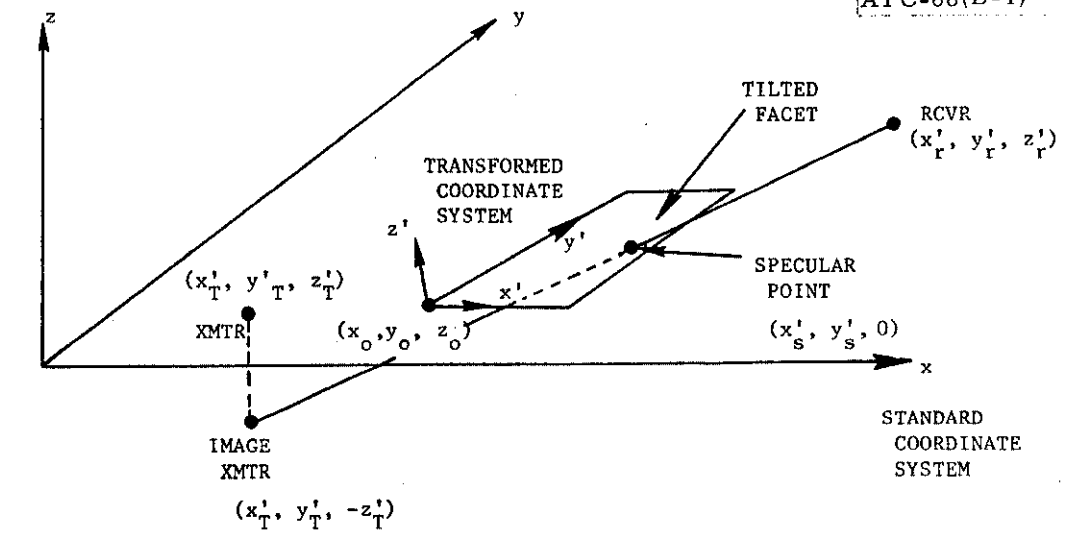

(a)

RECTANGULAR SURFACE ELEMENT

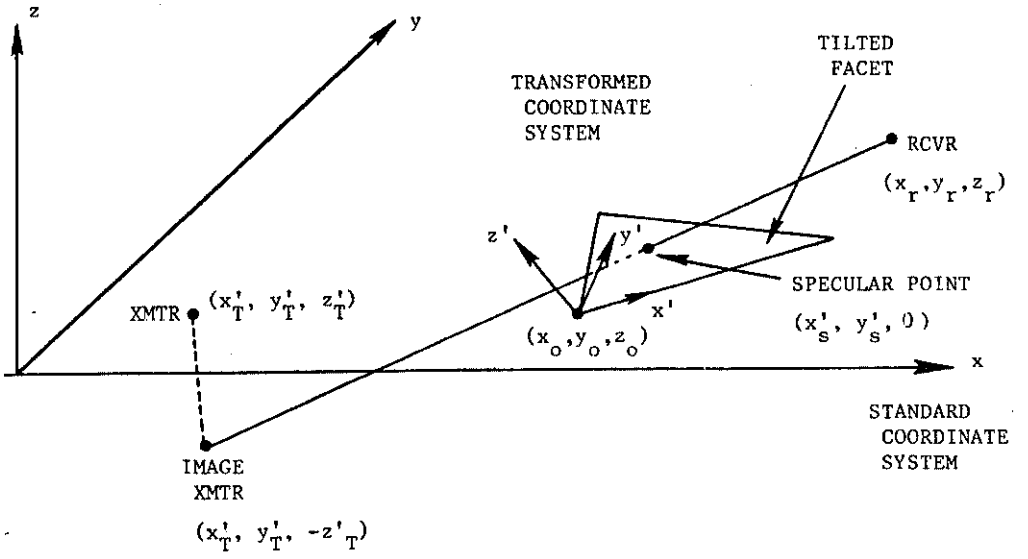

(b)

TRIANGULAR SURFACE ELEMENT

Fig. B-1. Configuration used in determining position of specular point for reflection from tilted ground facet.

The coordinates of the transmitter are (x'_T, y'_T, z'_T), so that the coordinates of the image transmitter are $(x'_T, y'_T, -z'_T)$.

Since the image transmitter, specular point, and receiver are collinear points, we obtain

$$\begin{bmatrix} x_s' \\ y_s' \\ z_s' \end{bmatrix} = \begin{bmatrix} x_T' \\ y_T' \\ -z_T' \end{bmatrix} + C \begin{bmatrix} x_r' - x_T' \\ y_r' - y_T' \\ z_r' + z_T' \end{bmatrix} . \qquad \text{(B-3)}$$

The constant C is determined by the condition that $z_s' = 0$, hence

$$C = \frac{z_T'}{z_r' + z_T'} . \qquad \text{(B-4)}$$

Thus, the coordinates of the specular point are given by

$$\begin{bmatrix} x_s' \\ y_s' \\ z_s' \end{bmatrix} = \begin{bmatrix} x_T' + C(x_r' - x_T') \\ y_T' + C(y_r' - y_T') \\ 0 \end{bmatrix} , \qquad \text{(B-5)}$$

where C is given by Eq. (B-4). These coordinates can be transformed back to the standard system using Eq. (B-2).

The preceding analysis is based on an assumption that the transmitter and receiver both lie above the surface element, i.e., $z_T' > 0$, $z_r' > 0$. A check is made by the program to determine if this condition is true. If this

condition is not true then the specular point is determined relative to the infinite ground, or xy - plane, cf. Fig. B-1. However, in performing the numerical integration, there is a check made to determine if the receiver is shadowed by this surface element from the transmitter, so that in this event its contribution to the sum is set to zero.

APPENDIX C

METHOD USED TO DETERMINE WHETHER A POINT LIES INSIDE A RECTANGLE OR TRIANGLE

We now present the method used to determine whether a point, whose coordinates are (x, y, z), when projected onto the ground, or xy-plane, so that its coordinates are (x, y, 0), lies inside of the boundaries defined in this ground plane by a surface element. This technique is essential in performing the numerical integration, over the appropriate rectangular and triangular surface elements, of the Fresnel-Kirchoff diffraction integral discussed in Section II. The geometry for this problem is shown in Fig. C-1, which depicts the boundaries of the triangular and rectangular surface elements defined in the xy-plane.

We begin the discussion by first considering the situation where we have a triangular surface element. For this situation we must distinguish between the two cases depicted in Fig. C-1a, b. In case A, the points P_1, P_2, P_3 form a clockwise set of points, while in case B they form a counterclockwise set of points. These two cases contain all the possible configurations which need be considered. The following form a necessary and sufficient set of conditions which must be satisfied in order that a point P lie inside of a triangle:

$$C_{AB} (\vec{u}_2 \times \vec{u}_1) \cdot \vec{u}_z \geq 0 \quad , \qquad \text{(C-1)}$$

$$C_{AB} (\vec{u}_3 \times \vec{u}_2) \cdot \vec{u}_z \geq 0 \quad , \qquad \text{(C-2)}$$

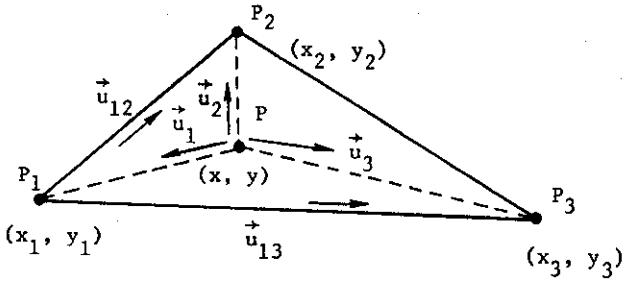

(a)

CASE A-TRIANGULAR SURFACE ELEMENT

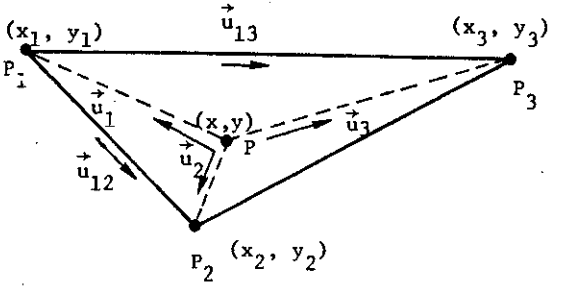

(b)

CASE B-TRIANGULAR SURFACE ELEMENT

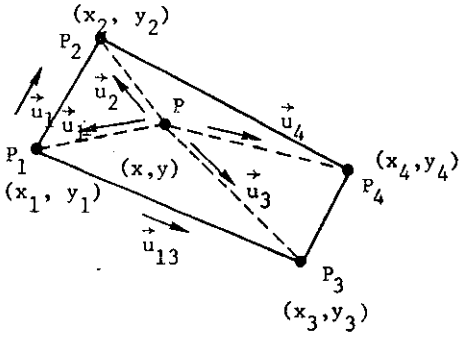

(c)

CASE A-RECTANGULAR SURFACE ELEMENT

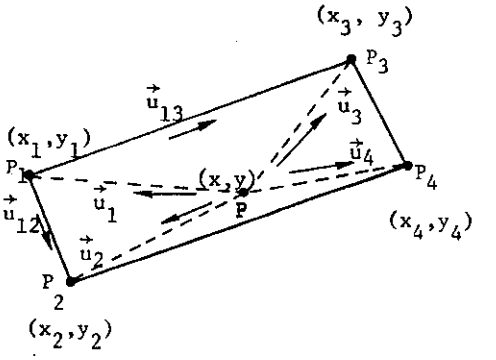

(d)

CASE B-RECTANGULAR SURFACE ELEMENT

$\vec{u}_1$, $\vec{u}_2$, $\vec{u}_3$, $\vec{u}_4$, $\vec{u}_{12}$, $\vec{u}_{13}$ ARE UNIT VECTORS IN INDICATED DIRECTIONS

Fig. C-1. Geometry used for determining whether a point lies inside a triangle or rectangle.

$$C_{AB}\ (\vec{u}_1 \times \vec{u}_3) \cdot \vec{u}_z \geq 0 \quad , \tag{C-3}$$

where $\vec{u}_z$ is the unit vector in the direction of the z-axis, cf. Fig. II-1, and would point up out of the paper relative to the polygons shown in Fig. C-1, and

$$C_{AB} = (\vec{u}_{13} \times \vec{u}_{12}) \cdot \vec{u}_z \quad . \tag{C-4}$$

It is easily seen from Eq. (C-4) and Fig. C-1 that $C_{ab} = +1$ for case A and $C_{AB} = -1$ for case B.

In a similar manner we have the following set of necessary and sufficient conditions which must be satisfied in order that a point P lie inside of a rectangle:

$$C_{AB}\ (\vec{u}_2 \times \vec{u}_1) \cdot \vec{u}_z \geq 0 \quad , \tag{C-5}$$

$$C_{AB}\ (\vec{u}_4 \times \vec{u}_2) \cdot \vec{u}_z \geq 0 \quad , \tag{C-6}$$

$$C_{AB}\ (\vec{u}_3 \times \vec{u}_4) \cdot \vec{u}_z \geq 0 \quad , \tag{C-7}$$

$$C_{AB}\ (\vec{u}_1 \times \vec{u}_3) \cdot \vec{u}_z \geq 0 \quad . \tag{C-8}$$

It should be noted in Figs. C-1c, d that it is known that $x_1 \leq x_2 \leq x_3 \leq x_4$ since this is the manner in which the rectangle must be specified in the computer program. Hence, the cases A and B represent all the possible configurations for rectangles.

In order to show the sufficiency of these conditions, it is required to assume that the conditions are true, that the corresponding point lies outside the polygon, and that this leads to a contradiction. In order to show the necessity of these conditions, it is required to assume that the point lies inside the polygon, that the corresponding conditions are not true, and that this leads to a contradiction.

APPENDIX D

DIFFRACTION BY CIRCULAR AND SQUARE APERTURES

We now consider the problem of diffraction by either a circular or square aperture in an opaque screen, which was discussed in Section II. The geometry for this problem is depicted in Fig. D-1. Using the Fresnel-Kirchoff diffraction integral, cf. Sommerfeld,[5] p. 202, the complex amplitude of the diffracted signal at the receiver, relative to the signal at the receiver with no screen present, can be written as

$$\rho_c = j \frac{r_{10} + r_{20}}{\lambda} \iint \frac{\varepsilon^{-jk(R_t + R_r - r_{10} - r_{20})}}{R_t R_r} \, dS \quad . \tag{D-1}$$

The Fresnel approximations for R_t, R_r are

$$R_t = (r_{10}^2 + r^2)^{1/2} \cong r_{10} + \tfrac{1}{2} \frac{r^2}{r_{10}} \quad , \tag{D-2}$$

$$R_r = (r_{20}^2 + r^2)^{1/2} \cong r_{20} + \tfrac{1}{2} \frac{r^2}{r_{20}} \quad , \tag{D-3}$$

so that using the fact that $dS = rdrd\theta$ we can write Eq. (D-1) as

$$\rho_c = \frac{j}{\lambda} \left(\frac{1}{r_{10}} + \frac{1}{r_{20}} \right) \int_0^a \int_0^{2\pi} \varepsilon^{-j\frac{k}{2}\left(\frac{1}{r_{10}} + \frac{1}{r_{20}} \right) r^2} \, rdrd\theta$$

$$= \frac{2\pi j}{R_f^2} \int_0^a \varepsilon^{-j\pi \left(\frac{r}{R_f}\right)^2} rdr \quad , \tag{D-4}$$

where R_f is the Fresnel zone size given by

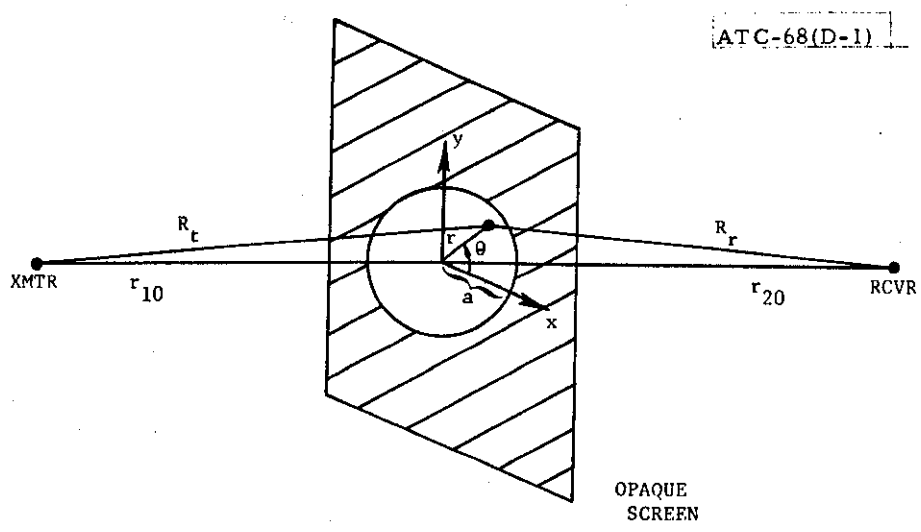

(a)
CIRCULAR APERTURE

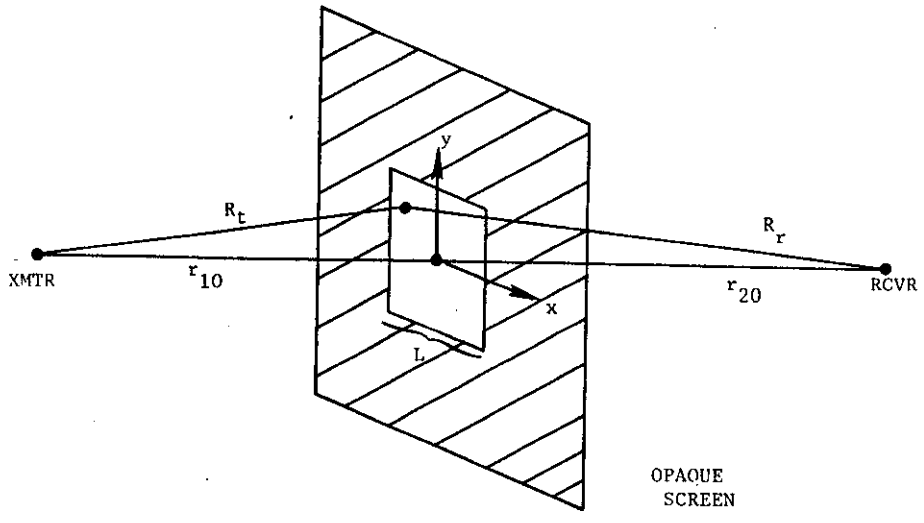

(b)
SQUARE APERTURE

Fig. D-1. Geometry employed for determining diffraction by circular and square apertures.

$$R_f = \left(\lambda \frac{r_{10} r_{20}}{r_{10} + r_{20}} \right)^{1/2} \quad . \tag{D-5}$$

If we let $\mu = -j\pi \left(\frac{r}{R_f}\right)^2$, so that $d\mu = -j2\pi r dr / R_f^2$, we can write Eq. (D-4) as

$$\rho_c = -\int_0^{-j\pi N} \varepsilon^{\mu} \, d\mu = 1 - \varepsilon^{-j\pi N} \quad , \tag{D-6}$$

where N is the number of Fresnel zones given by

$$N = a^2 / R_f^2 \quad . \tag{D-7}$$

It is easily seen that by using some trigonometric manipulations that the expression in Eq. (D-6) can be rewritten as

$$\rho_c = 2 \left| \sin \left(\frac{\pi N}{2} \right) \right| \varepsilon^{j\frac{\pi}{2}(1 - N + 2N')} \quad , \tag{D-8}$$

where N' is the largest integer less than or equal to N/2.

We now consider diffraction by a square aperture of side L, so that

$$\rho_s = \frac{j}{R_f^2} \int_{\frac{-L}{2}}^{L/2} \int_{\frac{-L}{2}}^{L/2} \varepsilon^{-j\pi \left(\frac{x^2 + y^2}{R_f^2} \right)} \, dxdy$$

$$= j \left[2 \int_0^{L/2} \varepsilon^{-j\pi x^2 / R_f^2} \, \frac{dx}{R_f} \right]^2 \quad . \tag{D-9}$$

If we let $v = \sqrt{2}\, x / R_f$, so that $dv = \sqrt{2} dx / R_f$, we can write Eq. (D-9) as

$$\rho_s = 2jF^2 \left(L / \sqrt{2} R_f \right) \quad , \tag{D-10}$$

where $F(x)$ is the Fresnel integral defined previously in Eq. (II-34). The distance L is chosen so that the area of the square is equal to that of the circle, so that $L^2 = \pi a^2$, and $N = a^2/R_f^2 = L^2/\pi R_f^2$. Hence, we can write Eq. (D-10) as

$$\rho_s = 2\, jF^2\left(\sqrt{\frac{\pi N}{2}}\right) \tag{D-11}$$

APPENDIX E

DETERMINATION OF POSITION OF SPECULAR POINT FOR BUILDING REFLECTION

We now present the method for computing the position of the specular point for reflection from a building, as discussed in Section III. The geometry for this problem is illustrated in Fig. E-1. The solution for the coordinates of the specular point is best obtained by means of a transformation of coordinates. In order to transform from the standard coordinate system, i.e., x, y, z, axes shown in Fig. E-1, to the primed system, x', y', z' axes, we must employ two successive rotations of coordinate systems about the z, x'-axes, by angles θ, θ_T, respectively, so that using matrix notation

$$\begin{bmatrix} x' \\ y' \\ z' \end{bmatrix} = \begin{bmatrix} 1 & 0 & 0 \\ 0 & \cos\theta_T & -\sin\theta_T \\ 0 & \sin\theta_T & \cos\theta_T \end{bmatrix} \begin{bmatrix} \cos\theta & \sin\theta & 0 \\ -\sin\theta & \cos\theta & 0 \\ 0 & 0 & 1 \end{bmatrix} \begin{bmatrix} x-x_L \\ y-y_L \\ z \end{bmatrix} \quad \text{(E-1)}$$

In a similar manner, to transform from the primed to the unprimed coordinates, we have

$$\begin{bmatrix} x \\ y \\ z \end{bmatrix} = \begin{bmatrix} 1 & 0 & 0 \\ 0 & \cos\theta_T & \sin\theta_T \\ 0 & -\sin\theta_T & \cos\theta_T \end{bmatrix} \begin{bmatrix} \cos\theta & -\sin\theta & 0 \\ \sin\theta & \cos\theta & 0 \\ 0 & 0 & 1 \end{bmatrix} \begin{bmatrix} x' \\ y' \\ z' \end{bmatrix} + \begin{bmatrix} x_L \\ y_L \\ 0 \end{bmatrix}. \quad \text{(E-2)}$$

An initial check is made by the program to determine if a reflection is feasible. The condition for this is

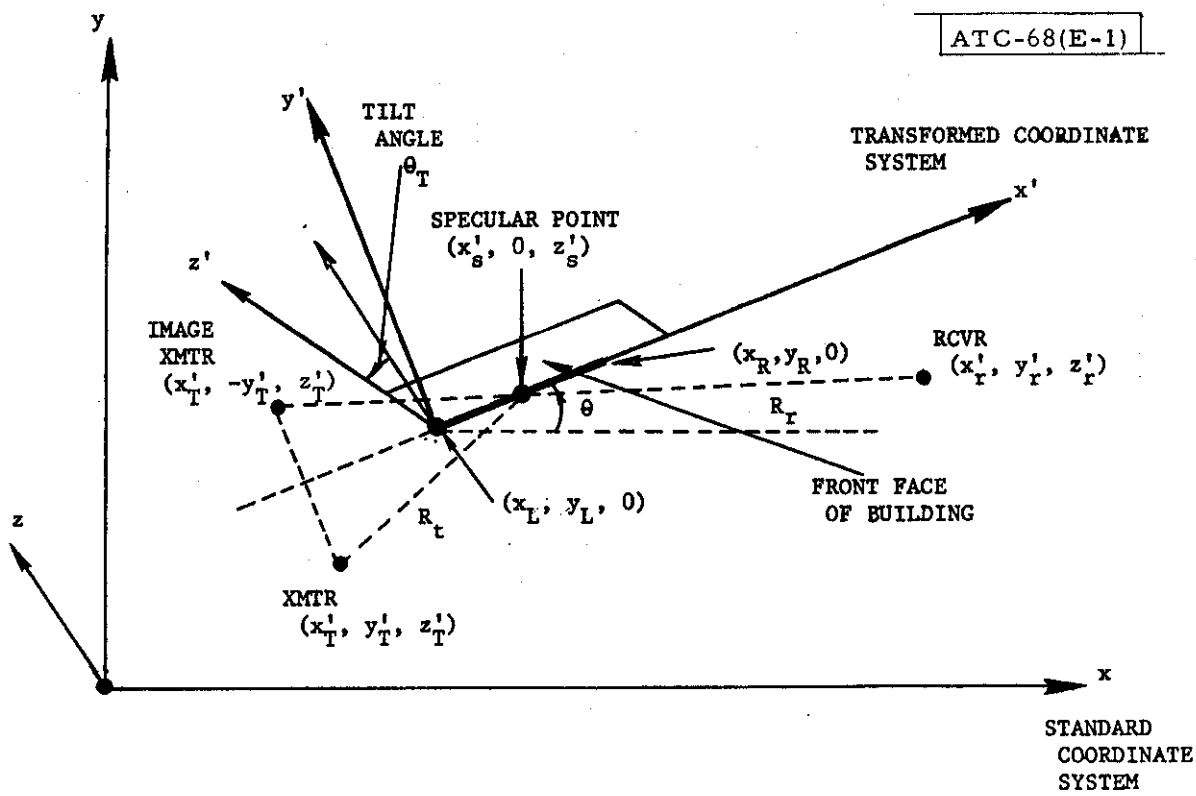

BUILDING SPECIFIED BY (x_R, y_R), (x_L, y_L), H_B, H_{bottom}

Fig. E-1. Configuration used in determining position of specular point for reflection from building.

$$\text{sign}\{y_T'\} = \text{sign}\{y_r'\} \quad , \tag{E-3}$$

where y_T' and y_r' are the y'-coordinates of the transmitter and receiver, respectively, in the transformed coordinate system, as indicated by the transformation in Eq. (E-1). The coordinates of the transmitter are (x_T', y_T', z_T'), so that the coordinates of the image transmitter are $(x_T', -y_T', z_T')$. Since the image transmitter, specular point, and receiver are collinear points, we get

$$\begin{bmatrix} x_s' \\ y_s' \\ z_s' \end{bmatrix} = \begin{bmatrix} x_T' \\ -y_T' \\ z_T' \end{bmatrix} + C \begin{bmatrix} x_r' - x_T' \\ y_r' + y_T' \\ z_r' - z_T' \end{bmatrix} . \tag{E-4}$$

The constant C is determined by the condition that $y_s' = 0$, hence

$$C = \frac{y_T'}{y_r' + y_T'} = \frac{R_t}{R_t + R_r} . \tag{E-5}$$

Thus, the coordinates of the specular point are given by

$$\begin{bmatrix} x_s' \\ y_s' \\ z_s' \end{bmatrix} = \begin{bmatrix} x_T' + C(x_r' - x_T') \\ 0 \\ z_T' + C(z_r' - z_T') \end{bmatrix} , \tag{E-6}$$

where C is given by Eq. (E-5). These coordinates can be transformed to the standard system by using Eq. (E-2).

APPENDIX F

DISCUSSION OF VALIDITY OF APPROXIMATIONS EMPLOYED IN DIFFRACTION FORMULA

A discussion is now given of the validity of the approximations which have been used in computing the signal loss due to diffraction by a rectangular opening in an opaque screen, as discussed in Sections III, IV and VII. The present analysis makes use of the configuration shown in Fig. F-1.

Using the results of Sommerfeld,[5] p. 202, we can write the complex amplitude of the received signal due to diffraction by a rectangular aperture, relative to the receiver signal with no screen present, as

$$v_R = j\rho_t\rho_R\gamma R_f^{-2} \int_{\xi_1}^{\xi_2}\int_{\eta_1}^{\eta_2} \varepsilon^{-j(\Phi_\xi \xi^2 + \Phi_\eta \eta^2 - \Phi_{\xi\eta}\xi\eta)}\, d\xi d\eta \quad , \qquad \text{(F-1)}$$

where ρ_t is the time delay factor given in Eq. (III-2), ρ_R is the distance factor given in Eq. (III-3), R_f is the Fresnel zone size given in Eq. (III-7), and

$$\Phi_\xi = \pi(1 - \alpha^2)/R_f^2 \quad , \qquad \text{(F-2)}$$

$$\Phi_\eta = \pi(1 - \beta^2)/R_f^2 \quad , \qquad \text{(F-3)}$$

$$\Phi_{\xi\eta} = 2\pi\alpha\beta/R_f^2 \quad , \qquad \text{(F-4)}$$

where α, β, γ are the direction cosines of the line of sight relative to the ξ, η, ζ-axes, respectively, so that

$$\alpha^2 + \beta^2 + \gamma^2 = 1 \quad . \qquad \text{(F-5)}$$

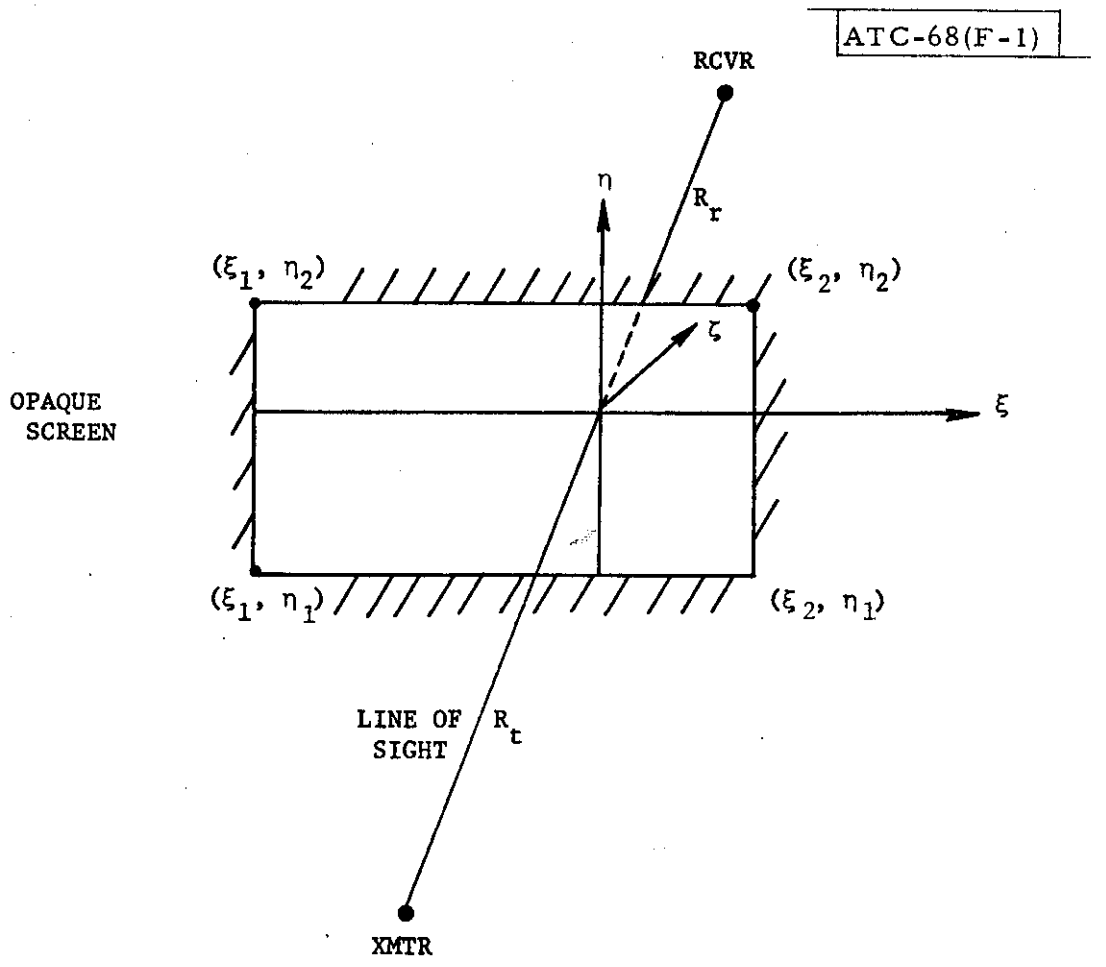

Fig. F-1. Configuration used to analyze diffraction by a rectangular aperture in an opaque screen.

If we make the change of variables $\Phi_\xi \xi^2 = \frac{\pi}{2}\xi'^2$, $\Phi_\eta \eta^2 = \frac{\pi}{2}\eta'^2$, then we can rewrite Eq. (F-1) as

$$v_R = j\rho_t \rho_R \frac{\gamma}{2\alpha_1\beta_1} \int_{X_1}^{X_2} \int_{Y_1}^{Y_2} \varepsilon^{-j\frac{\pi}{2}(\xi^2 + \eta^2)} \varepsilon^{jC\xi\eta} \, d\xi d\eta \quad , \tag{F-6}$$

where

$$\alpha_1 = (1 - \alpha^2)^{1/2} \quad , \tag{F-7}$$

$$\beta_1 = (1 - \beta^2)^{1/2} \quad , \tag{F-8}$$

$$C = \frac{\pi\alpha\beta}{\alpha_1\beta_1} \quad , \tag{F-9}$$

$$X_1 = \sqrt{2}\alpha_1\xi_1/R_f \quad , \tag{F-10}$$

$$X_2 = \sqrt{2}\alpha_1\xi_2/R_f \quad , \tag{F-11}$$

$$Y_1 = \sqrt{2}\beta_1\eta_1/R_f \quad , \tag{F-12}$$

$$Y_2 = \sqrt{2}\beta_1\eta_2/R_f \quad . \tag{F-13}$$

An approximation for v_R, as given in Eq. (F-6), has been used which is based on the assumption that $|\alpha\beta| \ll 1$, so that $\gamma \approx \alpha_1\beta_1$, and $C \approx 0$, in which case we can write

$$v_R = \frac{j}{2}\rho_t\rho_R \int_{X_1}^{X_2} \varepsilon^{-j\frac{\pi}{2}\xi^2} d\xi \int_{Y_1}^{Y_2} \varepsilon^{-j\frac{\pi}{2}\eta^2} d\eta$$

$$= \frac{j}{2}\rho_t\rho_R \left(F(X_2) - F(X_1)\right)\left(F(Y_2) - F(Y_1)\right) \quad , \tag{F-14}$$

where F(u) is the Fresnel integral defined previously in Eq. (II-34). We now examine the errors involved in these approximations. There are two sources of error, one of which occurs due to the following term not being equal to unity

$$\frac{\alpha_1\beta_1}{\gamma} = \left[\frac{(1-\alpha^2)(1-\beta^2)}{1-\alpha^2-\beta^2}\right]^{1/2} = \left(1 + \frac{\alpha^2\beta^2}{1-\alpha^2-\beta^2}\right)^{1/2}$$

$$= 1 + \frac{1}{2}\frac{\alpha^2\beta^2}{1-\alpha^2-\beta^2} + \cdots \tag{F-15}$$

It is easily seen that the second term in Eq. (F-15) will be small compared to unity, if $|\alpha\beta| \ll 1$ and $\alpha^2 + \beta^2 \neq 1$. In particular, if $\alpha = 0$, or $\beta = 0$, then this second term is zero and need not be considered.

The second source of error, relative to the term $\frac{j}{2}\rho_t\rho_R$, is due to the following

$$E = \int_{X_1}^{X_2}\int_{Y_1}^{Y_2} \varepsilon^{-j\frac{\pi}{2}(\xi^2+\eta^2)}\left(1 - \varepsilon^{jC\xi\eta}\right) d\xi d\eta \, . \tag{F-16}$$

Using the series expansion for $\varepsilon^{jC\xi\eta}$, Eq. (F-16) can be written as

$$E = jC \int_{X_1}^{X_2} \xi \varepsilon^{-j\frac{\pi}{2}\xi^2}\, d\xi \int_{Y_1}^{Y_2} \eta \varepsilon^{-j\frac{\pi}{2}\eta^2}\, d\eta \; +$$

$$(jC)^2 \int_{X_1}^{X_2} \xi^2 \varepsilon^{-j\frac{\pi}{2}\xi^2}\, d\xi \int_{Y_1}^{Y_2} \eta^2 \varepsilon^{-j\frac{\pi}{2}\eta^2}\, d\eta \; +$$

$$\frac{(jC)^3}{6} \int_{X_1}^{X_2} \xi^3 \varepsilon^{-j\frac{\pi}{2}\xi^2}\, d\xi \int_{Y_1}^{Y_2} \eta^3 \varepsilon^{-j\frac{\pi}{2}\eta^2}\, d\eta \; + \; . \; . \; . \qquad \text{(F-17)}$$

However, according to Gradshteyn and Ryzhik,[26] p. 194, equation numbers 5, 6, we have the following integration formulas

$$\int x \varepsilon^{-j\frac{\pi}{2}x^2}\, dx = \frac{j}{\pi} \varepsilon^{-j\frac{\pi}{2}x^2} \quad , \qquad \text{(F-18)}$$

$$\int x^2 \varepsilon^{-j\frac{\pi}{2}x^2}\, dx = \frac{j}{\pi}\left(x\varepsilon^{-j\frac{\pi}{2}x^2} - F(x)\right) \quad , \qquad \text{(F-19)}$$

$$\int x^3 \varepsilon^{-j\frac{\pi}{2}x^2}\, dx = \frac{j}{\pi}\left(x^2 \varepsilon^{-j\frac{\pi}{2}x^2} - \frac{2j}{\pi} \varepsilon^{-j\frac{\pi}{2}x^2}\right) \quad . \qquad \text{(F-20)}$$

These integration formulas can be verified by direct differentiation. If we substitute these expressions for the appropriate integrals in Eq. (F-17), multiply and collect terms, we get

$$E = -\frac{jC}{\pi^2}\sum_{m,n=1}^{2} H(X_m,Y_n) + O(C^2) \quad , \tag{F-21}$$

where

$$H(X_m,Y_n) = (-1)^{m+n}\varepsilon^{-j\frac{\pi}{2}(X_m^2 + Y_n^2)}\varepsilon^{j\frac{C}{2}X_mY_n}\ \text{sinc}\ (\tfrac{C}{2}X_mY_n) \quad , \tag{F-22}$$

$$\text{sinc}\ (x) = \frac{\sin x}{x} \quad , \tag{F-23}$$

and $O(C^2)$ is a term which, when divided by C^2, remains constant as $C \to 0$.

In general, the expression in Eq. (F-21) can be used to obtain an estimate of the error involved in approximating the Fresnel surface integral in Eq. (F-6) by the product of one-dimensional Fresnel integrals, as given in Eq. (F-14). If $C \ll 1$, then using the fact that $|\text{sinc}\ (x)| \leq 1$, for all x, we have

$$|E| \leq \frac{4}{\pi^2}|C| = \frac{4}{\pi}\frac{|\alpha\beta|}{((1-\alpha^2)\ (1-\beta^2))^{1/2}} \quad . \tag{F-24}$$

We assume $|\beta| \leq \beta_{max}$, $\beta_{max} \ll 1$, and that $|\alpha| \leq 1/2$, so that $\frac{|\alpha|}{(1-\alpha^2)^{1/2}} \leq 1$, and we obtain

$$|E| \leq \frac{4}{\pi}\beta_{max} \quad . \tag{F-25}$$

We can also consider $|E|$ to be the error relative to the value for $|v_r|$ obtained when either α or β is zero and the line of sight intersects the center of a diffraction aperture whose dimensions are very large, since in this case this value for $|v_r|$ is equal to unity. If $\beta_{max} = 0.2$, corresponding to a direction cosine angle of about 78.5 degrees, then $|E| \leq 0.26$,

which corresponds to an error of 20 · log (1.26) = 1.97 dB. Thus, if $|\beta|$ is less than 0.2, an error of only about 2 dB occurs. Similarly, if $|\alpha| \leq \alpha_{max}$ and $|\beta| \leq 1/2$, we obtain the same error of about 2 dB when $\alpha_{max} = 0.2$.

It has been shown that small errors occur if $|\alpha\beta| \ll 1$, i.e., $\alpha \approx 0$, or $\beta \approx 0$. or $\alpha\beta \approx 0$. This implies that the line of sight lies in a plane which is perpendicular to the diffraction aperture and is parallel to one of the edges of the aperture. This will be approximately the case for building and aircraft reflections when these obstacles, as well as the transmitter and receiver, are close to the ground plane. It is also true for shadowing buildings, and shadowing aircraft which are close to the ground plane. However, there would be some problem in employing the approximations for those situations where the shadowing aircraft is at a significantly high altitude. In these cases a Fresnel surface integral would have to be computed, as discussed by Millington et al.[27, 28] This is a rather complex procedure, and is, therefore, undesirable to use in a computer program. In these situations the present approach is still applicable and may be considered as an approximation.

APPENDIX G

DETERMINATION OF SPECULAR POINT FOR REFLECTION FROM CYLINDER

A discussion is now given of the method employed to compute the position of the specular point for reflection from a cylinder, i.e., either aircraft fuselage or tail fin, as discussed in Section IV. The geometry for this problem is depicted in Fig. G-1. For simplicity, this figure shows only the transformed coordinate axis, i.e., x', y', z'-axes. In the case of the fuselage, these axes are obtained in a manner similar to that indicated for buildings in Appendix E, i.e.,

$$\begin{bmatrix} x' \\ y' \\ z' \end{bmatrix} = \begin{bmatrix} 0 & 0 & -1 \\ -\sin\theta & \cos\theta & 0 \\ \cos\theta & \sin\theta & 0 \end{bmatrix} \begin{bmatrix} x \\ y \\ z \end{bmatrix}, \qquad \text{(G-1)}$$

and

$$\begin{bmatrix} x \\ y \\ z \end{bmatrix} = \begin{bmatrix} 0 & -\sin\theta & \cos\theta \\ 0 & \cos\theta & \sin\theta \\ -1 & 0 & 0 \end{bmatrix} \begin{bmatrix} x' \\ y' \\ z' \end{bmatrix}, \qquad \text{(G-2)}$$

where θ is the angle between the fuselage axis and the centerline, or xz-plane. In dealing with the tail fin, there is no transformation of coordinates, i.e., $x' = x$, $y' = y$, $z' = z$.

It is advantageous to view the vertical cylinder in Fig. G-1 from the top, as shown in Fig. G-2. Using this figure, we have

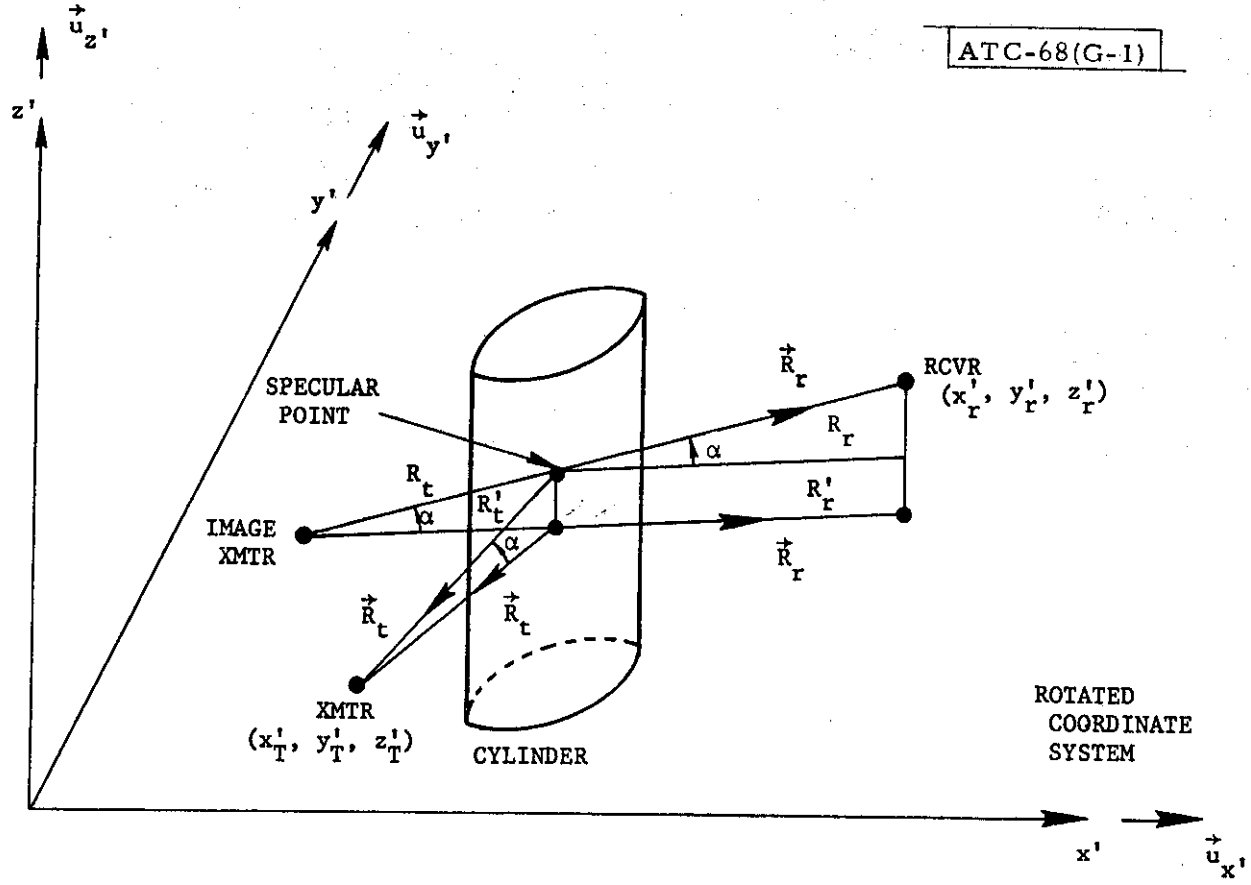

$\vec{u}_{x'}$, $\vec{u}_{y'}$, $\vec{u}_{z'}$ ARE UNIT VECTORS IN x', y', z' DIRECTIONS, RESPECTIVELY

IMAGE XMTR IS TAKEN RELATIVE TO PLANE TANGENT TO CYLINDER AT SPECULAR POINT

$R_t = |\vec{R}_t|$, $R_r = |\vec{R}_r|$, $R'_t = |\vec{R}'_t|$, $R'_r = |\vec{R}'_r|$

Fig. G-1. Geometry employed to determine position of specular point for reflection from cylinder.

ATC-68(G-2)

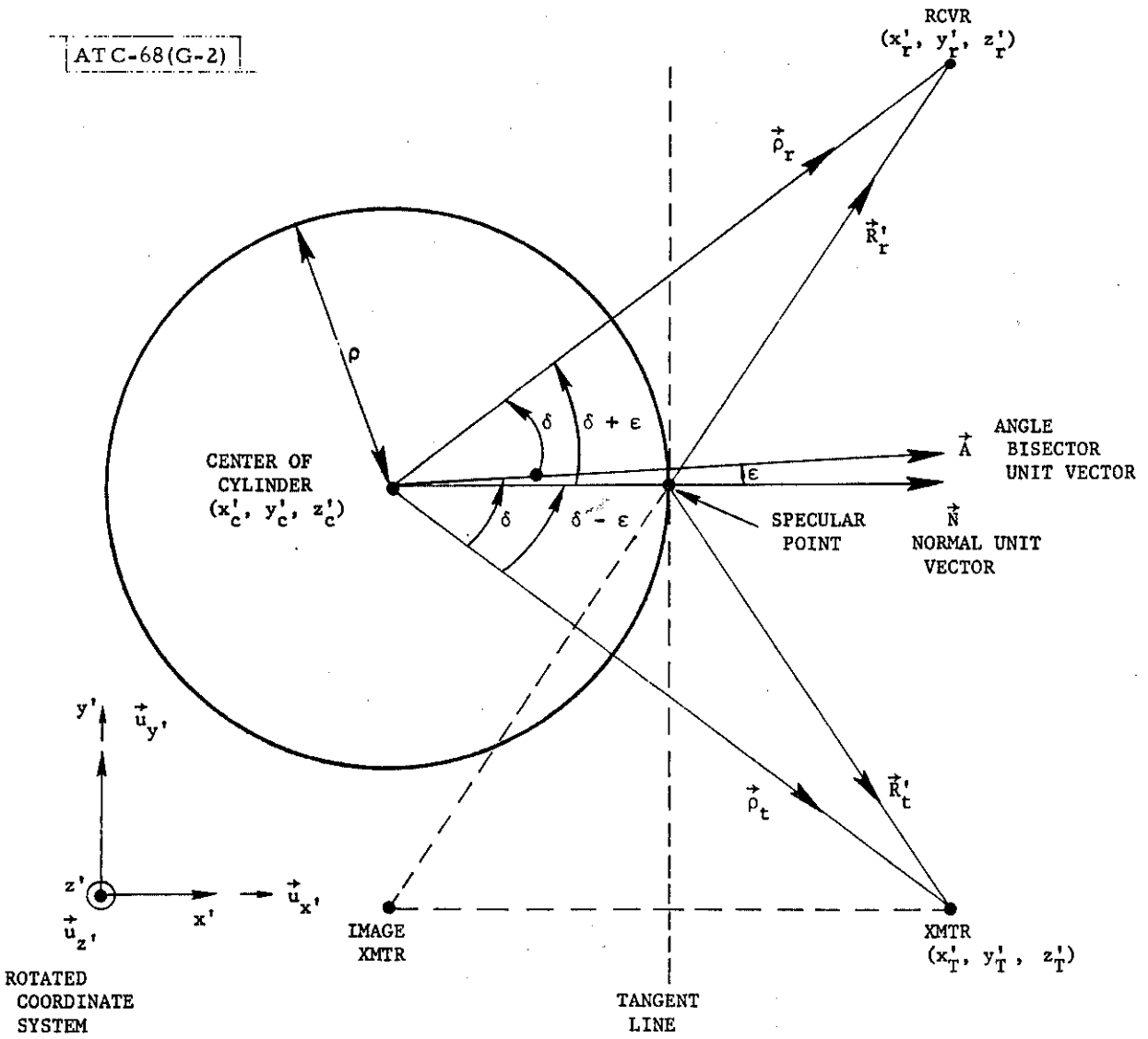

z' AXIS POINT UPWARD

$u_{x'}$, $u_{y'}$, $u_{z'}$ ARE UNIT VECTORS IN x', y', z' DIRECTIONS, RESPECTIVELY

$\vec{\rho}_r = \rho_{rx'} \vec{u}_{x'} + \rho_{ry'} \vec{u}_{y'}$, $\vec{\rho}_t = \rho_{tx'} \vec{u}_{x'} + \rho_{ty'} \vec{u}_{y'}$

$R'_t = |\vec{R}'_t|$, $R'_r = |\vec{R}'_r|$, $\rho_t = |\vec{\rho}_t|$, $\rho_r = |\vec{\rho}_r|$

Fig. G-2. Method used in determination of specular point.

$$\sin(2\delta) = \frac{1}{\rho_r \rho_t} \left(\vec{u}_{z'} \cdot (\vec{\rho}_t \times \vec{\rho}_r) \right) \quad ,$$

so that

$$\delta = \frac{1}{2} \sin^{-1} \left[\frac{\rho_{tx'} \rho_{ry'} - \rho_{ty'} \rho_{rx'}}{\rho_t \rho_r} \right] \quad . \tag{G-3}$$

The unit vector $\vec{A}$ in the direction of the angle bisector is obtained as

$$\vec{A} = \frac{\rho_t \vec{\rho}_r + \rho_r \vec{\rho}_t}{| \rho_t \vec{\rho}_r + \rho_r \vec{\rho}_t |} \quad . \tag{G-4}$$

The small angle ε is gotten by noting from Fig. G-2

$$\tan \beta = \frac{\rho_r \sin(\delta+\varepsilon)}{\rho_r \cos(\delta+\varepsilon) - \rho} = \frac{\rho_t \sin(\delta-\varepsilon)}{\rho_t \cos(\delta-\varepsilon) - \rho} \quad ,$$

so that

$$\rho_r \rho_t \sin(\delta+\varepsilon) \cos(\delta-\varepsilon) - \rho_r \rho \sin(\delta+\varepsilon) = \rho_r \rho_t \sin(\delta-\varepsilon) \cos(\delta+\varepsilon) - \rho_t \rho \sin(\delta-\varepsilon)$$

and

$$\sin(2\varepsilon) = \frac{\rho}{\rho_t} \sin(\delta+\varepsilon) - \frac{\rho}{\rho_r} \sin(\delta-\varepsilon) \quad . \tag{G-5}$$

The transcendental equation for ε in Eq. (G-5) is solved by means of a trial and error procedure to determine ε, using the value for the angle δ obtained from Eq. (G-3). However, if $\rho/\rho_t \leq 0.01$, and $\rho/\rho_r \leq 0.01$, this procedure is skipped and ε is taken to be zero.

The unit vector $\vec{N}$, pointing in the direction between the center of the cylinder and the specular point, is determined by noting the following vector product relationships,

$$\vec{N} \cdot \vec{A} = \cos \varepsilon \quad , \tag{G-6}$$

$$(\vec{N} \times \vec{A}) \cdot \vec{u}_{z'} = \sin \varepsilon \ . \tag{G-7}$$

Thus, the components of the vector $\vec{N}$ are

$$N_{x'} = A_{x'} \cos \varepsilon + A_{y'} \sin \varepsilon$$

$$N_{y'} = -A_{x'} \sin \varepsilon + A_{y'} \cos \varepsilon \quad . \tag{G-8}$$

Hence, the x', y' coordinates of the specular point are

$$x_s' = x_c' + \rho N_{x'} \quad , \tag{G-9}$$

$$y_s' = y_c' + \rho N_{y'} \quad . \tag{G-10}$$

In order to find the z' coordinate of the specular point, we note from Fig. G-1 that the image transmitter, the specular point, and the receiver must be collinear, so that

$$z_s' = z_T' + R_t' \tan \alpha$$

$$= z_T' + R_t' \left(\frac{z_r' - z_t'}{R_t' + R_r'} \right)$$

$$= z_T' + C(z_r' - z_t') \quad , \tag{G-11}$$

where

$$C = \frac{R_t'}{R_t' + R_r'} = \frac{R_t}{R_t + R_r} \quad . \tag{G-12}$$

In the case of the fuselage, the position of the specular point in the unprimed, or standard, coordinate system may be obtained by using Eq. (G-2). For the tail fin, this transformation is not necessary, as noted previously.

We also mention that a check is necessary to determine whether the cylinder reflection solution, which is obtained according to the preceding method, is a feasible one. This is done by noting whether the following two necessary conditions are satisfied by the solution obtained for the specular point:

(1) The transmitter and receiver must both lie on the same side of the tangent line, cf. Fig. G-2.

(2) The center of the cylinder must lie on the opposite side of the tangent line from the transmitter and receiver, cf. Fig. G-2.

In addition, a third condition is necessary when dealing with the tail fin reflection case:

(3) The specular point must lie on that part of the cylinder defined by the boundaries of the tail fin, i.e., the specular point must lie on the tail fin.

For the fuselage case, if conditions (1) and (2) are satisfied, the magnitude of the multipath component is computed as indicated in Section IV, and otherwise, this magnitude is set to zero, i.e., the fuselage is not oriented for a specular reflection. In the tail fin case, if conditions (1), (2), and (3) are satisfied, the magnitude of the multipath component is computed as indicated in Section IV, and otherwise, this magnitude is set to zero, i.e., the tail fin is not oriented for a specular reflection.

APPENDIX H

TRANSFORMATIONS OF COORDINATES REQUIRED FOR SHADOWING AIRCRAFT

A description is now presented of some of the calculations required to compute the shadowing effect due to aircraft, as described in Section VII. The geometry for this problem is shown in Fig. H-1. It should be noted that in Fig. H-1 the fuselage axis of the shadowing aircraft lies in the plane, containing the flight path, which is perpendicular to the ground, or xy-plane.

We begin the discussion by computing the direction cosines for the x'-axis, shown in Fig. H-1, which lies along the direction of the fuselage axis of the shadowing aircraft. Denoting these three direction cosines by a_1, b_1, c_1, relative to the x, y, z- axes, respectively, we have

$$c_1 = -\sin \theta_1 \quad , \tag{H-1}$$

since the fuselage axis makes an angle of θ_1 with the xy-plane, and

$$\frac{b_1}{c_1} = \frac{\Delta y}{\Delta x} \quad , \tag{H-2}$$

since the fuselage axis lies in the plane containing the flight path which is perpendicular to the xy-plane, where $\Delta y = y_1 - y_2$, $\Delta x = x_1 - x_2$. In addition, these direction cosines must satisfy the condition

$$a_1^2 + b_1^2 + c_1^2 = 1 \quad . \tag{H-3}$$

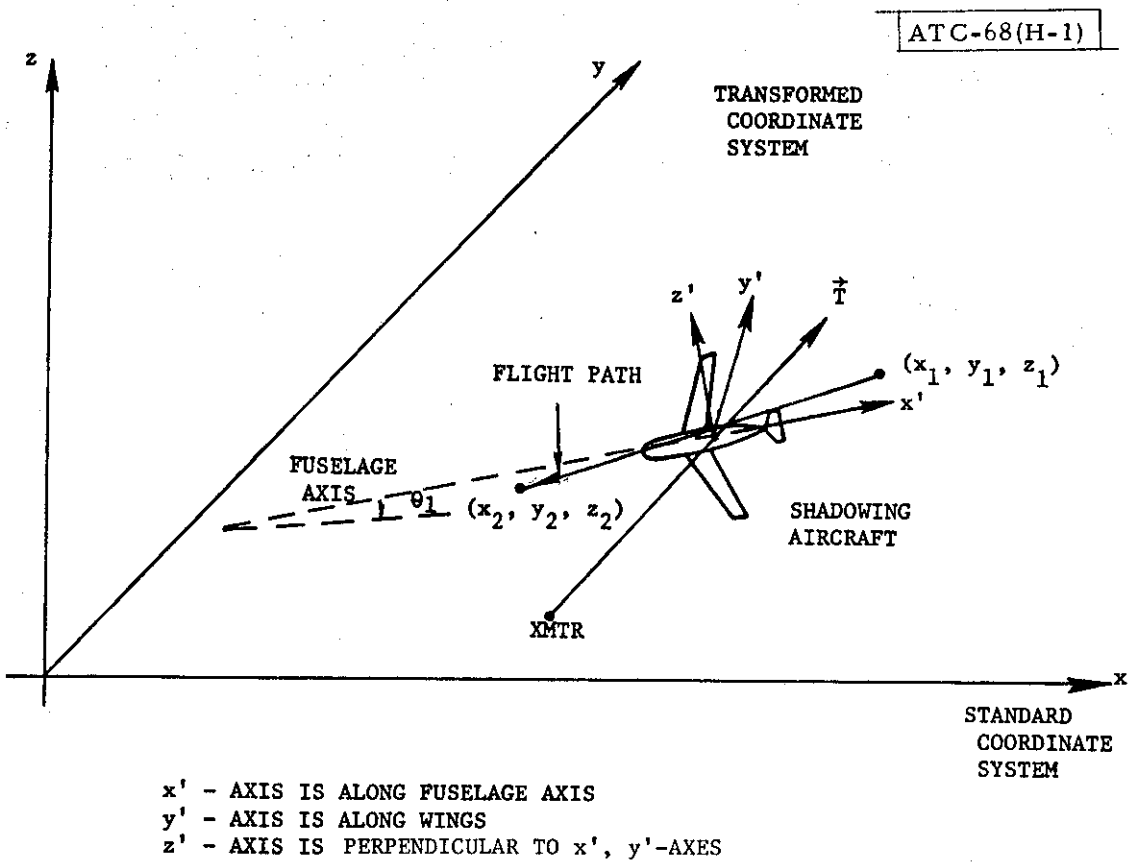

Fig. H-1. Geometry used for computing shadowing effect due to aircraft.

Using Eqs. (H-1) -(H-3) we can solve for a_1, b_1 as

$$a_1 = |\cos \theta_1| \, \Delta x/\Delta R \quad , \tag{H-4}$$

$$b_1 = |\cos \theta_1| \, \Delta y/\Delta R \quad , \tag{H-5}$$

where

$$\Delta R = (\Delta x^2 + \Delta y^2)^{1/2} \quad . \tag{H-6}$$

The magnitude sign is required in Eqs. (H-4), (H-5) in order to keep the signs of a_1, b_1 the same as Δx, Δy, respectively.

It should be noted that when the flight path is parallel to the z-axis, so that $\Delta x = \Delta y = 0$, there is an unresolvable ambiguity which is arbitrarily resolved by assuming that the fuselage axis is parallel to the xz-plane. In this case we have $b_1 = 0$, $a_1 = \cos \theta_1$, while c_1 is still given by Eq. (H-1).

We now calculate the direction cosines for the z'-axis, shown in Fig. H-1, which lies in the plane containing the flight path which is perpendicular to the xy-plane. These three direction cosines are denoted as a_3, b_3, c_3, and are taken relative to the x, y, z-axis, respectively. Since the z'-axis is perpendicular to the x'-axis, we have

$$a_1 a_3 + b_1 b_3 + c_1 c_3 = 0 \quad . \tag{H-7}$$

The x'z'-plane is parallel to the z-axis, so that the z-component of the vector cross product, between the unit vectors in the x', z' directions, must be zero. Hence, we obtain

$$a_3 b_1 - b_3 a_1 = 0 \quad . \tag{H-8}$$

In addition, these direction cosines must satisfy the usual condition

$$a_3^2 + b_3^2 + c_3^2 = 1 \quad . \tag{H-9}$$

Using Eqs. (H-7) - (H-9) we can solve for a_3, b_3, c_3 as

$$a_3 = - \frac{a_1 c_1}{(a_1^2 + b_1^2)^{1/2}} \quad , \tag{H-10}$$

$$b_3 = - \frac{b_1 c_1}{(a_1^2 + b_1^2)^{1/2}} \quad , \tag{H-11}$$

$$c_3 = (a_1^2 + b_1^2)^{1/2} \quad , \tag{H-12}$$

where a_1, b_1, c_1 are the direction cosines for the x'-axis given in Eqs. (H-4), (H-5), (H-1), respectively.

If $a_1 = b_1 = 0$, $c_1 = 1$, then the fuselage is aligned along the z- axis, and there is an unresolvable ambiguity which is arbitrarily resolved by assuming that the shadowing aircraft wings make an angle of 90 degrees with respect to the x-axis. In this case we have $a_3 = -c_1$, $b_3 = -b_1$, $c_3 = a_1$.

The direction cosines of the y'-axis are denoted as a_2, b_2, c_2, relative to the x, y, z-axes, respectively. These direction cosines are obtained by observing that the unit vector in the direction of the y'-axis is equal to the vector cross product of the unit vectors in the directions of the z', x'-axes.

Hence, we have

$$a_2 = b_3c_1 - c_3b_1 \quad , \tag{H-13}$$

$$b_2 = c_3a_1 - a_3c_1 \quad , \tag{H-14}$$

$$c_2 = a_3b_1 - b_3a_1 \quad . \tag{H-15}$$

In order to determine the profile of the shadowing aircraft, as discussed in Section VII A, the viewing, or aspect, angles of the aircraft, as seen from the transmitter, must be calculated. The geometry for this problem is depicted in Fig. H-2. The viewing angles α and β are given by

$$\alpha = \sin^{-1}(\vec{T} \cdot \vec{u}_{y'}/|\vec{T}|) \quad , \tag{H-16}$$

$$\beta = \sin^{-1}(\vec{T} \cdot \vec{u}_{z'}/|\vec{T}|) \quad , \tag{H-17}$$

where we have used the fact that the magnitude of the vector $\vec{T}$, i.e., $|\vec{T}|$, is the same as the magnitude of this vector after it has been transformed into the x', y', z' - coordinate system by a simple rotation of coordinates. The following conditions define the various profiles for the shadowing aircraft, as seen from the transmitter:

Front-Back Profile

$$|\alpha| \leq 5^{o}$$

$$|\beta| \leq 5^{o}$$

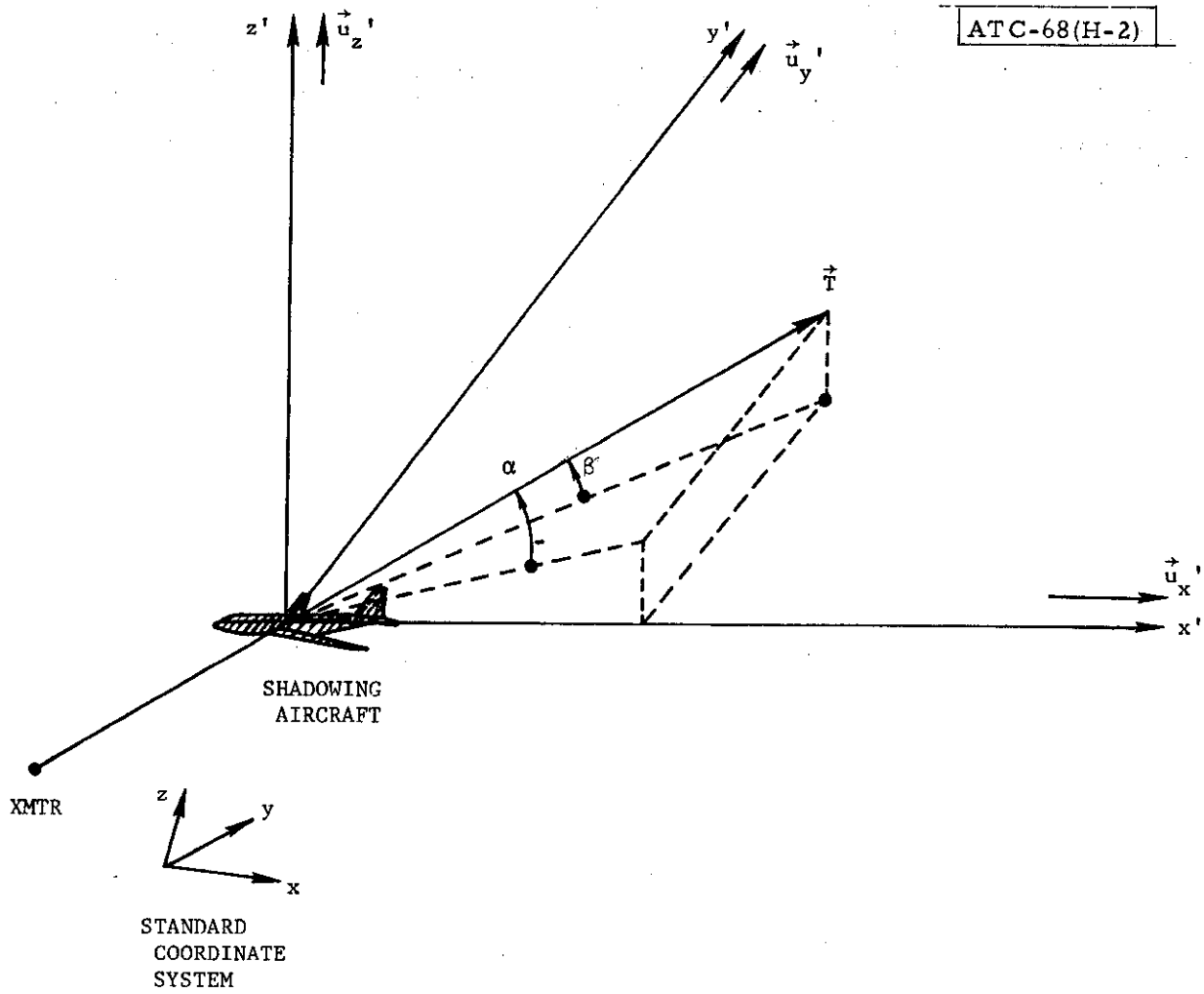

Fig. H-2. Geometry employed for computing viewing angles of shadowing aircraft as seen from transmitter.

Side Profile

$$|\alpha| > 5^{o}$$

$$|\beta| \leq 5^{o}$$

Bottom-Top Profile

$$|\beta| \geq 5^{o}$$

The computation of the shadowing effect, due to aircraft and buildings, is facilitated by making a transformation of coordinates so that the new coordinate system is centered on the diffraction aperture, as shown in Fig. VII-3. However, the details for doing this for shadowing aircraft are similar to those presented previously in Appendix B. In the case of shadowing buildings, the details for performing this transformation are similar to those presented previously in Appendix E, except that there is only a single rotation of coordinates that is required. That is, the rotation of coordinates required to account for the building tilt angle is not necessary for the case of shadowing buildings. Hence, no additional exposition of these details is required at this point.

APPENDIX J

THEORETICAL JUSTIFICATION FOR THE ASSIGNMENT OF COMPLEX AMPLITUDES OF EDGE RAYS

We now provide the justification for the method, which was used in Section VII, to assign the complex amplitudes to the edge rays. This justification is given only for case A, since it is similar for cases B and C. The expression for V_{SH} given in Eq. (VII-1) can be written as

$$V_{SH} = \underbrace{1}_{\text{Direct wave}} + \rho_z \left(\underbrace{\frac{\varepsilon^{-j\frac{\pi}{2}\tilde{y}_2^2}}{\sqrt{2}\,\pi\,\tilde{y}_2}}_{\text{Right-hand edge ray}} - \underbrace{\frac{\varepsilon^{-j\frac{\pi}{2}\tilde{y}_1^2}}{\sqrt{2}\,\pi\,\tilde{y}_1}}_{\text{Left-hand edge ray}} \right) , \qquad \text{(J-1)}$$

where $\tilde{y}_2$, $\tilde{y}_1$, ρ_z have been given previously in Eqs. (VII-2), (VII-3), (VII-14), respectively, and it has been assumed that $\tilde{y}_1$, $\tilde{y}_2$ are both very large and positive, so that we may use the following asymptotic expansion for the Fresnel integral, cf. Sommerfeld,[5] p. 241,

$$F(x) = F(\infty) + j\,\frac{\varepsilon^{-j\frac{\pi}{2}x^2}}{\pi\,x} = \frac{1}{2}(1-j) + j\,\frac{\varepsilon^{-j\frac{\pi}{2}x^2}}{\pi\,x} , \quad x \to \infty . \qquad \text{(J-2)}$$

The expression for V_{SH} in Eq. (J-1) indicates that it is given by a sum of a direct wave plus 2 edge rays, as required for case A and discussed in Section VII B. In particular, the second term in Eq. (J-1) corresponds to the right-hand edge ray, while the third term corresponds to the left-hand ray.

We now compute the distance traversed by the edge rays, relative to the direct path between transmitter and receiver. For simplicity, we consider only the left-hand edge ray, since the analysis for the right-hand edge ray is similar. Using the results of Appendix F, and the Fresnel approximation discussed by Sommerfeld,[5] p. 202, we can write that the distance traversed by the left-hand edge ray, relative to the direct path, is

$$\Delta R_L = \left(\frac{1}{R_t} + \frac{1}{R_r}\right)\left(\frac{(y_1 - y_s)^2(1 - \alpha^2)}{2}\right) = \lambda\, \tilde{y}_1^{\,2}/4 \quad , \qquad \text{(J-3)}$$

where α is the direction cosine of the line of sight relative to the ξ-axis, and it has been assumed that the direction cosine of the line of sight relative to the η-axis, denoted as β, is equal to zero, cf. Appendix F. The phase delay of the left-hand edge ray, relative to the direct wave, is obtained from Eq. (J-3) as

$$\phi_L = 2\pi\, \Delta R_L/\lambda = \pi\, \tilde{y}_i^{\,2}/2 \quad . \qquad \text{(J-4)}$$

However, this is just the phase delay associated with the left-hand edge ray, as indicated by its associated complex amplitude in Eq. (J-1). Thus, the justification for assigning a complex amplitude to an edge ray is that it provides the correct phase delay for the particular path traversed by that edge ray.

APPENDIX K

DISCUSSION OF TRANSMITTER AND RECEIVER ANTENNA PATTERNS

A discussion is now presented of the effect of the transmitter and receiver antenna patterns, denoted by $G(\alpha,\beta)$, $G_A(\alpha',\beta')$, respectively, on the various computational procedures presented in Sections II - VII. The angles α,β and α',β' are the planar azimuth, elevation angles, for the vectors $\vec{R}_t$, $\vec{R}_r$, measured relative to a coordinate system centered on the transmitter, receiver, respectively, cf. Fig. II-1.

In Sections II - VII, all expressions for the relative multipath amplitude should contain multiplicative factors $G(\alpha,\beta) \cdot G_A(\alpha',\beta')$. However, it has been mentioned that it is desired to maintain the multipath subroutines as being system-independent. Thus, these multiplicative factors are applied in the system subroutines, using the information about the planar directional angles supplied by the multipath subroutines. In addition, for simplicity, $G(\alpha,\beta)$, $G(\alpha',\beta')$ typically are each taken as a product of two patterns, each of which depends on α,β, and α',β', only.

We now discuss the rationale for removing the antenna patterns from inside the integral in Eq. (II-20). In general, the transmitter antenna pattern, $G(\alpha,\beta)$, changes with time. For example, in the time reference scanning beam MLS implementation, the antenna pattern is scanned through azimuthal and elevation angles in the azimuth and elevation guidance systems, respectively. Thus, the integral in Eq. (II-20) would have to be evaluated for many different

transmitter antenna patterns during a given scan in a particular MLS implementation. In order to avoid this complication, the quantity $G(\alpha,\beta)$ was removed from inside the integral in Eq. (II-20). The resulting integral is computed only once, for a given aircraft position, and the result multiplied by $G(\alpha,\beta)$, where α,β are the planar azimuth and elevation angles, respectively, for the vector direction between the transmitter and the specular point on the ground. It should be noted that this factor, $G(\alpha,\beta)$, will, in general, vary with time. The justification for removing the quantity $G(\alpha,\beta)$ from inside the integral in Eq. (II-20) is provided subsequently. It was also assumed that the aircraft receiver antenna pattern, $G_A(\alpha',\beta')$, can be removed from inside the integral in Eq. (II-20), as was the case for $G(\alpha,\beta)$. This assumption is, of course, justified if the aircraft receiver antenna pattern is omnidirectional, so that $G_A(\alpha',\beta') = 1$ for all α',β'.

It is important to state that in some cases the transmitter antenna pattern, $G(\alpha,\beta)$, should be the near-field, and not the far-field, pattern. In these cases, this near-field pattern could change considerably as the range R_t varies. The near field of the antenna is usually defined as extending a distance from the antenna of $R = 2D^2/\lambda$, where D is the dimension of the antenna. The situations in which the near-field, and not the far-field, pattern is required occur when D is large, so that R is large enough for the near field to encompass the region defined by the first Fresnel zone. As an example, in the MLS configuration, for either the azimuth pattern of the azimuth array, or the elevation pattern of the elevation array, we have typically $D = 60\lambda$, so that $R = 7200\lambda$. At C-band, $\lambda = 6$ cm $\cong 0.2$ feet, so that

$R \simeq 1{,}440$ feet. In this case, the first Fresnel zone is found typically to lie entirely within the near field of the transmitter antenna. For example, at C-band, if $h_t = 9$ feet, and if the aircraft is at a range of 20 miles and elevation angle of 2.5°, then the first Fresnel zone is an ellipse which is 200 feet long by 9 feet wide, centered approximately 200 feet from the transmitter antenna, and thus lies completely within the near zone. We now give an example of a situation where the far-field pattern is required. The azimuthal pattern of the elevation array typically corresponds to an aperture $D = 5\lambda = 1$ foot, so that $R = 10$ feet and the near field is well outside the region defined by the first Fresnel zone described previously. A somewhat marginal situation occurs for the elevation pattern of the azimuth array which typically corresponds to an aperture $D = 20\lambda = 4$ feet, so that $R = 160$ feet. However, for simplicity, the MLS system subroutines which have been developed employ the far-field pattern for $G(\alpha,\beta)$.

We now wish to justify the procedure of removing the transmitter antenna pattern for the radiated field, $G(\alpha,\beta)$, from inside the integral in Eq. (II-20), as noted previously. Towards this end, the integral in Eq. (II-20) was evaluated with $G(\alpha,\beta)$ inside, and outside, the integral. When the quantity $G(\alpha,\beta)$ is taken outside the integral, the resulting integral is multiplied by $G(\alpha,\beta)$, where α,β are the planar azimuth and elevation angles, respectively, for the vector direction between the transmitter and the specular point on the ground. The results of these two separate computations for $|\rho_s|$ are illustrated in Figs. K-1 and K-2. Both of these sets of data were obtained using a $(\sin x/x)^2$ radiation pattern with a 1° beamwidth. The results of Fig. K-1

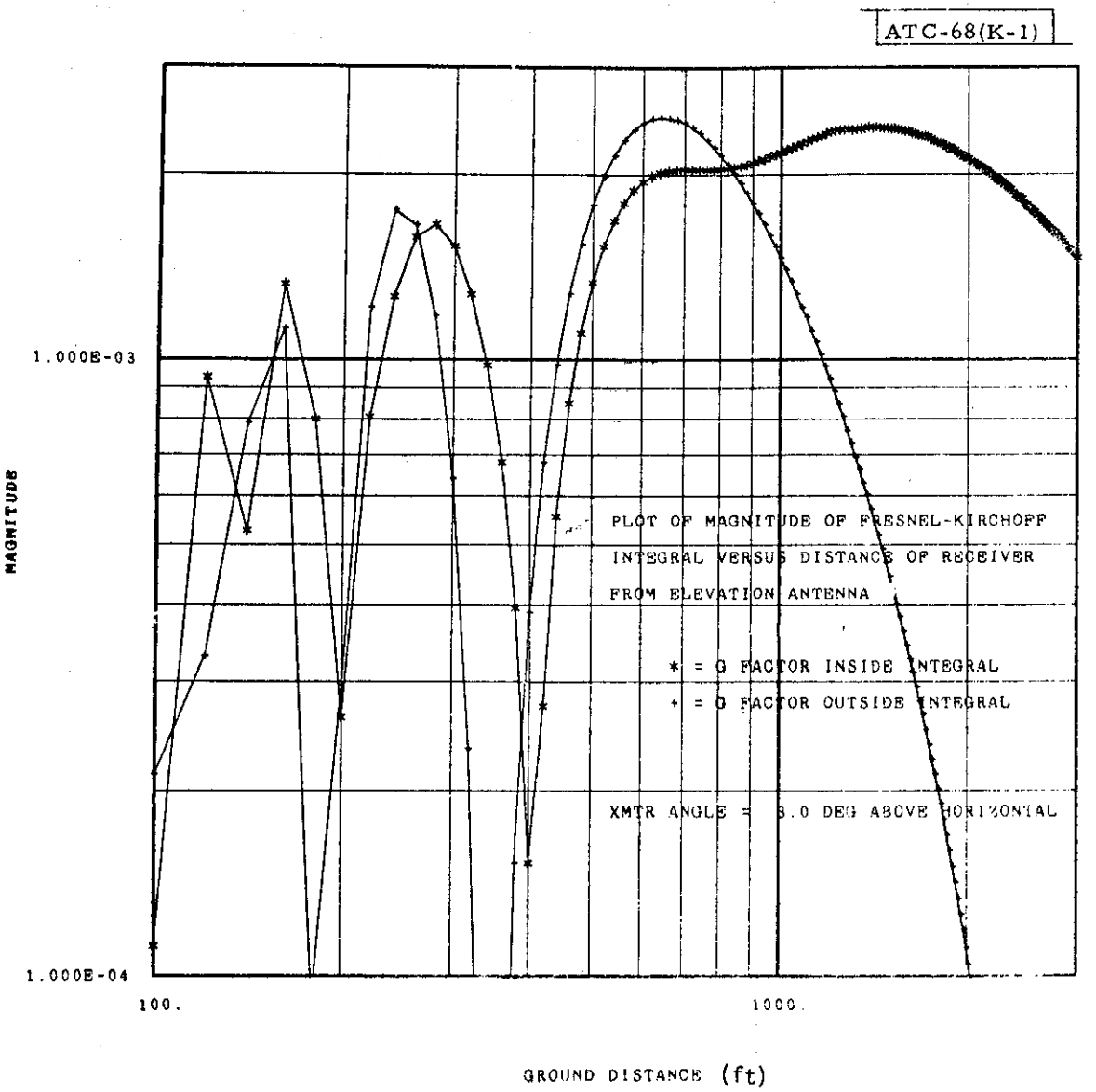

Elevation antenna located at (9000, -400, 0), with a 1° beamwidth $(\sin x/x)^2$ pattern

Aircraft receiver on 20:1 linear centerline glide path terminating at (9000, 0, 0)

Fig. K-1. Plot of magnitude of Fresnel-Kirchoff diffraction integral for a flat, smooth, perfectly-conducting surface, vs distance of receiver from elevation antenna, with antenna pattern inside and outside of integral.

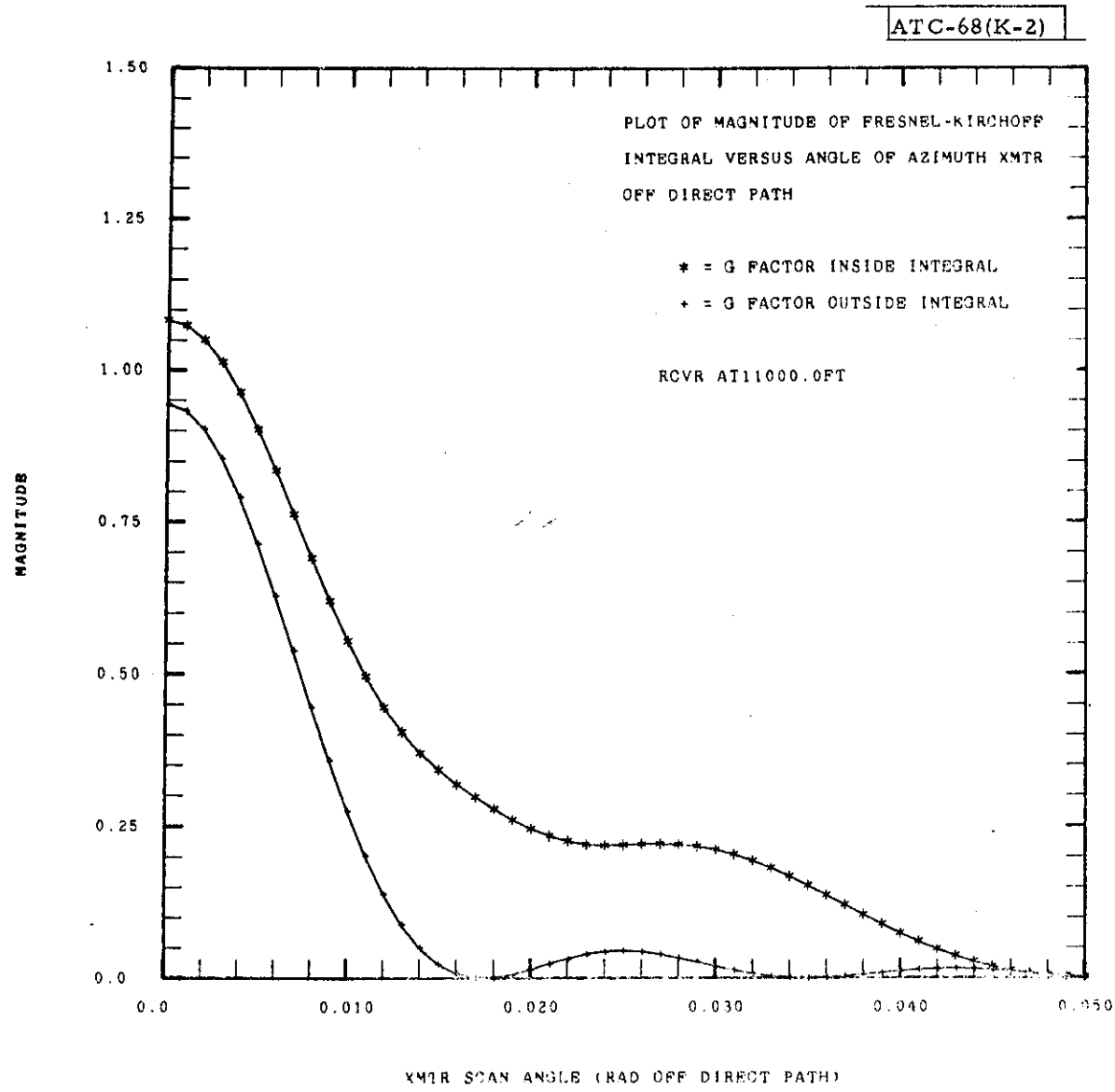

Azimuth antenna located at (0, 0, 7) with 1° beamwidth $(\sin x/x)^2$ pattern

Aircraft receiver at (11000, 0, 100)

Fig. K-2. Plot of magnitude of Fresnel-Kirchoff integral, for a flat, smooth, perfectly-conducting surface, vs scan angle of azimuth transmitter relative to centerline, with antenna pattern inside and outside of integral.

were obtained for an elevation scanning antenna system, while those of Fig. K-2 are applicable for an azimuth scanning antenna system. In both of these figures the two computations are reasonably close to each other. In addition, for the elevation system, the data of Fig. K-1 show that the results obtained for the two sets of computations are very small, less than 0.03, so that in this case the specular ground reflection may be neglected. The results in Fig. K-1 also illustrate the sidelobe structure of the elevation system antenna pattern. Thus, these facts provide the justification for computing ρ_s with $G(\alpha,\beta)$ outside of the integral in Eq. (II-20), as is done in the computer simulation program. However, we mention that there could be some situations in which this procedure could lead to errors which are larger than those indicated above. For example, larger errors could occur if the effect of the elevation pattern rolloff near the horizon, on the azimuth array, is taken into account in Fig. K-2.

In Sections III and IV, the discussion of scattering from buildings and aircraft contained an implicit operation in which the transmitter antenna pattern, $G(\alpha,\beta)$, was removed from inside the Fresnel-Kirchoff diffraction integral, as was done in Section II, cf. Eqs. (III-1) and (IV-1). It is possibly to justify this operation if the obstacle, or building, lies in the far field of the transmitter antenna, as will now be shown. In order to show this, we note that the approximation should be valid if the Fresnel zone size, R_f, is less than a transmitter beamwidth in extent, i.e.,

$$R_f < \theta R_t \qquad \text{(K-1)}$$

where θ is the angular beamwidth. Thus, using Eq. (III-7), we have

$$R_f = \sqrt{\lambda \frac{R_t R_r}{R_t + R_r}} \leq \sqrt{\lambda R_t} \quad , \qquad \text{(K-2)}$$

so that we can write the inequality in (K-1) as

$$\sqrt{\lambda R_t} < \theta R_t \quad . \qquad \text{(K-3)}$$

However, since $\theta \approx \lambda/D$, we have finally

$$D^2/\lambda < R_t \quad , \qquad \text{(K-4)}$$

which is essentially the condition that the obstacle be located in the far field of the transmitter antenna. For a 60λ C-band array, D = 12 feet, λ = 0.2 feet, and R_t must be greater than 720 feet, which is true in nearly all cases of practical interest.

ACKNOWLEDGEMENT

The author would like to express his sincere appreciation to his colleague Dr. J.E. Evans for many helpful comments and suggestions concerning this work.

REFERENCES

1. Beckmann, P., "Scattering by Composite Rough Surfaces," Proc. IEEE (August 1965), pp. 1012-1015.

2. Kerr, D.E., Propagation of Short Radio Waves (McGraw-Hill Book Company, N.Y., 1951).

3. Beckmann, P. and A. Spizzichino, The Scattering of Electromagnetic Waves from Rough Surfaces (Pergamon Press, N.Y., 1963)

4. Goodman, J.W., Introduction to Fourier Optics, (McGraw-Hill Book Company, N.Y., 1968).

5. Sommerfeld, A., Optics (Academic Press, N.Y., 1954).

6. Mitzner, K.M., "Change in Polarization on Reflection from a Tilted Plane," Radio Science, 1, no. 1 (Jan. 1966), pp. 27-29.

7. Silver, S., Microwave Antenna Theory and Design (McGraw-Hill Book Company, N.Y., 1949).

8. Keller, J.B., "Geometrical Theory of Diffraction," Journal of the Optical Society of America, 52, no. 2 (February 1962), pp. 116-130.

9. Crispin, J.W. and K.M. Siegel, Methods of Radar Cross-Section Analysis (Academic Press, N.Y., 1968).

10. Horonjeff, R., Planning and Design of Airports (McGraw-Hill Book Company, N.Y., 1962).

11. "Microwave Landing System," Phase I Report, ITT Gilfillan (27 September 1972).

12. Evans, J.E., Burchsted, R., Capon, J., Orr, R.S., Shnidman, D.A. and Sussman, S.M., "MLS Multipath Studies, Volume I: Mathematical Models and Validation," Project Report ATC-63, Lincoln Laboratory, M.I.T. (25 February 1976).

13. Shnidman, D.A., "The Logan MLS Multipath Experiment," Project Report ATC-55, Lincoln Laboratory, M.I.T. (23 October 1975).

14. Riblet, H.J. and C.B. Barker, "A General Divergence Formula," Journal of Applied Physics, 19 (January 1948), pp. 63-70.

15. Kodis, R.D., "A Note on the Theory of Scattering From an Irregular Surface," IEEE Trans. Ant. Prop., AP-14, no. 1 (January 1966), pp. 77-82.

References (Cont'd)

16. Barrick, D.E., "Rough Surface Scattering Based on the Specular Point Theory," IEEE Trans. Ant. Prop., AP-16, no. 4 (July 1968), pp. 449-454.

17. McGarty, T.P., "Models of Multipath Propagation Effects in a Ground-to-Air Surveillance Systems," Technical Note 1974-7, Lincoln Laboratory, M.I.T. (February 25, 1974). DDC AD-777241/1.

18. Wait, J.R. and A.M. Conda, "Diffraction of Electromagnetic Waves By Smooth Obstacles for Grazing Angles," Jour. Res. NBS, 63D, no. 2 (Sept.-Oct. 1959), pp. 181-197.

19. Benjamin, J. and G.E.J. Peake, "Contributions to the U.K. Microwave Landing System Study (Phase 1)," Royal Aircraft Establishment, Tech. Memo RAD 1021 (May 1973).

20. Neugebauer, H.E.J. and M.P. Bachynski, "Diffraction by Smooth Cylindrical Mountains," Proc. IRE, 46 (1958), pp. 1619-1627.

21. Jordan, E.C. and K.G. Balmain, Electromagnetic Waves and Radiating Systems (Prentice-Hall, Inc., N.J., 1968).

22. "Microwave Landing Systems," TACD Final Report, Texas Instruments (Thomson-CSF), FAA-RD-74-170 (September 1972).

23. Evans, J.E., "A Ray Theory/Far Field Antenna Pattern for Rectangle Shadowing," Project Report, Lincoln Laboratory, M.I.T. (in preparation).

24. Spiridon, A., "Impact of Obstacle Shadows in Monopulse Azimuth Estimate," Project Report ATC-50, Lincoln Laboratory, M.I.T. (17 July 1975), DDC AD-A015139/9.

25. "IBM System/360 and System/370 Fortran IV Language," IBM Corporation Publication GC28-6515-10 (May 1974).

26. Gradshteyn, I.S. and I.M. Ryzhik, Table of Integrals, Series and Products (Academic Press, N.Y., 1965).

27. Millington, G, R. Hewitt and F.S. Immirzi, "Double Knife-Edge Diffraction in Field-Strength Predictions," Monograph No. 507E, Proc. IEE (September 1962), pp. 419-429.

28. Millington, G., R. Hewitt and F.S. Immirzi, "The Fresnel Surface Integral, Monograph No. 507E, Proc. IEE (September 1962), pp. 430-437.